UNIVERSITY
OF ICELAND

Ph.D. Thesis

in Geology

Early Pleistocene environment and climate of the Nihewan Basin, NE China

Ahmed Hamdi Abdrabou Moghazi

March 2026

FACULTY OF EARTH SCIENCES

Early Pleistocene environment and climate of the Nihewan Basin, NE China

Ahmed Hamdi Abdrabou Moghazi

Dissertation submitted in partial fulfillment of a
Philosophiae Doctor degree in Geology

PhD Committee
Steffen Mischke, supervisor
Institute of Earth Sciences, University of Iceland
Ívar Örn Benediktsson
Institute of Earth Sciences, University of Iceland
Þorsteinn Þorsteinsson
Icelandic Meteorological Office

Opponents
Jonathan Holmes
University College London
Christopher J. Bae
University of Hawai'i at Manoa

Faculty of Earth Sciences
School of Engineering and Natural Sciences
University of Iceland
Reykjavík, March 2026

Early Pleistocene environment and climate of the Nihewan Basin, NE China
Dissertation submitted in partial fulfillment of a *Philosophiae Doctor* degree in Geology

Faculty of Earth Sciences
School of Engineering and Natural Sciences
University of Iceland
Askja, Sturlugata 7
IS-102, Reykjavík
Iceland

Telephone: 7619552

Bibliographic information:
Moghazi, H.A., 2026, *Early Pleistocene environment and climate of the Nihewan Basin, NE China,* PhD dissertation, Faculty of Earth Sciences, University of Iceland, 138 pp.

Author ORCID: https://orcid.org/0009-0003-4597-5901
ISBN number: ISBN 978-9935-9877-1-6

Abstract

The Nihewan Basin in northern China preserves abundant Early Pleistocene Palaeolithic sites and represents one of the earliest locations of hominins outside Africa. Sediments from three excavation trenches at the Dachangliang ridge in the northeastern part of the Nihewan Basin were investigated in the PhD study to reconstruct the environmental and climatic changes and assess their relationship with hominin activities during the Early Pleistocene. A multi-proxy approach was applied, integrating field-based observations with grain-size, magnetic susceptibility and ostracod assemblage (bivalved micro-crustacean) analyses, as well as parameterized grain-size end-member modeling, cyclostratigraphic analysis and stable isotope analysis of ostracod shells ($\delta^{18}O$ and $\delta^{13}C$ values). The studied sediments were mostly interpreted as fluvially reworked, originally aeolian deposits which accumulated through six depositional cycles, alternating between dominantly a wetland with periods of lake and alluvial plain settings. The grain-size distributions of the synthetic NH-T composite section were attributed to a mixture of four distinct end members (EMs 1-4). EMs 1-3 were used to infer the history of East Asian winter/summer monsoons (EAWM/EASM) in the region. Inferred EASM conditions dominated during periods from ca. 1.66-1.62 Ma, 1.52-1.25 Ma and after 0.82 Ma, whereas EAWM conditions prevailed from ca. 1.62-1.52 Ma and during the Mid-Pleistocene transition (MPT) 1.25-0.82 Ma. The unexpectedly high $\delta^{18}O$-$\delta^{13}C$ covariance suggests that the basin was mostly hydrologically closed, and waters affected by evaporation. Hydrological state shifts between more standing and flowing waters were detected. Assessed together with the synthetic archaeological record, hominins apparently occupied the basin during periods of prevailing EASM climate and more standing waters. Collectively, these insights refine our current perspectives of the favorable and less favorable climatic conditions that shaped the Early Pleistocene hominin activities in the region. Thus, this study establishes a foundation for continued research on the palaeoenvironments of Early Pleistocene hominins in East Asia.

Útdráttur

Nihewan-sigdældin í norðurhluta Kína varðveitir fjölda fornminja frá fyrri hluta pleistósen á fornsteinöld og er einn elsti fundarstaður frummanna utan Afríku. Í þessari doktorsrannsókn er gerð greining á setlögum úr þremur skurðum á Dachangliang hryggnum í norðausturhluta Nihewan-sigdældarinnar. Markmið rannsóknarinnar er að endurskapa umhverfis- og loftslagsbreytingar og meta tengsl þeirra við athafnir frummanna á fyrri hluta pleistósentímabilsins. Fjölþáttanálgun er beitt, þar sem vettvangsathuganir eru tengdar við greiningar á kornastærð, segulviðnámi og samsetningu tvískelja skelkrabba (ostracod). Að auki er notast við breytubundin kornastærðardreifingarlíkön (end-member modeling), greiningar á hringferlum jarðlagaskipanar (cyclostratigraphy) og greiningu á stöðugum samsætum í skeljum skelkrabba ($\delta^{18}O$ og $\delta^{13}C$ gildi). Setlögin sem rannsökuð voru eru að mestu túlkuð sem árset sem var upphaflega vindborið. Það safnaðist upp í sex setmyndunarhrinum, annars vegar í votlendi með tímabundnum stöðuvatnamyndunum, og hins vegar á ársléttum. Kornastærðardreifingu samsetta sniðsins NH-T má rekja til fjögurra ólíkra þátta (EM1-4). EM1-3 voru notaðir til að draga ályktanir um sögu monsúnrigninga um sumur og vetur (EASM/EAWM) í austurhluta Asíu. Skilyrði til sumarrigninga voru ríkjandi fyrir um 1,66-1,62, 1,52-1,25 og frá 0,82 milljónum ára. Aftur á móti voru skilyrði til vetrarrigninga ríkjandi frá u.þ.b. 1,62-1,52 milljónum ára og á tímabili mikilla umbreytinga á mið-pleistósen fyrir um 1,25-0,82 milljónum ára. Óvenju sterk samfylgni $\delta^{18}O$–$\delta^{13}C$ bendir til þess að vatnasvæðið hafi að mestu verið aflokað og orðið fyrir áhrifum uppgufunar. Greina mátti breytingar á vatnafari milli stöðuvatnsástands og rennandi vatns. Samhliða fornleifagögnum virðist sem frummenn hafi verið á vatnasvæðinu á tímabilum þar sem loftslag með sumarrigningum (EASM) og myndun stöðuvatna var ríkjandi. Samanlagt skerpa þessar niðurstöður skilning okkar á þeim hagstæðu og óhagstæðu loftslagsskilyrðum sem mótuðu athafnir frummanna á fyrri hluta pleistósentímabilsins á þessu svæði. Þannig leggja þessar rannsóknir mikilvægan grunn að frekari rannsóknum á fornloftslagi og umhverfisaðstæðum frummanna í Austur-Asíu á fyrri hluta pleistósen.

To my parents

Table of Contents

List of Figures

List of Tables

Acknowledgements

This PhD dissertation is the product of a nearly five-year journey of exciting and sometimes rather challenging days, during which I have been fortunate to learn so much. The generous support from the University of Iceland Doctoral Research Fund and the Doctoral Teaching Assistant Grant made this research possible. Although this work is attributed to me alone, it would not have been possible without the support and contributions of many people.

First and foremost, I would like to express my most sincere gratitude to my supervisor, Dr. Steffen Mischke, for offering me the opportunity to pursue this project and for the excellent guidance he has provided throughout. Thank you, Steffen, for your patience, constant encouragement, regular discussions and for making my PhD journey such a positive and meaningful experience.

My gratitude also extends to several key collaborators. I thank Dr. Hailong Zhao at Liaoning University, his students, and the local farmers for their crucial role during the fieldwork. I am also grateful to Dr. Chengjun Zhang at Lanzhou University for providing grain-size data, facilitating important contacts, and for helpful discussions.

My thanks also go to the other members of my PhD committee, particularly Dr. Ívar Örn Benediktsson for his support and time shared through the course of the project.

A big thank you to Al-Hussein and Ásta for helping me with my work.

Thank you to the wonderful fellow PhD students for the discussions, shared experiences, and friendship: Araksan, Patrick, Diana, Tingting, Nína, Mathis, Emily, Heini, Noemi, Daniel, Didas, Yilin, Patricia, Eemu, Nicolas, Méline, Bryndís, Yasmeen and many others.

Finally, and most importantly, I would like to express my heartfelt thanks to my parents and siblings for their love, encouragement, and unwavering support throughout this entire journey. I could not have reached this milestone without you, and I hope to have made you proud.

1 Introduction

1.1 Background on Nihewan Basin

The Early Pleistocene (2.58-0.78 Ma) was a critical period for hominin evolution, characterized by early human survival, adaptation and dispersal, likely driven by the changing climate conditions (Potts et al., 2020; Yang et al., 2021). However, most of our current understanding of Pleistocene human evolution, migrations, and their environmental and climatic context comes from research in Africa, which represents a bias in both research focus and interpretation. This highlights the need for exploration in other, under-researched regions, such as Asia. The Nihewan Basin is a key research area as it has the highest concentration of the Early Pleistocene Palaeolithic sites in E Asia (Fig. 1.1; Yuan et al., 2011). The basin has long been regarded as the third oldest known location of hominin occupation outside of Africa, following the 2.1 Ma site of Shangchen on the Chinese Loess Plateau (CLP) and the 1.8 Ma site of Dmanisi in Georgia (Lordkipanidze et al., 2013; Zhu et al., 2018). Recent paleoanthropological discoveries and revised chronologies, however, show that a growing number of sites across Asia appears to predate the middle Early Pleistocene sites in the Nihewan Basin (Bae and Manthey, 2025). For example, the Xihoudu site, dated to 2.43 Ma, currently represents the earliest evidence of hominin presence in China and possibly in the whole of Asia (Shen et al., 2020).

This late Cenozoic intermontane basin in the relatively high latitude part of northern China contains thick, well-constrained, continuous sedimentary sequences, which preserve rich assemblages of mammalian fossils and an abundance of stone artefacts (Fig. 2.1, Fig. 3.1, Fig. 4.1; Barbour, 1924; Teilhard de Chardin and Piveteau, 1930; Deng et al., 2008; Yang et al., 2019).

The fluvio-lacustrine sequences of the so-called “Nihewan Beds” (Barbour, 1924) or the Nihewan Formation (Min and Chi, 2003) represent the type section of the Early Pleistocene in N China (Young, 1950). Over the last 100 years, the most widely known Quaternary studies in the Nihewan Basin have focused on documenting and examining the technology of stone tools, describing megafaunal components, and using magnetostratigraphy to date lithic artefact-bearing sediment sections (Wei, 1983; Xia, 1992; Qiu, 2000; Deng and Zheng, 2005; Wang et al., 2005, 2006; Deng et al., 2006a, 2006b, 2007, 2008; Liu et al., 2010; Ao et al., 2012, 2013a).

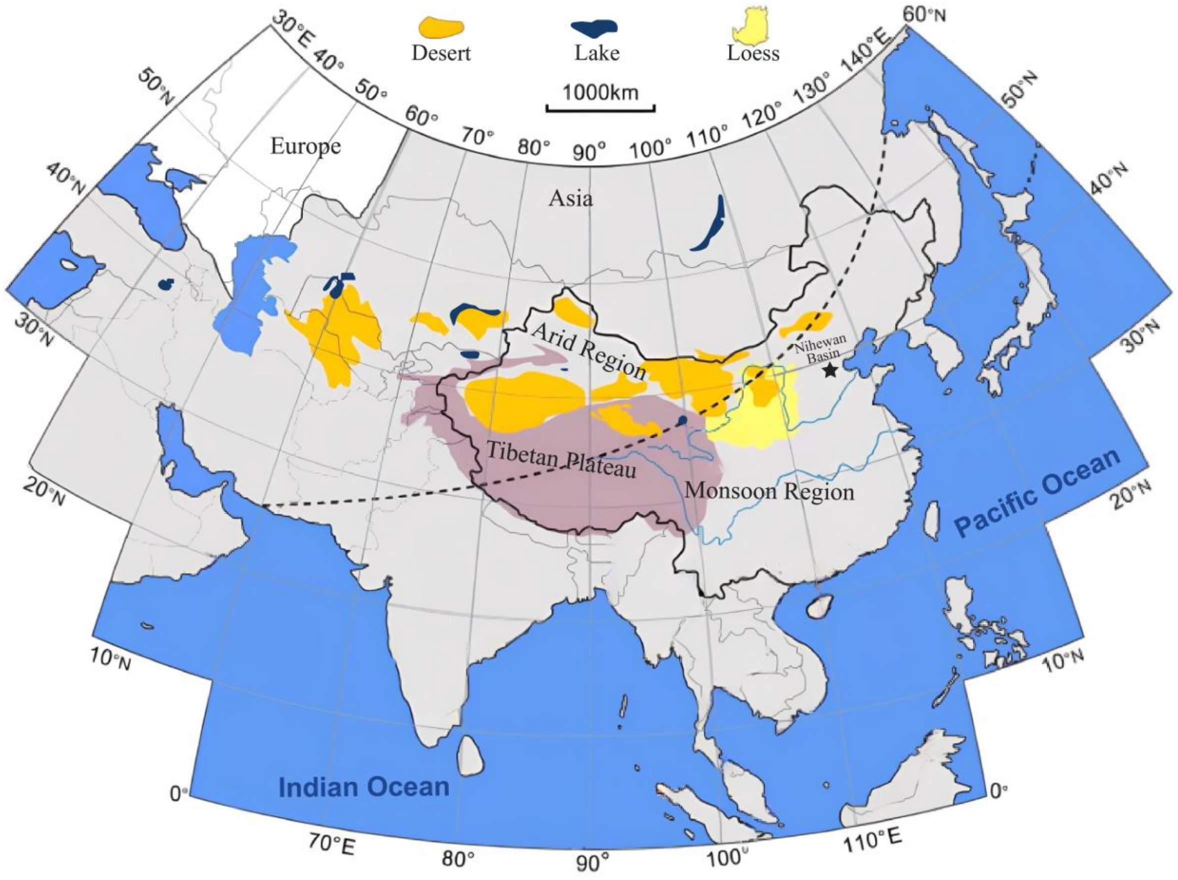

Figure 1.1 *Location of Nihewan Basin marked with a black star (modified after Zhang et al., 2011). The dashed line marks the northernmost limit of the East Asian summer monsoon*

The archaeological excavations in the basin have uncovered hominin-produced stone tools dating back from ca. 1.66-0.4 Ma (Dennell, 2013). The most important archaeological sites discovered in the basin include Majuangou (MJG; 1.66-1.32 Ma), Dachangliang (DCL; 1.36 Ma), Xiaochangliang (XCL; 1.36 Ma), Feiliang (FL; 1.2 Ma), Donggutuo (DGT; 1.1 Ma), Cenjiawan (CJW; 1.1 Ma), Huojiadi (HU; 1.0 Ma), and Maliang (ML; 0.8 Ma) (Fig. 2.1, Fig. 3.1; Xie and Cheng, 1990; Zhu et al., 2001, 2004; Wang et al., 2005; Deng et al., 2006a, 2006b, 2007; Liu et al., 2010). Throughout this timeframe of hominin activities, the basin was characterized by mixed conditions of forests and grasslands (Ao et al., 2013b).

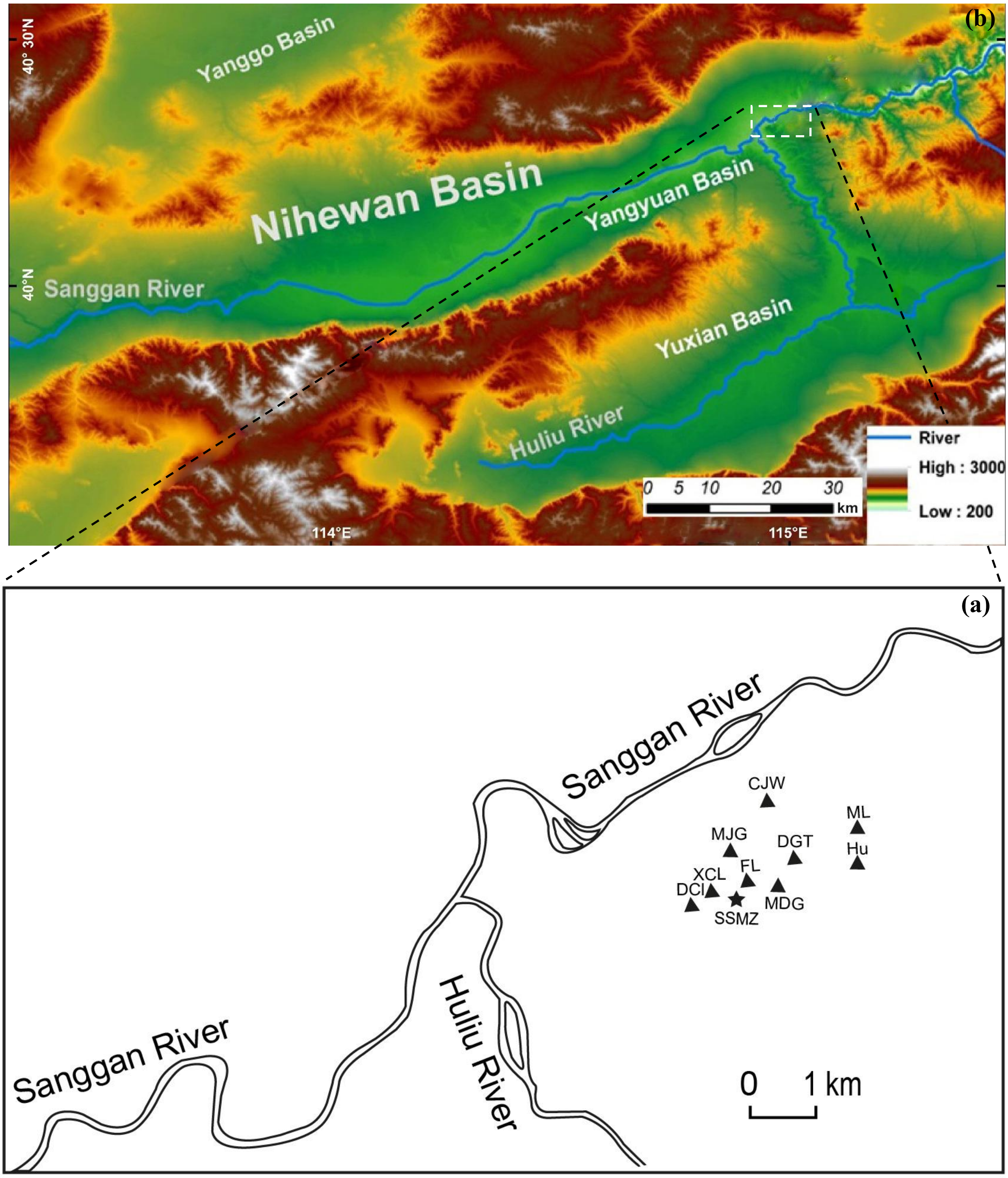

Figure 2.1 *Early Pleistocene fossil (star) and archaeological (triangles) sites (a) in the Nihewan Basin (b)*

The Nihewan fauna *sensu stricto* at Xiashagou represents the Early Pleistocene type fauna in N China and serves as a key reference for biostratigraphical correlations in the region (Deng et al., 2019; Tu et al., 2022). This mammalian assemblage is mostly composed of Palaeoarctic taxa,

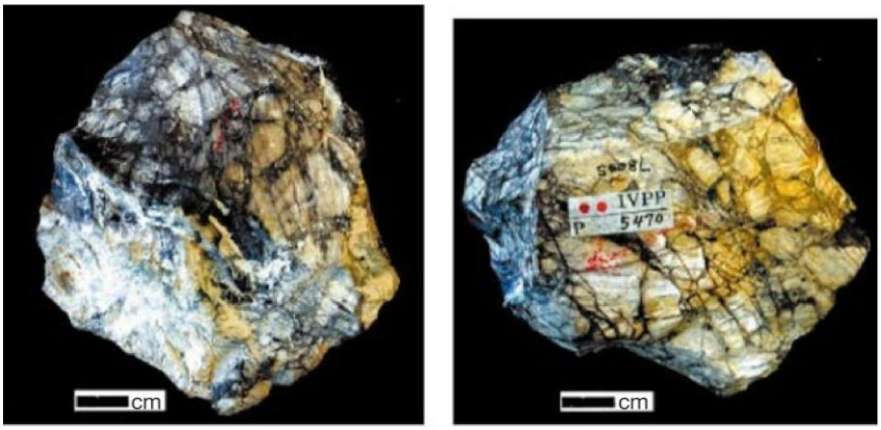

Disc core

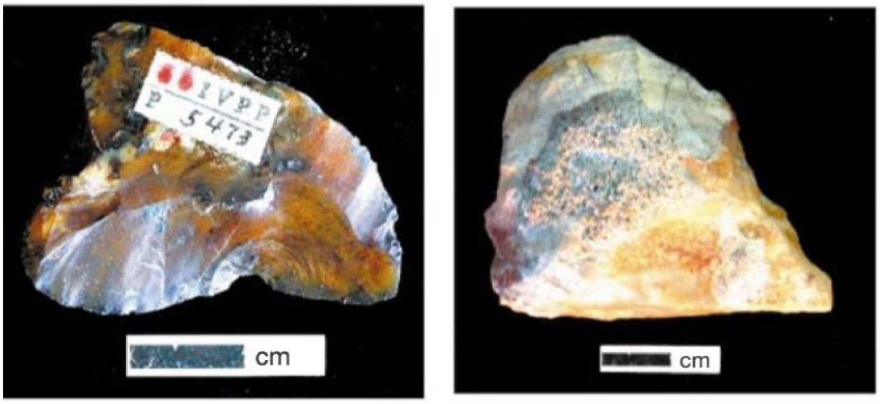

Notch

Side scraper

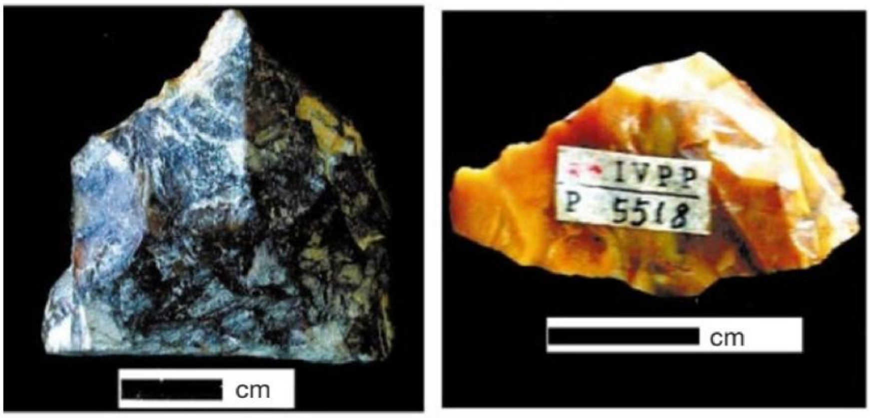

Borer

Burin

Figure 3.1 *Examples of stone artefacts from the Early Pleistocene Xiaochangliang site in the Nihewan Basin (modified after Zhu et al., 2001)* including early mammoth (*Mammuthus meridionalis* and *M. trogontherii*), woolly rhino (*Coelodonta nihowanensis*), early bison (*Bison palaeosinensis*), Chihli wolf (*Canis chihliensis*), raccoon dogs (*Nyctereutes* spp.) and diverse horses (*Equus* spp.) (Fig. 2.1, 4.1; Tong et al., 2021, 2024). In addition, other taxa found include bovid (*Gazella* sp.), camel (*Paracamelus gigas*), deer (*Cervus* sp.) and cat (*Felis* sp.) (Teilhard de Chardin and Piveteau, 1930; Tong et al., 2021).

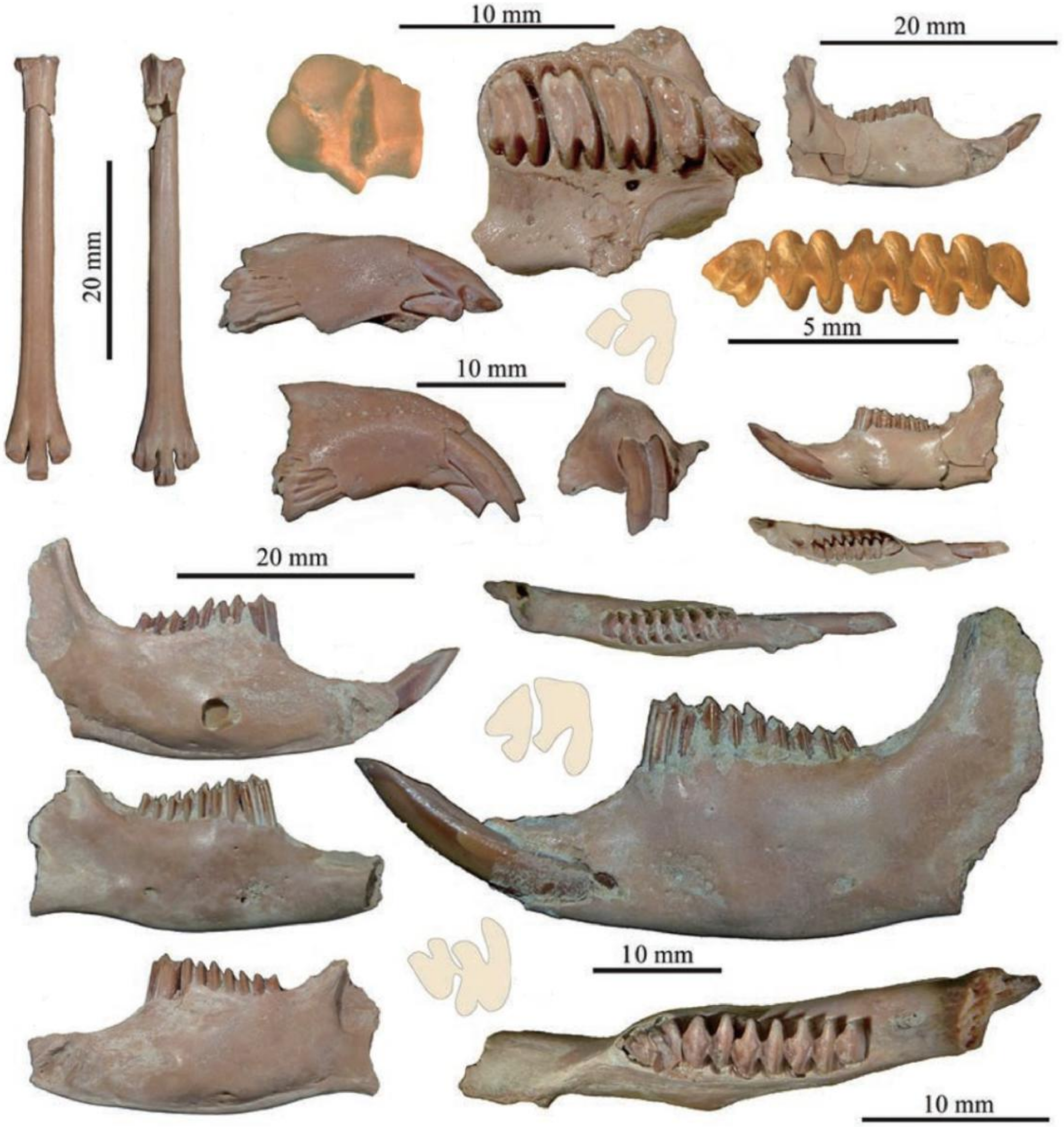

Figure 4.1 *Mammalian fossil remains recovered from the Early Pleistocene Shanshenmiaozui (SSMZ) site, Nihewan Basin (modified after Tong et al., 2021)*

1.2 Motivation

Despite the importance of the Nihewan Basin and the number of conducted studies over a century of research in the basin, the published literature presents conflicting interpretations of the complex depositional history in the Nihewan Basin, often under the misconception that the basin's sedimentary infill is composed of fluvio-lacustrine or mostly lacustrine sediments (Barbour, 1924; Li et al., 2000; Min et al., 2002, Hu et al., 2005; Li et al., 2008; Chen et al., 2015). A holistic investigation using sedimentological and micropalaeontological analyses of the long stratigraphic Early Pleistocene sediment sections in the basin is missing which results in the first motivating factor of this dissertation. Moreover, the basin is geographically located at the eastern margin of China's loess distribution and ca. 400 km SW of the Chifeng area in Inner Mongolia where Early Pleistocene loess deposits have been found in river valleys and hills (Zeng et al., 2011, 2019). The basin's location has the potential to provide a valuable long-term record of the past atmospheric dustiness in relation to the variations of the East Asian Monsoon (EAM), possibly comparable with the Pleistocene monsoon evolution that was previously inferred from the CLP. Thus, the second motivation is to investigate whether the Nihewan deposits evolved by aeolian or aqueous transport media or a combination of both. Furthermore, previous efforts have been made for reconstructing the terrestrial hydroclimate changes based on $\delta^{18}O_{enamel}$ and $\delta^{13}C_{enamel}$ records of Pleistocene mammalian tooth enamel (Xu et al., 2021, 2023). However, longer-term continuous stable isotope records directly retrieved from strata in the Nihewan Basin and covering the long span of ca. 1.3 millions of years of hominin activities in the basin between ca.1.66-0.4 Ma (Zhu et al., 2004; Deng et al., 2008; Dennell, 2013; Pei et al., 2019) are also still lacking. Addressing this gap derives the third motivation.

This dissertation contributes to answering the following research questions:

- What were the Early Pleistocene depositional settings of the accumulated sediments at Dachangliang in the northeastern Nihewan Basin?
- How do the Dachangliang sediments correlate lithologically and stratigraphically with adjacent well-dated artefact-bearing sediment sections?
- What characterizes the Dachangliang sediment sources, transportation dynamics, and their links with the EAM variability in the region during the Early Pleistocene?
- How did the hydrological state of the Nihewan Basin's water bodies evolve during the Early Pleistocene?
- What were the specific environmental and climatic conditions during periods of proven human presence in the basin?

1.3 Research methods and goals

The overarching goal of this dissertation is to provide a better understanding of the palaeoenvironmental and palaeoclimatic context of hominins in the Nihewan Basin. The dissertation is based on three exceptionally well-exposed, accessible, thick, and continuous sediment sections (T1-T3) located along the Dachangliang mountain ridge on the northeastern margin of the Nihewan Basin (Fig. 5.1). Detailed logging and sampling were carried out at centimeter-scale resolution, yielding a total of 414 sediment samples with a total sediment thickness of 112.5 m. The data used in this study were obtained through a multi-proxy approach that involved: 1) the assessment of detailed field-based sedimentological observations and analyses, 2) grain-size analysis with a Malvern 2000 laser particle sizer, 3) end-member modelling analysis of grain-size data according to Dietze et al. (2012) and Paterson and Heslop (2015), 4) measurements of magnetic susceptibility using a SM150L magnetic susceptibility meter, 5) identification of ostracod (micro-crustacean) species assemblages following Mischke et al. (2006) and Pang et al. (2015), 6) cyclostratigraphic analysis using WaverideR (Arts, 2023) and Astrochron (Meyers, 2014) R packages, with orbital tuning to the La2004 astronomical solution (Laskar et al., 2004), and 7) stable oxygen and carbon isotope analysis of ostracod shells.

Detailed descriptions of the background and interpretation of these proxies are provided, where relevant, in the following chapters.

Figure 5.1 *Visual inspection and sampling of lower part of T1 (a) and T3 (b) sediment sections by MSc students of Dr. Zhao, local assistants and the PhD project supervisor Dr. Steffen Mischke (c) and (d)*

1.4 Dissertation overview

The introduction presented here outlines the contribution of this dissertation to a better understanding of the Early Pleistocene palaeoclimate and palaeoenvironment of the Nihewan Basin, and briefly summarizes the analytical approaches used to address the key research questions. The following chapters represent three manuscripts I-III which are thematically organized and generally follow the evolution of my doctoral research at the Institute of Earth Sciences, University of Iceland. Two of these manuscripts have already been published, and the third is under revision. **Chapter 2**, *Early Pleistocene depositional and environmental conditions at Dachangliang, Nihewan Basin, NE China*, provides new insights into understanding the complex depositional history of the exposed Early Pleistocene sediments in the Nihewan Basin, NE China. These sediments were interpreted as fluvially reworked, originally aeolian deposits which accumulated through six remarkable depositional cycles of changing hydrodynamic conditions between dominantly a wetland with periods of lake and alluvial plain settings. This manuscript was published in *Frontiers in Earth Science*. **Chapter 3**, *The East Asian monsoon variability in the Nihewan Basin, northern China, during the Early Pleistocene: A grain size end-member modelling analysis*, presents the first application of end-member modelling analysis of the Nihewan sediments. Four grain-size end members (EMs) were identified and used to quantitatively reconstruct the history of the East Asian Summer Monsoon, dust-storm outbreaks during springtime, and the Eastern Asian Winter Monsson in the basin. The reconstructed climatic changes help highlight periods of the favorable and less favorable conditions for hominin occupation during 1.66-0.78 Ma. This manuscript was published in *Quaternary Science Reviews*. **Chapter 4**, *Concurrent hydrological closure and hominin presence in the Early Pleistocene Nihewan Basin (northern China): insights from stable isotopes*, presents the first long-term stable isotope record from the Early Pleistocene Nihewan Basin which indicates that the basin was mostly hydrologically closed, and waters affected by evaporation. The inferred hydrological state at the study location shifted between closed settings with higher water levels (more standing waters) and open settings with low water levels (more flowing waters). The stable isotope evidence, combined with the synthetic archaeological record, suggests that hominins probably occupied the Nihewan Basin during wetter climate when waters were more standing. This manuscript has been submitted to *Climate of the Past*.

References for the publications are listed below:

Moghazi, A.H., Zhao, H., Zhang, C., Omar, H., Eltijani, A. and Mischke, S. (2024). The East Asian monsoon variability in the Nihewan Basin, northern China, during the Early Pleistocene: a grain size end-member modelling analysis. *Quaternary Science Reviews*, 346.

Moghazi, A.H., Zhao, H., Zhang, C., Eyþórsdóttir E.A. and Mischke, S. (2024). Early Pleistocene depositional and environmental conditions at Dachangliang, Nihewan Basin, NE China. *Frontiers in Earth Science*, 12.

Moghazi, A.H., Zhao, H., Zhang, C., Schröder, B. and Mischke, S. (2025). Concurrent hydrological closure and hominin presence in the Early Pleistocene Nihewan Basin (northern China): insights from stable isotopes. Submitted to *Climate of the Past* (3rd December).

Manuscript I

2 Early Pleistocene depositional and environmental conditions at Dachangliang, Nihewan Basin, NE China

2.1 Abstract

The Pleistocene sediments of Nihewan Basin in NE China are intensively studied since ca. 100 years because of its rich mammalian fossil record and abundant stone-artefact-bearing layers. To better understand the mechanisms underlying past climate and environmental changes in the basin, three sediment sections at the Dachangliang location were investigated using a multi-proxy toolbox of sedimentological, magnetic susceptibility (MS) and micropalaeontological analyses. The exposed sediments are lithologically mostly relatively homogeneous, with grain sizes in a relatively small range. However, variations in colour, bedding structures, concentrations of magnetic minerals and the ostracod assemblage were used to correlate the three sections to form the synthetic NH-T section of 86.2-m total length. The sediments mainly represent varicoloured silt of probably reworked loess deposits, partially interbedded with fine sand layers and minor contributions of clay particles. These sediments are interpreted to have accumulated in wetlands alternating with deposition on an alluvial plain, and with a lacustrine setting which probably existed from time to time. These different depositional settings are expressed in the three dominant fine to coarse silt-sized components and the ostracod-assemblage changes (mostly *Limnocythere flexa*, *Ilyocypris* spp. and *Leucocythere* sp.). The recorded ostracods of laterally apparently consistent white marl beds (dominantly *Cytherissa lacustris*) were used to stratigraphically correlate these sections. The resulting NH-T section was further correlated with the three proximal artefact-bearing sections Majuangou, Banshan and Xiantai which have published magnetostratigraphic data. The correlation shows that the investigated sedimentary sequence was probably formed between ca. 1.7 and 0.9 Ma. The relatively continuous synthetic sequence NH-T represents three main wetter periods with three intervening drier intervals, possibly synchronous with interglacial (S_{23}-S_{20}, S_{15}-S_{13} and S_{10}-S_{9}) and glacial (L_{20}-L_{18}, L_{17}-L_{16} and L_{13}-L_{11}) periods which were previously inferred from the palaeoclimatic records of the Chinese Loess Plateau (CLP) in the SW of the Nihewan Basin.

2.2 Introduction

The study of the Early Pleistocene sediments in the Nihewan Basin, NE China, plays a key role in our understanding of the Quaternary natural and cultural history, and the interaction between early humans and the environment in N China. The Nihewan Basin is a late Cenozoic intermontane rift with a thick succession of lacustrine and fluvial sediments from the late Pliocene to the Late Pleistocene (Wei, 1991). The Nihewan Basin is significant in Quaternary geological research in China due to its continuous sedimentation and it is known for its fossil remains of the Pleistocene megafauna and rich source of lithic artefacts (Barbour, 1924; Teilhard de Chardin and Piveteau, 1930; Deng et al., 2008; Yang et al., 2019). As such, it has become an important location for investigating Quaternary palaeontology, palaeoenvironment, and palaeolithic archaeology at high latitudes in E Asia. Furthermore, the Nihewan Basin provides valuable insights into the evolution and behavior of early humans in the region following the earliest "Out of Africa" migration (Schick et al., 1991; Zhu et al., 2001; Zhu et al., 2004; Dennell, 2013). However, Bae and Manthey (2025) challenge the classic Out of Africa I model and show that a number of Asian sites predate the traditional 1.8 Ma threshold of the *Homo erectus* appearance and their artefactual record in the Nihewan Basin. The identification of pre-1.8 Ma sites across Asia supports the growing evidence of earlier, multi-lineage dispersals from Africa (Bae and Manthey, 2025). The most widely known Quaternary studies in the Nihewan Basin have focused on documenting and examining the technology of stone tools, describing megafaunal components, and using magnetostratigraphy to date lithic artefact-bearing sediment sections (Wei, 1983; Xia, 1992; Qiu, 2000; Deng and Zheng, 2005; Wang et al., 2005; Deng et al., 2006b; Wang et al., 2006; Deng et al., 2007; Deng et al., 2008; Liu et al., 2010; Ao et al., 2012, 2013a). The earlier inferences of Xia (1992) on the ancient lake shoreline changes in the Nihewan Basin indicated two periods of advance and three periods of retreat, forming terraces during the early and middle Pleistocene. In contrast, Li et al. (2008) suggested two longer lasting lacustrine periods with the accumulation of fluvio-lacustrine deposits in between based on their work on the exposed fluvio-lacustrine sequence at Xiaodukou (XDK, 120-m thick, ca. 1.8-0.1 Ma, correlated to marine isotope stages 64 to 11) in the Nihewan Basin. Some more recent studies provided a very schematic or cursory perspective of the basin evolution. For example, Chen et al. (2015) suggested that the Nihewan Basin underwent three major stages of evolution including expansion, contraction, and extinction, as indicated by the lacustrine, deltaic, and alluvial fan deposits which formed at 2.6, 1.8, and 0.11 Ma, respectively. Furthermore, the inferred paleo-lake history of the Taiyuan and Linfen grabens in N China, includes three periods of regressions in lake level followed by the deposition of loess during the Pleistocene (Hu et al., 2005). Despite over a century of research in the basin, the published literature presents conflicting interpretations of the complex depositional history in the Nihewan Basin. In addition, detailed sedimentological and micropalaeontological analysis of long stratigraphic Early Pleistocene sediment sections in the basin are missing. Thus, our work had the aim to provide a better understanding of 1) the Early Pleistocene depositional setting at Dachangliang in the Nihewan Basin, and 2) to establish a lithological and stratigraphic correlation between the Dachangliang deposits and the neighbouring well-dated palaeolithic sites in the E margin of the Nihewan Basin. We conducted a multi-proxy study, including the analyses of grain size, sediment colour, sedimentary structures, magnetic mineral concentrations, and ostracod assemblage of the deposits. The presented data are fundamental for a better understanding of the climate and environment during the Early Pleistocene, and their significance for the early periods of hominin occupation in the region.

2.3 Study area

The Early Pleistocene deposits of Dachangliang are exposed at the E margin of the Nihewan Basin in Yangyuan County, Hebei Province. The basin is located at the NE margin of the Loess Plateau, in the transitional zone between the Inner Mongolia Plateau and the N China Plain (Fig. 6.2). The basin is located in the NE part of the Shanxi Graben System, which developed in the region of Taihang Mountains and Yanshan Mountains during the Middle and Late Pliocene as a series of intermontane basins (Li et al., 1998). The Nihewan Basin is a NE-SW elongate graben structure with a floor at ca. 800-900 m above sea level, encompassing an area of about 80-km length and 15-20-km width. It is bounded by the Xiong'er Mountain to the N, the Liuleng Mountains to the S, the Fenghuang Mountains to the E and the Guancen Mountain to the SW. The basin is structurally separated by the Youfang dip-slip fault into two sub-basins: the Yangyuan sub-basin lies in the N and the Yuxian sub-basin in the S. The Nihewan deposits cover Archaean gneiss and Sinian quartzites (Xiong'er Mt.), Palaeozoic marine strata (Liuleng Mts.) and Mesozoic volcaniclastic rocks. Paleogene basalts and gravels occur occasionally within the basin in the SE of the Liuleng Mountains. Nihewan Basin accumulated a relatively continuous archive of fluvio-lacustrine sediments in a semi-deep to shallow palaeolake during the Late Pliocene to Middle Pleistocene. With tectonic development of a graben basin, reworked reddish sediments of aeolian origin were initially accumulated within the basin during the Early Pliocene. Subsequently, the basin became completely invaded by Nihewan palaeolake in the Middle-Late Pliocene (Ao et al., 2013b; Liu et al., 2018). During the Early to Middle Pleistocene, the water body began to disappear gradually and finally dried up (Xia, 1992). Afterwards, the lacustrine environment was replaced by a fluvial setting with the ancient tributaries of the Sanggan River flowing from SW to the NE through the basin (Wei, 2016). This depositional history resulted in the succession of the so-called "Nihewan Beds" (Barbour, 1924) or the Nihewan Formation (Min and Chi, 2003) that represents the type section of the Early Pleistocene in N China (Young, 1950). Today, the fluvio-lacustrine sequences are capped by wind-blown deposits from the last glaciation. Chi and Wei (2013) divided the sedimentary succession of the Nihewan Basin (approximately 700 m) into five lithostratigraphic units ranging in age from Pliocene to Holocene as follows: 1) the Pliocene Yuxian Formation, 2) the early Pleistocene Nihewan Formation, 3) the middle Pleistocene Xiaodukou Formation, 4) the late Pleistocene Xujiayao Formation, and 5) the Holocene Shibaozhuang Formation. Shao et al. (2026) subsequently refined the chronology of the Xujiayao sedimentary sequence, assigning it to the Late Middle Pleistocene. Confusingly, the entire sedimentary fill of the basin was also termed the Nihewan Beds (Barbour, 1924) and renamed the Nihewan Formation in recent years (Deng et al., 2008).

2.3.1 Dachangliang age

Magnetostratigraphic analysis of fluvio-lacustrine sediments at Dachangliang implied that sediments accumulated from the lower Olduvai subchron to the late Brunhes chron (Deng et al., 2006b). The age of the artefact-bearing layer at Dachangliang site, discovered in August 2000, and excavated in September 2000 and also in July and August 2001, is about 1.36 Ma based on the correlation of magnetostratigraphic, lithostratigraphic and magnetic susceptibility data with the neighbouring well-known Xiaochangliang site (Pei, 2002; Deng et al., 2006b). The latest astronomical dating shows that the estimated age of the artefact layer at the Dachangliang site is 1.48 Ma (Ao et al., 2010), slightly older than the Xiaochangliang site. The Majuangou-III site, only ca. 1 km to the NE of Dachangliang, is one of the oldest well-dated sites in NE China, dating back to approximately 1.66 Ma. In contrast, the earliest evidence for the presence of hominins in Asia comes from the Xihoudu site in the southern part of the Chinese Loess Plateau. The Xihoudu deposits were radiometrically dated to 2.43 Ma (Shen et al., 2020).

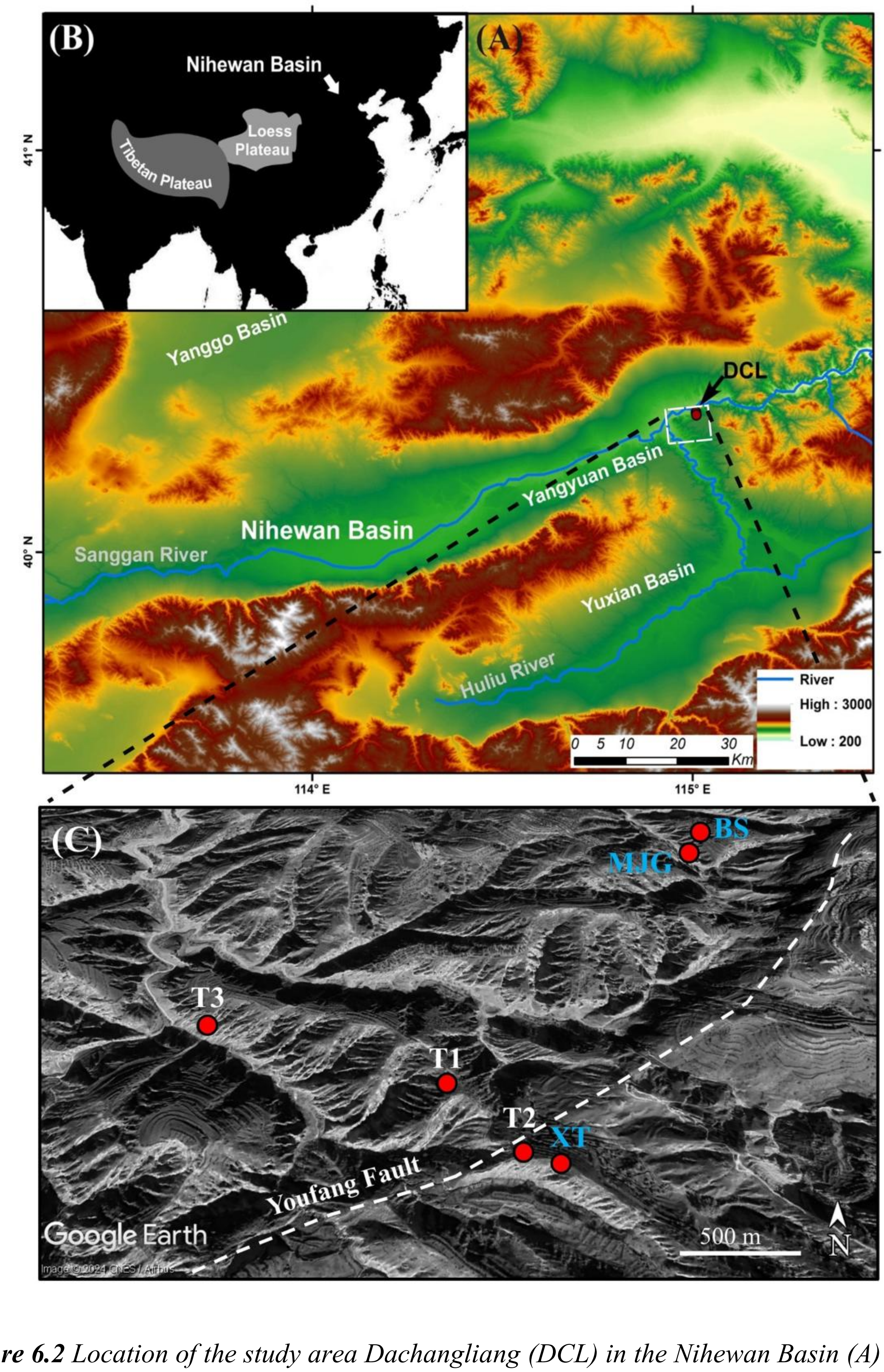

Figure 6.2 *Location of the study area Dachangliang (DCL) in the Nihewan Basin (A) and general position in Asia (B). Locations of the T1, T2 and T3 sections (white labels) and the neighbouring Paleolithic sites (Majuangou (MJG), Banshan (BS) and Xiantai (XT); blue labels (C)*

2.3.2 Hydrology

The Nihewan Basin is fed by a number of small rivers and streams, and it is drained by the Sanggan River, its tributary, the Huliu River. The Sanggan River originates from the SW mountains (mainly Guancen Mountain) and meanders through the Datong and Yangyuan sub-basins in a NE direction. Today, the Sanggan River flows out of the basin through the Sanggan Gorge at the province of Shanxi. The Huliu River, the main tributary, drains the S Yuxian sub-basin and joins the Sanggan River in the NE part of the Nihewan Basin.

2.3.3 Climate

The climate in the basin is semi-arid, controlled by the winter and summer monsoon with distinct seasonal changes. Winters are cold, dry, and influenced by prevailing NW winds (winter monsoon) which originate from the cold Mongolian High. Conversely, the region is characterized by high temperatures and abundant precipitation in the summer owing to the effect of SE winds (summer monsoon) driven by low pressure over the continent and high pressure over the N Pacific (Domrös and Peng, 1988). The mean annual temperature is 7.7°C with a mean January temperature of ca. -16°C, and mean July temperature of ca. 29°C (Yangyuan County Weather Station, 1980-2019; data source: China Meteorological Data Network, http://data.cma.cn). Mean annual precipitation is 347.8 mm (1980-2019), with the majority occurring during the summer months.

2.3.4 Vegetation, current human impact

The regional vegetation includes temperate steppe in the interior of the basin and temperate deciduous shrubland in the mountainous regions (Mu et al., 2015). Typical grassland taxa such as *Artemisia*, Gramineae and Asteraceae dominate below 1200 m asl. However, most of the flat alluvial areas adjacent to the rivers and streams are used for cultivation, and the main crops are *Zea mays* (corn), *Sorghum bicolor* (great millet) and *Setaria italica* (foxtail millet; Liu et al., 1996). Between 1200 and 1600 m asl, mixed forests of coniferous and broadleaved trees such as *Betula phatyphylla*, *Quercus*, *Carpinus* and *Pinus tabulaeformis*, and deciduous shrubs (*Ostryopsis* and *Spiraea salicifolia*) occur. Above 1600 m asl, cold-resistant coniferous forests mainly include *Larix principis-rupprechtii*, *Picea wilsonii* and *Pinus*.

2.4 Materials and Methods

2.4.1 Field work

Three sediment sections were newly exposed on the SW slope of the Dachangliang ridge at 40.2199 °N and 114.6589°E (T1), 40.2190°N and 114.6598°E (T2) and 40.2212 °N and 114.6549 °E (T3), respectively (Fig. 6.2). The tops of the T1, T2 and T3 sections were determined to be 894.04, 906.31 and 861.76 m, respectively, using a hand-held Qianxun SI (SR6) GPS receiver, a laser rangefinder and a tape. The lithology of the exposed sediments was described in detail including grain size, sedimentary bedding structures, pedogenic features (carbonate nodules, root casts, mottling, animal burrows, etc.), macroscopic fossils (mostly gastropod shells) and colour using the Munsell Soil Color Charts (2009) during the summers of 2018 and 2019. A total of 414 sediment samples were collected at intervals of

27 cm on average from the trenches (Fig. 7.2). The three sections represent a total sediment thickness of 112.5 m (45.8 m at T1, 26 m at T2, and 50.5 m at T3). In addition, three sediment samples were collected from two prominent, laterally consistent white beds (termed “white marls” by Barbour et al. (1926)) along the Dachangliang ridge between 100 and 330 m further SE of the southernmost section T2 (Fig. 6.2).

2.4.2 Age constrains of the investigated sediments

To roughly estimate the period of sediment formation represented by the newly investigated sections, we correlated our sections from Dachangliang with the adjacent Palaeolithic artefact-bearing sections Majuangou (MJG), Banshan (BS), and Xiantai (XT) recognized for their established magnetostratigraphic data (Zhu et al., 2004; Ao et al., 2010). These artefact-bearing sections with established magnetostratigraphy are located relatively closely to the newly investigated sections, in a distance of 100 m (XT) to 800 m (MJG and BS; Fig. 6.2). To determine the age of the sediments at different depths within the studied sections, we compared them to the sediments of nearby sections based on field observations including their sediment colour and grain size, and magnetic susceptibility data. The close proximity of the sedimentary section T2 to the XT section permitted a relatively straightforward stratigraphic correlation, also considering uncertainties due to lateral variations in sedimentary facies. The artefact-bearing bed at XT probably correlates with the sediments in the upper part of section T2 (Fig. 17.2). At MJG, a package of three distinctly coloured sediment layers, characterized as red, gray and yellow (RGY), was noticed. This RGY sediment package was used to laterally trace the four artefact-bearing beds from MJG and one artefact-bearing bed from BS to their correlative intervals at section T3 (Yang et al., 2022; Fig. 17.2). As a result of this correlation, a sediment accumulation rate of ca. 46 ka/m was roughly calculated. Thus, our investigated composite sedimentary section was probably formed within an age constrain

Figure 7.2 *Exposed sediment sections T1 to T3, including white marker layers W1, W2 and W3. The thicknesses of T1 and T2 are indicated and the dividing Youfang Fault (broken blue line) which caused a vertical displacement of approximately 30 m. The Sanggan River is flowing in the valley located N of the sampling locations (in the background)*

between ca. 1.7 and 0.9 Ma, covering the time from the end of the Olduvai and including the Jaramillo polarity subchrons (Fig. 17.2).

2.4.3 Laboratory analysis

2.4.3.1 Grain-size analysis

The grain-size distribution of all collected sediment samples was determined using a Malvern 2000 laser particle size analyzer at the Key Laboratory of Western China's Environmental Systems at Lanzhou University. In preparation for grain-size analysis, samples were chemically digested by sequential addition of HCl and H_2O_2 until carbonates and organic matter were eliminated. Then, the samples were treated with Na-hexametaphosphate to disperse aggregates. At least three measurement runs were performed for each sample, and the average was taken as the final result. The exported grain-size data were processed for sediment classification using the GRADISTAT software package (Blott and Pye, 2001), and the main textural parameters (mean and median grain size, sorting (σ_G), skewness (SK_G) and kurtosis (K_G) were calculated according to the equations of Folk and Ward (1957). The statistical coding program R language version 4.1.3 was used to identify the main types of grain-size-frequency curves of all samples, and to graphically present the calculated grain-size parameters, and the percentage abundances of the clay, silt and sand fractions *versus* section height (http://www.rstudio.com/). The sedimentological zones of the investigated sections were determined using the change point detection option in the software PAST. This method was selected as it offers a robust and objective way of recognizing changes in sedimentological characteristics and facilitates a precise stratigraphic correlation between the sections.

2.4.3.2 Magnetic susceptibility

The Magnetic susceptibility was measured using SM150L magnetic susceptibility meter (Institute of Earth Sciences, University of Iceland). The samples were first air-dried at room temperature in the laboratory for some days to avoid any chemical reactions. A sub-sample of ca. 10 g was placed in a non-magnetic polystyrene plastic container and measured within an AC magnetic field amplitude of 80 A m^{-1} at a low (χ_{LF}, 500 Hz) and high (χ_{HF}, 4000 Hz) frequency to calculate the frequency-dependent magnetic susceptibility (χ_{FD}) expressed as percentage χ_{FD} (%) = $[(\chi_{LF}-\chi_{HF})/ \chi_{LF}] \times 100$. A total of six repeat measurements per sample were performed to obtain accurate data and identify outliers.

2.4.3.3 Micropalaeontological analysis

A set of 47 sediment samples, three from individual sample locations in the SE of section T2, 21 from section T1 and 23 from section T3, were selected from two prominent sedimentary beds of white marls and from the under- and overlaying beds at intervals of 2.5 m for micropalaeontological analysis. Sub-samples of 30 g were treated using 3% hydrogen peroxide for about 24 h to remove organic matter and disaggregate the material. Then, the sediment was washed through standard sieves of 100, 250 and 1000 µm meshes and sieve residues were dried afterwards at 50°C for 24 hours. Ostracods were handpicked with needles and brushes from the sieve residues and examined under an OLYMPUS SZ61 low-power binocular microscope. Selected valves of each species were gold-coated and photographed with a Hitachi TM3000 scanning electron microscope. The ostracod valves were identified based on their outline and surface ornamentation according to Mischke et al. (2006) and Pang et al. (2015).

2.5 Results

2.5.1 Field observations

The exposed sediments at the sediment sections T1, T2 and T3 are lithologically mostly relatively homogeneous. They partly contain laminations of various thickness, horizontal and ripple bedding, and bioturbation features. The sediments are predominantly composed of varicoloured silt-sized materials, which are partly carbonate-rich, and partly interbedded with fine-grained sand layers and minor contributions of clay-sized particles. Carbonate-rich layers, which are up to a centimetre in thickness are occasionally present in the silt deposits. Lithological changes in the stratigraphic sequences occur as transitional, sharp, or erosional boundaries. The sediments display a range in colour on a centimetre scale from mostly very pale brown (10YR 7/3-4), yellowish brown (10YR 5/4-8), light olive gray (5Y 6/2), brownish yellow (10YR 6/8) to more minorly pale yellow (2.5Y 7/3-4), pink 2.5YR 8/3-4), light grey (2.5Y 7/1-2), white (2.5Y 8/1), greyish brown (2.5Y 5/2), reddish brown (2.5YR 4/3-4) and light brown (7.5YR 6/3-4; Figs. 8.2-10.2).

2.5.2 Laboratory results

The grain-size analysis of T1, T2 and T3 sediments reveals that coarse-grained silt (16-63 µm) represents the largest sediment fraction, ranging from a minimum of 4.6% to a maximum of 64%, with an average of 40%. The >63 µm size fraction also represents a significant portion of the sediments, ranging from a minimum of 0.6% to a maximum of 92%, with an average of 23%. The percentage of fine-grained silt (2-16 µm) varies from a minimum of 4% to a maximum of 72%, with an average of 33%. The clay-size fraction (<2 µm) represents the smallest portion; its range is from 0.2 to 15% with an average of 5% (Figs. 8.2-10.2). The grain-size-frequency distribution for most of the samples (72%) is unimodal, while the remaining samples (28%) show either bimodal or weakly polymodal distributions.

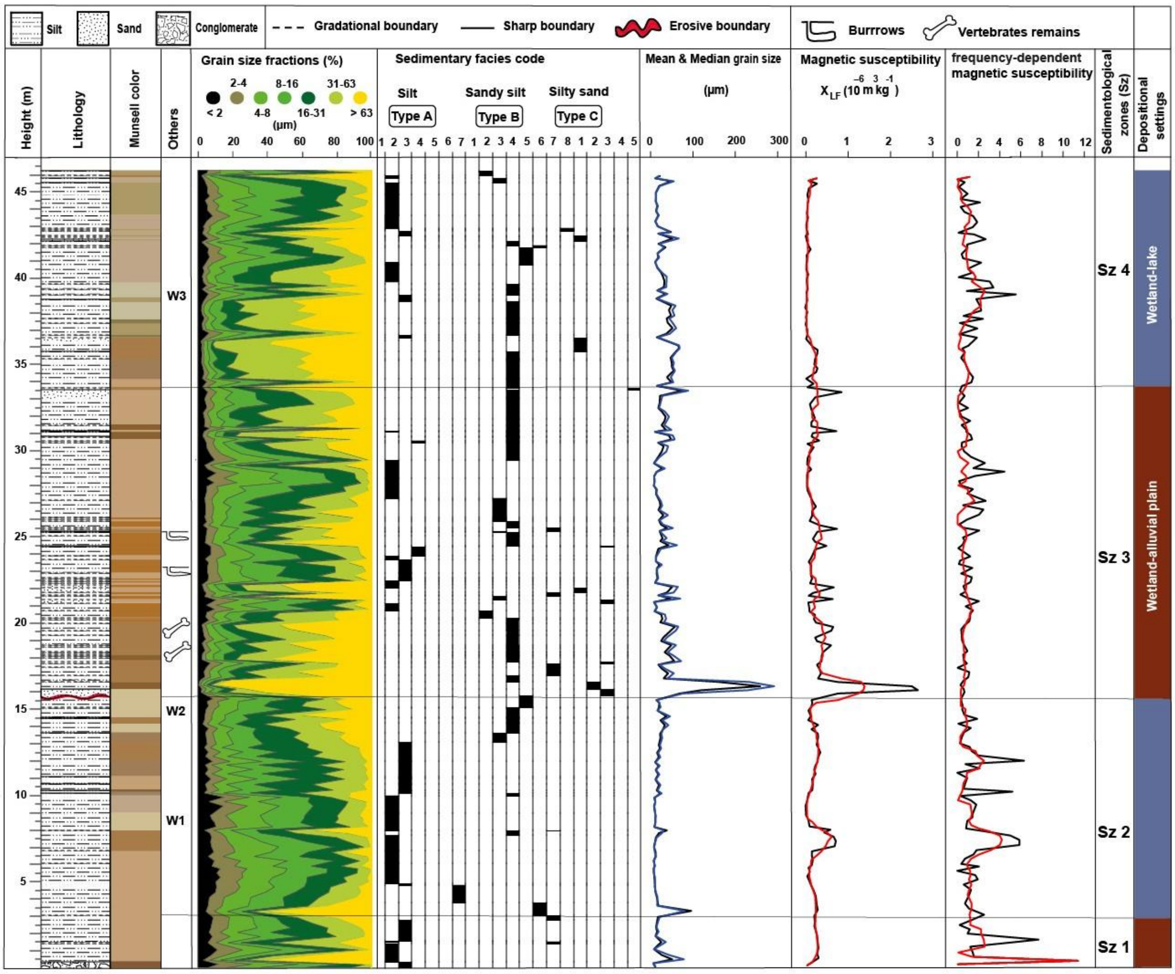

Figure 8.2 *Stratigraphy of the sediment section T1 including lithology, colour, position of white marker layers, grain-size fractions, sedimentary facies codes (represented by grain-size-frequency-curve types), mean (black) and median (blue) grain size, and magnetic and frequency-dependent magnetic susceptibilities (5-point running means in red). Resulting sedimentological zones at right*

The sediments range in mean (and median) grain size from a minimum of 6.3 µm (6.4 µm) to a maximum of 258.9 µm (292.1 µm) with an average of 27.8 µm (32.9 µm) in the T1 sediments, from 16.0 µm (17.0 µm) to 330.6 µm (343.8 µm) with an average of 41.3 µm (47.6 µm) in the T2 sediments, and from 6.7 µm (7.1 µm) to 125.9 µm (149.1 µm) with an average of 20.2 µm (24.1 µm) in the T3 sediments.

The sorting (σ_G) values are slightly variable from 2 to 10.8 µm (avg. of 3.1 µm) in T1, from 2.1 to 5.5 µm (avg 3.4 µm) in T2, and from 2.4 to 6.7 µm (avg 3.4 µm) in T3 samples, while the skewness (Sk_G) values are between -0.6 and 0.2 µm (avg -0.2) in T1, -0.3 to -0.1 (avg -0.2) in T2, and -0.4 to -0.02 (avg -0.2) in T3 samples. Additionally, the investigated samples exhibit kurtosis (K_G) varying from 0.8 to 2.2 µm with an average value of 1.2 µm, whilst T2 and T3

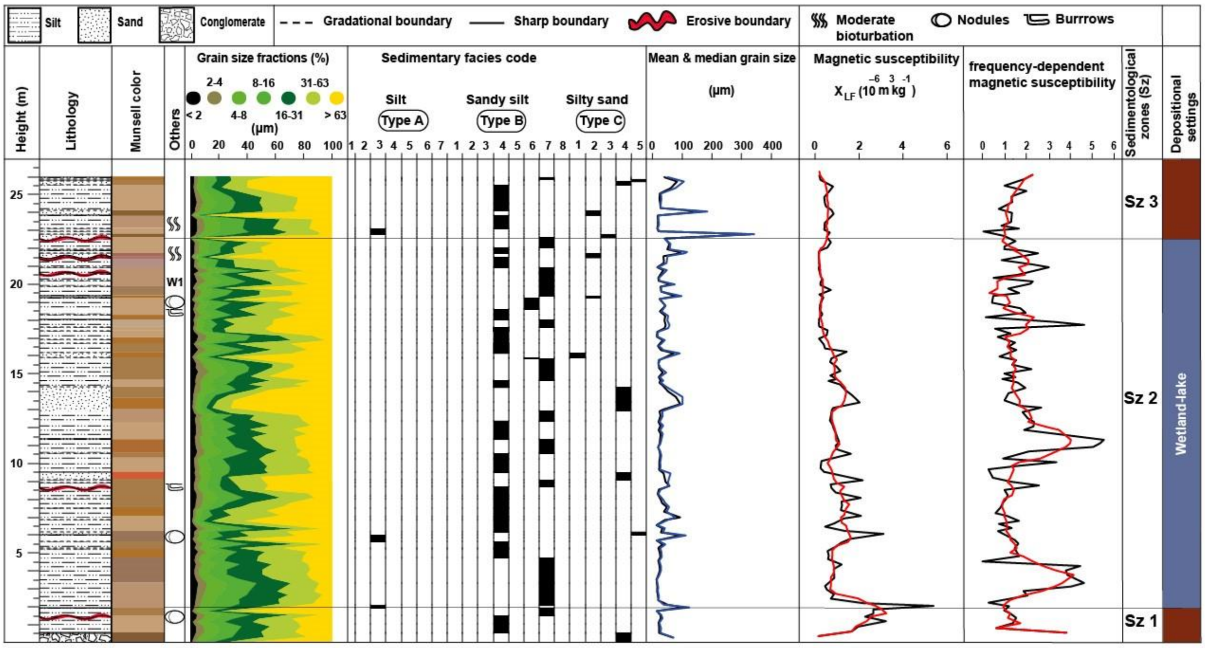

Figure 9.2 *Stratigraphy of the sediment section T2 including lithology, colour, position of white marker layers, grain-size fractions, sedimentary facies codes (represented by grain-size-frequency- curve types), mean (black) and median (blue) grain size, and magnetic and frequency-dependent magnetic susceptibilities (5-point running means in red). Resulting sedimentological zones at right*

samples have a range between 0.8 and 1.9 µm (avg 1.1 µm), to 0.7-1.9 µm (avg 1 µm), respectively (Figs. 11.2-13.2).

Magnetic susceptibility (χ_{lf}) in the sediment sections varies widely, with a range of 0.1-2.7 x 10^{-6} m^3 kg^{-1} in T1, 0.1-5.3 x 10^{-6} m^3 kg^{-1} in T2, and 0.1-4.4 x 10^{-6} m^3 kg^{-1} in T3. The average χ_{lf} values of the T1, T2 and T3 sections are 0.3 x 10^{-6} m^3 kg^{-1}, 0.8 x 10^{-6} m^3 kg^{-1}, and 0.7 x 10^{-6} m^3 kg^{-1}, respectively (Figs. 8.2-10.2). The related χ_{FD} values vary between 0.0-11.4%, with an average of 1.3%; between 0.0-5.5%, averaging 1.7%; and between 0.0-44.7%, with an average of 3.4%, respectively.

A freshwater-ostracod assemblage with low diversity is recorded in the three sediment sections with a total of 13 taxa identified. The most abundant species are *Limnocythere flexa*, *Ilyocypris* spp., *Leucocythere* sp. and *Heterocypris salina* (Fig. 14.2).

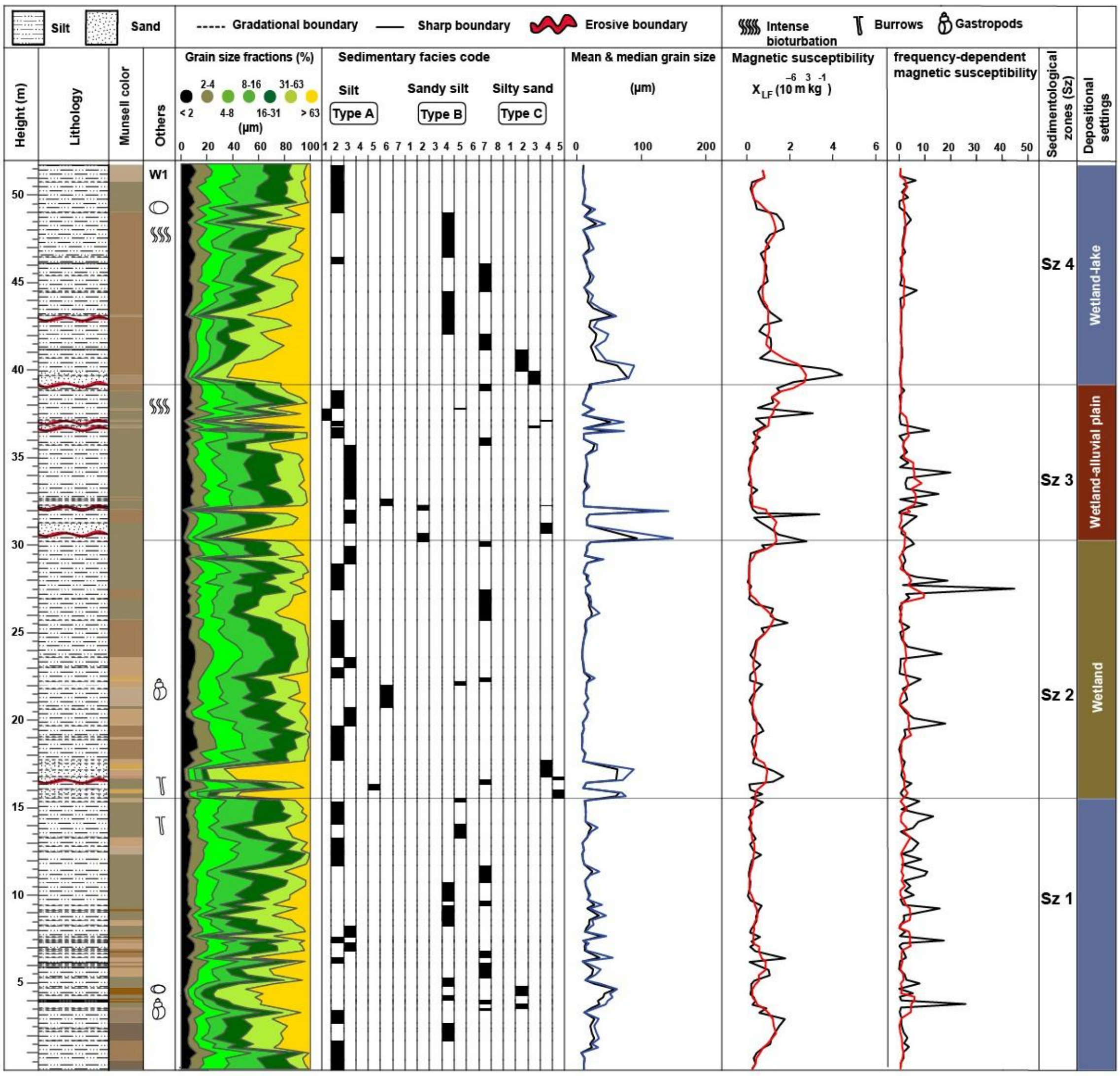

Figure 10.2 *Stratigraphy of the sediment section T3 including lithology, colour, position of white marker layers, grain-size fractions, sedimentary facies codes (represented by grain-size-frequency- curve types), mean (black) and median (blue) grain size, and magnetic and frequency-dependent magnetic susceptibilities (5-point running means in red). Resulting sedimentological zones at right*

In contrast to slightly darker and coarser-grained sediments, the white marl layers contain abundant valves of valves of *Leucocythere dorsotuberosa Cytherissa lacustris* apart from the white marl of the section T2. white marls contain less in comparison to the slightly darker and coarser-grained sediments (Fig. 14.2).

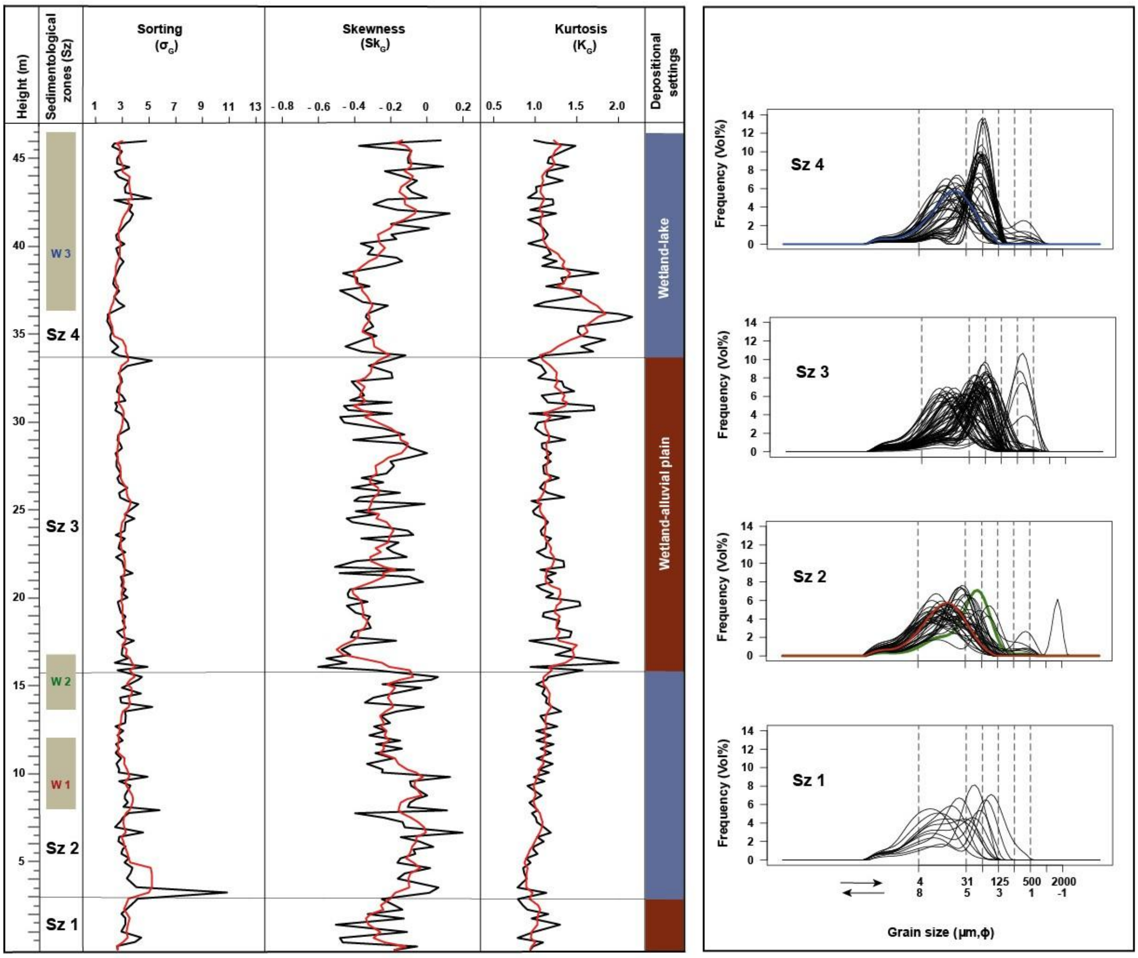

Figure 11.2 *Grain-size parameters (in micrometers) for sediments of T1 (left), presented as raw data (black) and as 5-point running means (red). Grain-size-frequency curves for the four sedimentological zones at right. The red, yellow, and blue curves represent the curves for sediments from the white marker layers W1, W2 and W3, respectively*

2.6 Discussion

2.5.1 Stratigraphic correlation of Dachangliang sediments

Generally, there are no consistent patterns of vertical variations in colour, grain-size distribution or the grain-size parameters sorting, skewness or kurtosis, and MS and χ_{FD} values observed across the three sediment sections (T1-T3). However, a clear differentiation based on sediment type, bedding structures and ostracod assemblage is noticeable (Supplementary Tables S1-S3; Figs. 8.2-13.2)

Section T1

In the T1 section, four sedimentological zones were identified (Fig. 8.2, Fig. 11.2):

Sedimentological zone (Sz) 1 **(0.0-3.0 m)** shows a range of mean grain sizes from fine to very coarse silt, (mostly fine silt from 10.7-15.6 µm).

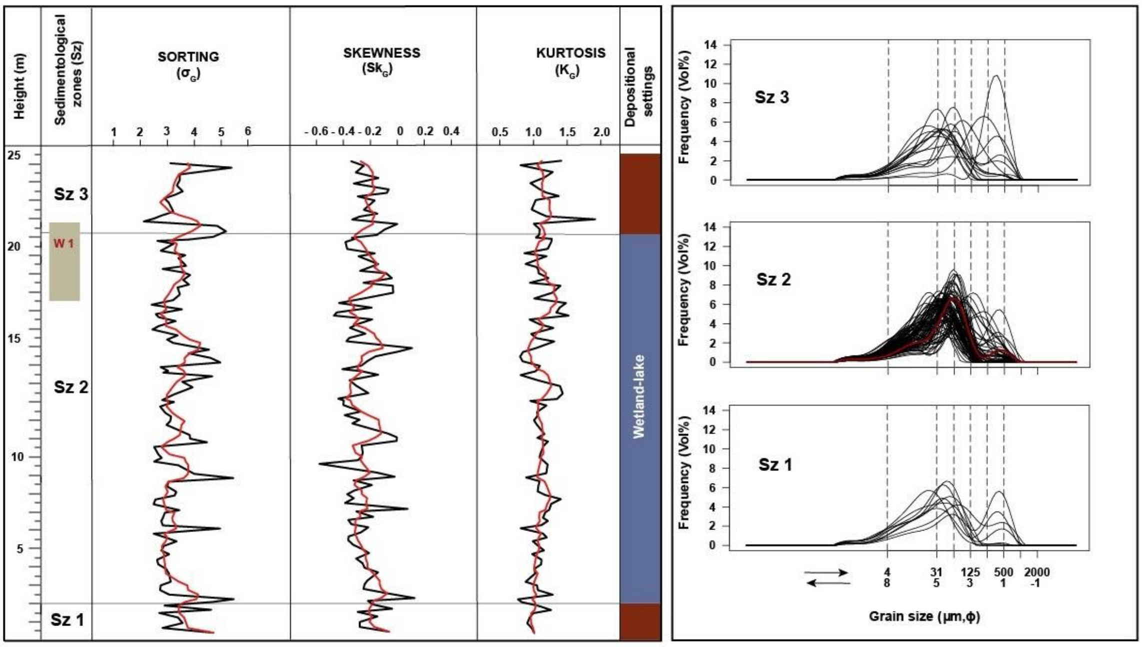

Figure 12.2 *Grain-size parameters (in micrometers) for sediments of T2 (left), presented as raw data (black) and as 5-point running means (red). Grain-size-frequency curves for the three sedimentological zones at right. The red curve represents the sediment of W1*

The sediments are predominantly characterized by unimodal GSDs with occasional occurrence of bimodal ones. The fine fraction (modes at 4.5-11.7 µm) represents the dominant pattern of these GSDs. The sediments are poorly to very poorly sorted, positive (fine-grained) skewed, and mesokurtic. They are partly structureless and show occasional horizontal lamination at 1.4-3.0 m above base. At the base is a 0.4-m thick gravel layer. The recorded ostracod assemblage is dominated by *Limnocythere* sp., and the presence of *Heterocypris salina* probably indicates that sediments formed partly in small temporary water bodies (Meisch, 2000).

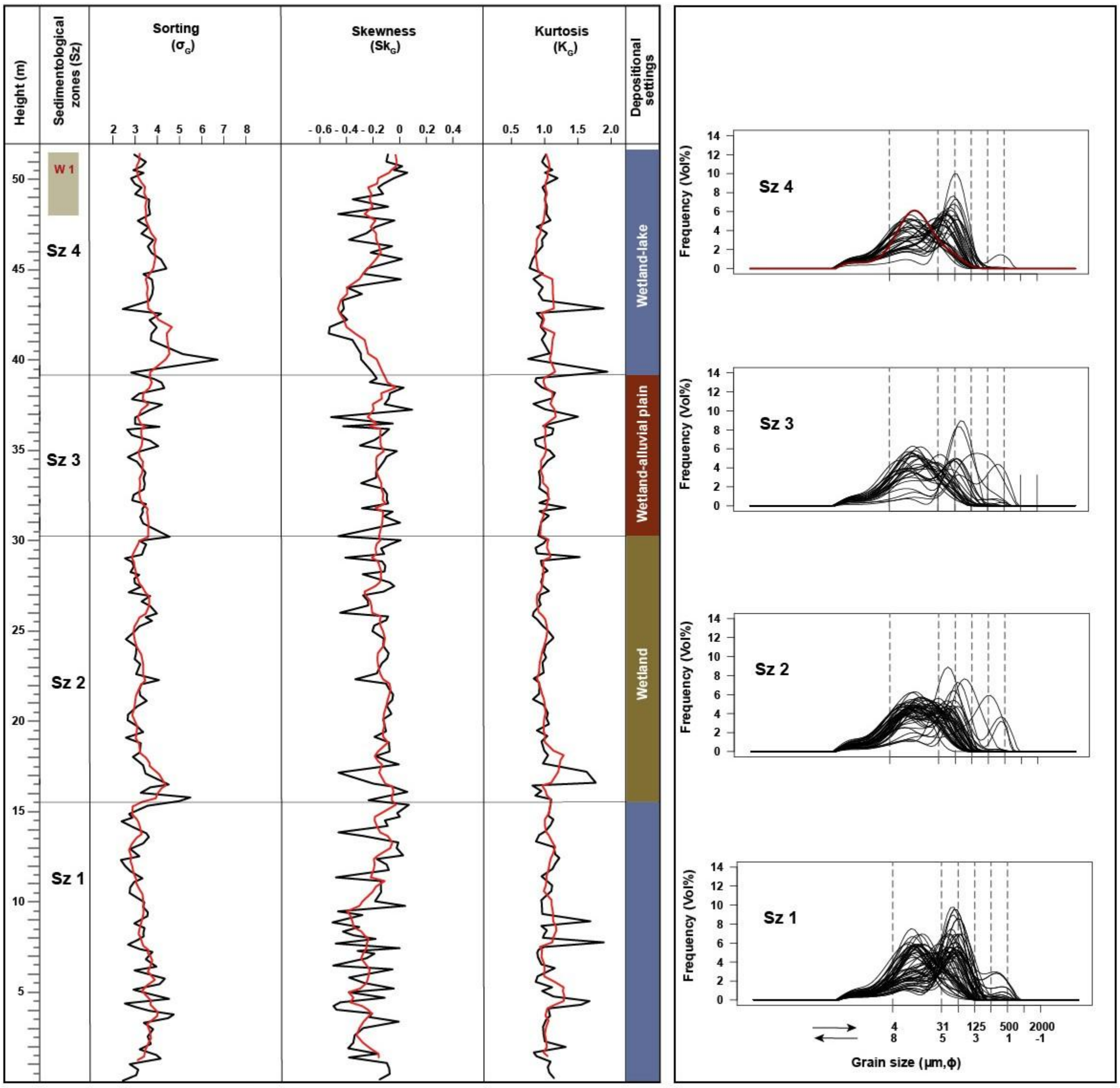

Figure 13.2 *Grain-size parameters (in micrometers) for sediments of T3 (left), presented as raw data (black) and as 5-point running means (red). Grain-size-frequency curves for the four sedimentological zones at right. The red curve represents the sediment of W1*

The sediments of ***Sz 1*** are interpreted as result of fluvial reworking of fine-grained materials of aeolian origin in a densely vegetated paludal environment representing a wetland-alluvial plain depositional setting (cycle 1). The gravels at the base probably resulted from a peak-flow event and the upper sediments of the zone likely represent the settling of fine suspended sediments in a standing water body on the floodplain (Vandenberghe, 2013). The fine-grained characteristics of most of the sediments of ***Sz 1*** are in remarkable contrast to

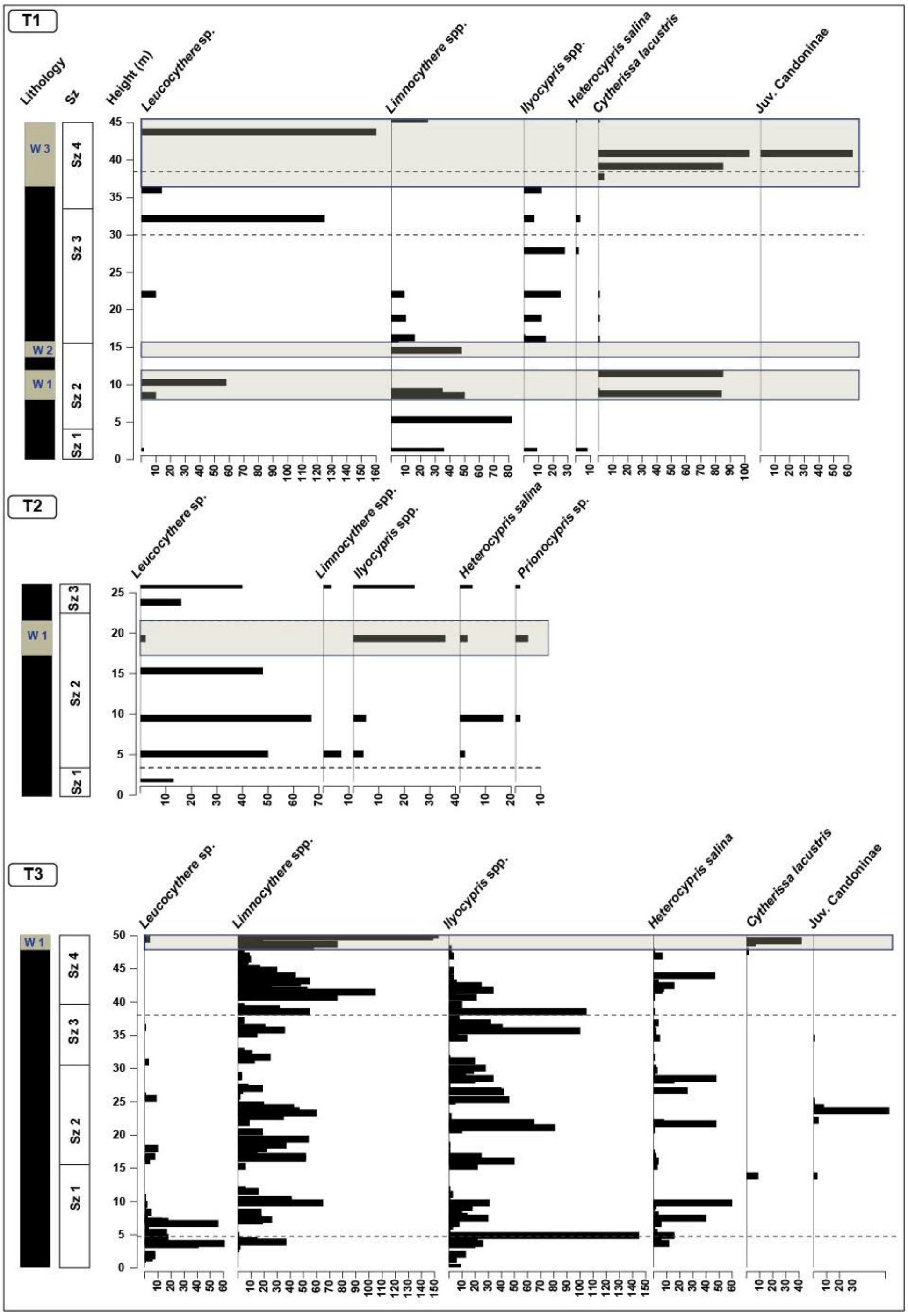

Figure 14.2 *Absolute abundances of ostracod valves per 30 g of sediment recorded at the sediment sections T1 to T3. Valves of Leucocythere spp. include those of L. dorsotuberosa, and valves of Limnocythere include those of L. flexa. Gray horizontal bars indicate the white marker layers*

the relatively pronounced relief at the margins of the Nihewan Basin today, the nearby exposure of bedrock as potential source of sediments and the gravelly deposits in the Sanggan River and in the seasonal streams today.

The mean grain size of these fine-grained sediments of the zone is comparable to the mean grain size of typical loess sediments that vary between 2-25 µm and were called "small dust" by Stuut et al. (2009) and loess type 1.c by Vandenberghe (2013). These fine-grained loess deposits characterize part of the Red Clays in China (Lebbink, 2010). Sun et al. (2018) suggested that loess deposition in NE China began during the early Pleistocene at ca. 1 Ma. According to Liu et al. (2018) the earliest Nihewan Formation sediments were sourced from Early Pliocene Red Clay deposits that were inferred to originate from weathering of aeolian deposits. Noticeably, some samples from T1-section show similar skewness and grain-size patterns to the Red Clay samples collected from Lingtai at the southern CLP (Sun et al. 2006; Fig. 15.2). Additionally, Yang et al. (2019) inferred the partial aeolian origin for the stone artefacts-bearing silt deposits of fluvial terraces of the Hanjiang River at the southern margin of the Qinling Mountains, central China.

The mean grain size of sediments of the ***Sz 2*** **(3.0-15.5 m**) is in a range from fine silt to very fine sand (predominantly medium silt from 8.0-29.2 µm). Unimodal GSDs are dominant in the sediments of this zone and bimodal distributions occur occasionally. The GSDs of the sediments consist of a higher portion of the fine fraction (modes at 7.4-22.6 µm) and a lower portion of the coarse fraction (modes at 41.1-64.5 µm). The sediments are poorly sorted, and predominantly positive (fine-grained) skewed with mesokurtic GSDs. Sedimentary structures are partially present within the zone and include horizontal and ripple lamination and horizontal bedding. Otherwise, the sediments are massive, and deposition probably occurred on a wetland. The sediments at 8.0-12.1 m (W1) and 13.7-15.8 m (W2) heights are brighter coloured and partly carbonate-rich. Similar brighter and carbonate-rich deposits were already recognized as prominent beds by Barbour et al. (1926) and called "white marls". These sediments are characterized by a relatively higher concentration of ostracods (Fig. 14.2). As in ***Sz 1***, *Limnocythere* sp. remains the dominant ostracod taxon, followed by *Cytherissa lacustris* which typically inhibits deep, cold lakes (Meisch, 2000). The horizontal lamination and bedding in ***Sz 2***, and the absence of *H. salina* in contrast to ***Sz 1*** probably indicate a periodic sedimentation of fine and coarse-grained reworked aeolian deposits in a relatively larger water body in comparison to ***Sz 1***. The deposition of white marl sediments likely occurred during a period when a lake was present at the location of the section. In contrast to ***Sz 1***, the occurrence of coarse-grained sediments with modes of GSDs at 41.1-64.5 µm are comparable to the 'large dust' of Stuut et al. (2009) and loess type 1.b of Vandenberghe (2013) which are characterized by modes at 25-65 µm. Thus, the sediments in ***Sz 2*** are interpreted as fluvially reworked, originally aeolian deposits which partly accumulated in a wetland and in a lake (cycle 2).

The mean grain sizes of sediment samples from ***Sz 3*** **(15.5-33.7 m)** range from fine silt to medium sand (mostly medium to coarse silt within 16.3-57.5 µm). Most of the sediments in this zone are marked by the predominance of unimodal GSDs, and bimodal distributions occur occasionally. The sediments are composed of a higher portion of the fine fraction (modes at 7.4-22.6 µm) and a lower portion of the coarse fraction (mode at >65 µm). The sediments are poorly sorted, strongly positive (fine-grained) skewed and leptokurtic. As in ***Sz 2***, horizontal lamination and bedding structures are evident, and cross bedding occurs at 15.8-16.6 m. An erosional surface is distinct near the base of the zone. The sediments of this zone are otherwise massive. They contain fossil bones and preserve traces of burrows left by animals which indicate that the deposition was under wetland conditions. The ostracod assemblage is slightly more diverse in comparison to ***Sz 2***, and the ostracod concentration is lower. The distinctly increased abundance of *Ilyocypris* sp. probably indicates the presence of small ponds and/or slowly flowing streams (Meisch, 2000). Based on the sedimentary characteristics and the ostracods, ***Sz 3*** can be distinguished into two parts that represent more fluctuating conditions first and more stable conditions afterwards. In the lower part (15.5-30.0 m), the dominant massive beds indicate the deposition in a wetland. However, the occurrence of ripple lamination with ostracods such as *Limnocythere* sp. and very few valves of *C. lacustris* indicate sporadically occurring fluvial reworking of locally sourced coarse-grained aeolian deposits and accumulation of transported sediments in a larger water body. The upper part (30.0-33.7 m) is characterized by the presence of horizontal bedding and *Leucocythere* sp. which indicate sediment deposition in small water bodies within a distal floodplain environment. These inferred conditions of ***Sz 3*** could be a result of the deposition in a wetland-alluvial plain setting (cycle 3). The presence of shallow freshwater bodies in this context may have served as a habitat for mammals and their predators. The GSDs of the sediments with mode at >65 µm resemble the modal sizes of nearshore components (C4, C5 and C6) identified in the sediments of Hulun Lake, Inner Mongolia (Xiao et al., 2012).

The mean grain size of sediments in the ***Sz 4*** **(33.7-46.1 m)** varies from fine silt to very fine sand (dominantly medium to coarse silt within 15.8-58.9 µm). Unimodal GSDs prevail in the zone and bimodal distributions occur occasionally. The sediments typically contain a larger fine fraction (modes at ~7.9-22.8 µm) and a smaller coarse fraction (modes at 41.5-65.0 µm). The sediments show poor sorting, and are dominated by positive (fine-grained) skewed, and leptokurtic distributions. As in ***Sz 2***, horizontal lamination and bedding structures are also observed in ***Sz 4***. However, the sediments are mostly homogenous. A brighter-coloured layer at 36.4-46.0 m (W3) above the base contains micritic carbonate. These observed carbonate-rich sediments of the zone represent the third and thickest white marl layer of the section T1. The number of ostracod taxa in ***Sz 4*** is slightly higher and concentrations are also higher than in the previous two zones. *Cytherissa lacustris* occurs at 40.9 m and indicates sediment deposition in a deeper freshwater lake. Valves of Candoninae occur at the same depth, and their members occur in various types of water bodies including lakes and wetlands, often characterised by freshwater and cold conditions (Meisch, 2000). The larger mean grain size of sediments of ***Sz 4*** indicates that sediments accumulated in a setting with higher energy level in contrast to ***Sz 2***. *Ilyocypris and Leucocythere* with low numbers in the lower part of the zone suggest sediment deposition in smaller water bodies on a floodplain. Moreover, a longer, stable period with stagnant waters and carbonate precipitation is inferred from the white marls including a period of sediment accumulation in a deeper lake. Thus, a wetland-lake setting is inferred for ***Sz 4*** (cycle 4).

Section T2

In the T2 section, three sedimentological zones were identified (Fig. 9.2, Fig. 12.2):

The range of mean grain sizes in ***Sz 1*** **(0.0-2.2 m)** varies from coarse silt to very fine sand (mostly medium silt from 24.9-30.2 µm). The sediments are dominantly characterized by unimodal GSDs with occasionally occurring bimodal distributions. The fine fraction (modes at 14.1-25.8 µm) comprises the dominant component of these GSDs. The sediments are poorly sorted, positive (fine-grained) skewed, and mesokurtic. The sediments are poorly sorted, positive (fine-grained) skewed, and mesokurtic. No sedimentary structures are found. At the base of the zone is a 0.6-m thick gravel layer.

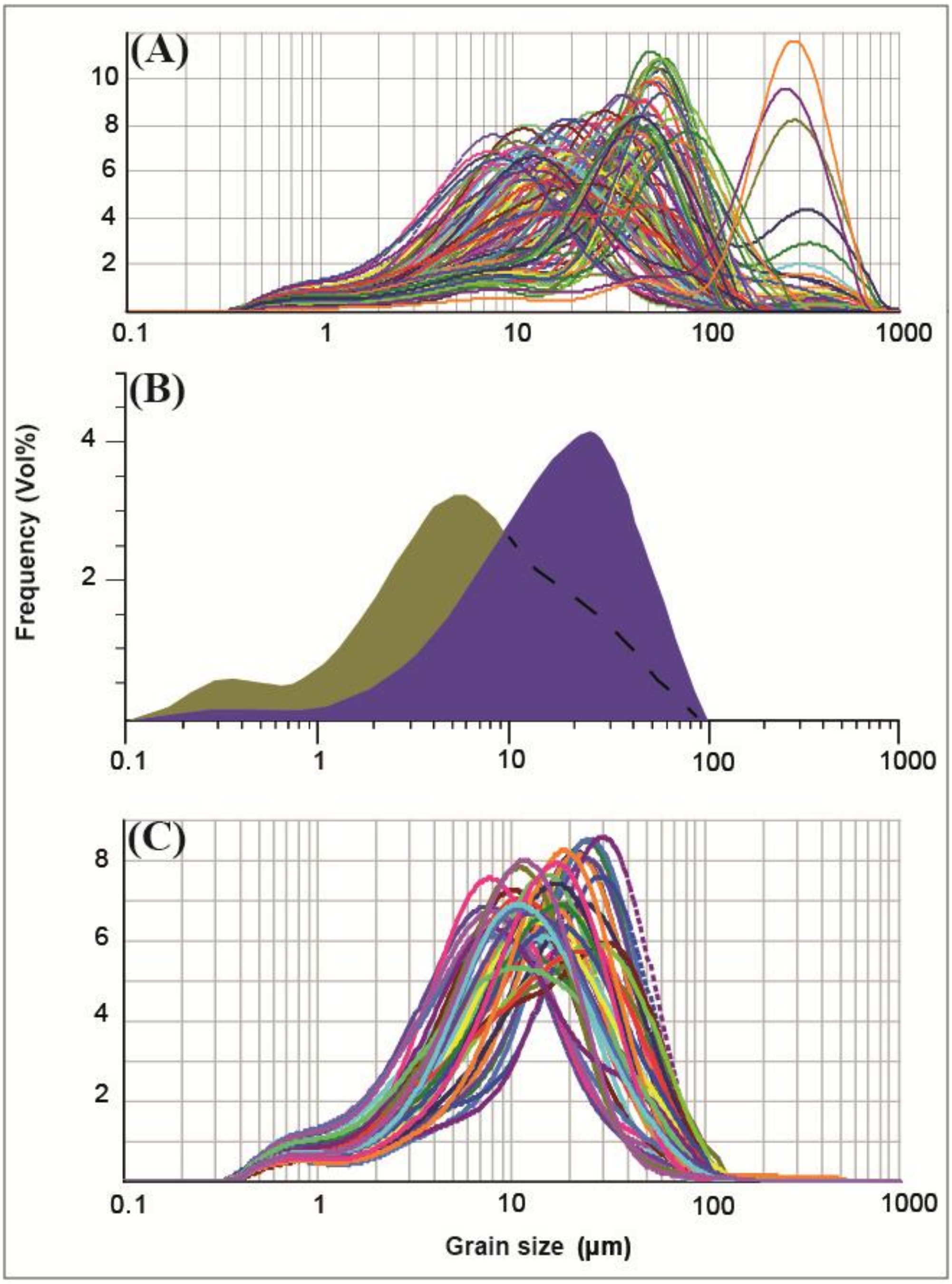

Figure 15.2 *(A) Grain-size-frequency curves for sediments from section T1. (B) Representative grain-size curve of Red Clay (bulk sample in green, quartz fraction in purple) from Lingtai section, S Chinese Loess Plateau redrawn from Sun et al. (2006). (C) Most abundant modes of grain populations at section T1*

The presence of carbonate nodules is recorded in the sediments. A distinct erosional surface can be observed near to the top of the zone. The recorded ostracod assemblage is only represented by *Leucocythere* sp., a taxon possibly adapted to cold climate and rapid hydrochemical fluctuations (Mischke et al., 2008). Valves of *Leucocythere* were identified in surface sediments from shallow water depths between 0.2 and 1.5 m in unstable seasonal ponds (Zhang et al., 2013). The presence of massive beds points to the deposition in a wetland. Nevertheless, the monospecific ostracod assemblage and low abundance of specimens preserved in the sediments of ***Sz 1*** indicate fluvial reworking of fine-grained materials of aeolian origin on an alluvial plain which experienced subaerial exposure from time to time. Thus, the sediments in ***Sz 1*** are interpreted to result from accumulation in a wetland-alluvial plain depositional setting (cycle 1).

The sediments of the ***Sz 2*** **(2.2-22.5 m)** typically have a mean grain size between coarse silt to very fine sand (dominantly medium to coarse silt within 16.0-59.3 µm). Most of the sediments show unimodal GSDs with the occasional occurrence of bimodal distributions. These GSDs are composed of a higher portion of the fine fraction (modes at 5.5-23.2 µm) and a lower content of the coarse fraction (mode at 41.1-62.3 µm). The sediments are poorly sorted, positive (fine-grained) skewed, and they have mainly leptokurtic and mesokurtic distributions. In contrast to ***Sz1***, the sediments of this zone show horizontal lamination and bedding, and ripple lamination structures. The sediments at 17.5-21.8 m (W1) are distinguished by its brighter colour and partly carbonate-rich composition which suggest accumulation in stagnant waters. They also contain carbonate nodules, traces of burrows and other evidence of moderate bioturbation. The brighter layer resembles the white marl layers of T1. Four distinctive erosional surfaces are also recognized, representing individual flooding events. The recorded ostracod assemblage predominantly contains *Leucocythere* sp., and also includes *Ilyocypris* sp. and *H. salina*. The presence of *Prionocypris* sp. indicates slowly flowing streams with abundant vegetation (Meisch, 2000). The collective evidence suggests that the sediments of ***Sz 2*** are fine and coarse-grained reworked aeolian deposits which were mostly deposited in a more stable, low-energy aquatic setting in comparison to ***Sz 1***. Thus, a dominating wetland-lake depositional setting (cycle 2) is inferred which was interrupted from time to time by fluvial conditions.

The mean grain size in the ***Sz 3*** **(22.5-26.0 m*)*** varies from coarse silt to medium sand (mostly medium silt from 18.3-29.0 µm). Unimodal GSDs prevail, and bimodal distributions occur occasionally. The fine fraction (modes at 14.1-27.6 µm) represents the dominant component of these sediments. The sediments show similar sorting, skewness and kurtosis as those of ***Sz 2***. Cross bedding (22.8 m) and horizontal bedding (23.0-25.8 m) occurs but otherwise, sediments are mostly homogeneous. Traces of moderate bioturbation are evident. Ostracod remains are less abundant compared to ***Sz 2***, with *Ilyocypris* sp. as the dominant taxon. The deposition of massive beds and the occurrence of few valves of *H. salina* are indication for wetland conditions. Thus, the characteristics of ***Sz 3*** probably represent sporadic fluvial reworking of fine-grained reworked aeolian materials in a wetland-alluvial plain setting (cycle 3).

Section T3

In the T3 section, four sedimentological zones were identified (Fig. 10.2, Fig. 13.2).

Sz 1 **(0.0-15.5 m)** shows a range of mean grain sizes from fine silt to very fine sand (mostly fine to medium silt within 8.1-27.3 µm). The sediments are dominantly characterized by unimodal GSDs with occasionally occurring bimodal distributions. These GSDs are composed of a higher portion of the fine fraction (modes at 5.5-20.4 µm) and a lower portion of the coarse fraction (modes at 44-58.5 µm). The sediments are poorly sorted, positive (fine-grained) skewed, and mesokurtic. The sediments are mostly homogeneous, which is indicative for the deposition in a wetland. However, horizontal and cross bedding sedimentary structures occur at a few stratigraphic levels within the zone. Carbonate nodules and traces of burrows left by animals are common. The sediments also contain gastropod shells and abundant ostracod valves. *Limnocythere* sp. and *Ilyocypris* sp. are the dominant ostracod taxa. The sediments in this zone might have formed under similar depositional conditions as those of ***Sz 2*** at section T1. Nevertheless, lake conditions at the zone top are marked by the presence of *C. lacustris*. This points to a wetland-lake deposition setting (cycle 1).

The mean grain sizes of sediment samples from ***Sz 2*** **(15.5-30.4 m)** range between fine silt to very fine sand (mostly fine silt from 8.1-15.3 µm). Unimodal GSDs dominate in this zone and bimodal distributions occur occasionally. The fine fraction (modes at 6.7-17.4 µm) comprises the dominant component of these GSDs. The sediments show similar sorting, skewness and kurtosis to ***Sz 1***. The only recognized sedimentary structure is horizontal lamination. However, the sediments are mostly homogeneous and include traces of burrows left by animals which are evidence for wetland conditions. A distinct erosional surface at 16.3 m probably results from a flooding event. The sediments in this zone contain remains of gastropods and a relatively higher concentration of ostracods compared with ***Sz 1***. The recorded ostracod assemblage is dominated by *Limnocythere* sp. and *Ilyocypris* sp. Valves of Candoninae and *H. salina* are also present. The collected evidence indicates a gentle and periodic deposition of reworked fine-grained suspended aeolian materials in a large, shallow and vegetated standing water body on a low-energy alluvial plain environment. Thus, deposition is interpreted to have occurred in a wetland setting (cycle 2).

The mean grain sizes of sediment samples from ***Sz 3*** **(30.4-39.3 m)** are within a range from medium silt to fine sand (mostly fine silt from 8.8-15.5 µm). Most of the sediments in this zone show unimodal GSDs with the occasional occurrence of bimodal ones. The fine fraction (modes at 6.1- 17.6 µm) is the dominant pattern in these GSDs. The sediments show similar sorting, skewness and kurtosis similar to ***Sz 2***. Horizontal lamination, cross bedding and ripple marks are evident. Other sedimentary structures include traces of intensive bioturbation. Five distinctive erosional surfaces are recorded within the sediments. There is a decrease in the ostracod concentration than in ***Sz 2***. The recorded ostracod assemblage is dominated by *Limnocythere* sp. and *Ilyocypris* sp. with a significant decrease in the concentration of *H. salina*. This may reflect similar depositional conditions to the sediments of ***Sz 1*** at section T1. Thus, deposition in a wetland-alluvial plain setting is inferred (cycle 3).

The sediments of the ***Sz 4*** **(39.3-50.5 m)** typically have a mean grain size between fine silt to very fine sand (mostly fine silt from 8.7-14.8 µm). Unimodal GSDs are dominant with the occasional occurrence of bimodal distributions. These GSDs are dominantly composed of the fine fraction (modes at 5.2-16.6 µm). The sediments show similar sorting, skewness and kurtosis as those of ***Sz 3***. Horizontal lamination and ripple marks are found. The sediments in this zone include traces of intensive bioturbation at 46.5 m. The sediments at the height of 48.15-50.85 m (W1), are relatively similar to that was described in ***Sz 2*** of section T1 as (W1 and W2). Moreover, a relatively higher concentration of ostracods is present in these sediments of this zone compared to those of ***Sz 3***. The recorded ostracod assemblage is dominated by *Limnocythere* sp. and *Ilyocypris* sp., and *H. salina* is present too. In contrast to ***Sz 2***, these sediments were likely deposited in larger and deeper ponds under low-energy conditions in topographically lower areas of alluvial settings. The distinct presence of *C. lacustris* at 49.5 m in the prominent brighter-coloured layer likely represents a period of lacustrine deposition at larger water depth. The majority of the sediments of ***Sz 4*** were formed in a wetland-lake depositional setting.

White marl deposits

The T1 section contains three distinct white marl layers (W1-W3). They lack bedding structures and are mainly composed of fine groundmass of micritic carbonate. They also contain disseminated angular inorganic detrital constituents (mostly quartz and feldspar grains) with the absence of skeletal grains (> 1 mm; Fig. 16.2). This supports the in situ-formation of these carbonate-rich sediments. It indicates that these sediments were likely deposited in low-energy aquatic conditions. The marl sediments are, therefore, lacustrine or paludal origin. The mean grain size of the non-calcareous sediments of W1 is between fine to medium silt (mostly fine silt 8.3-23.0 μm). They are poorly sorted, and the GSDs are mostly positive (fine-grained) skewed and mesokurtic. Sediments of W2 show mean grain size between fine to medium silt (mostly medium silt 13.9-29.2 μm). They are poorly sorted, and the GSDs are mostly positive (fine-grained) skewed and leptokurtic. The mean grain size of sediments of W3 is between fine to coarse silt (mostly coarse silt 10.8-51.8 μm). It is poorly sorted, and the GSDs are mostly strongly positive (fine-grained) skewed and leptokurtic. All three layers show low MS and FDMS. The monospecific assemblage of *C. lacustris* was exclusively recorded in these layers. The ostracod assemblage indicates that the deposition of the marl sediments occurred in a deep lacustrine setting (Meisch, 2000).

In the T2 section, there is a similar white marl layer without bedding structures which represents in situ-formed micritic carbonate. The mean grain size of the layer is between medium silt to very fine sand (mostly coarse silt 18.5-81.8 μm). It is poorly sorted and has mostly positive to strongly positive (fine-grained) skewed and leptokurtic GSDs. Also here, the white marl has low MS and FDMS. The recorded ostracod assemblage in this layer is dominated by *Ilyocypris* sp., accompanied by valves of *Leucocythere* sp., *H. salina* and *Prionocypris* sp. The assemblage indicates that paludal conditions prevailed during the formation of this white marl layer. We first correlate the T1-T3 sections using their elevations above sea level, specifically the height positions of the white marl layers (Fig. 17.2). The presence of a distinctive erosional surface near to the top of the white layer in T2 can be reasonably correlated with a similar surface near the top of W2 at section T1 which marks a period of significant erosion (Fig. 8.2). Similarly, the base of this layer likely correlates with the base of W1 at section T1 due to the nearly equal thickness of the two layers W1 and W2 in T1. Alternatively, the white marl in T2 could theoretically be correlated to every white marl layer in T1 based on the nearly similar grain size and magnetic susceptibility. The recognized ostracod assemblage of the white marl layers in T1, dominated by either *C. lacustris* or *Limnocythere* spp., differs from the assemblage of the white marl layer in section T2, dominated by *Ilyocypris* spp. (Fig. 14.2). However, such difference possibly results from slight habitat differences within the lake environment during the deposition of the sediments of the sections T1 and T2 which occurred probably less closely spaced than their vicinity implies today assuming that the horizontal component of displacement along the Youfang Fault was not insignificant (Deng et al., 2008; Ao et al., 2013b; Fig. 6.2, Fig. 7.2). The originally larger distance between the accumulation areas of sections T1 and T2 is also supported by the relatively coarser-grained sediments of the section T2 not only in comparison to those of section T1 but also of section T3. We favor the correlation of the white layer in section T2 with layer W1 and/or W2 in section T1 based on the more comparable thicknesses of these layers and their vertical position taking the assumed vertical displacement along the Youfang Fault of ca. 30 m into account (Deng et al., 2008; Fig. 17.2).

The T3 section also contains one distinct white marl layer which does not include bedding structures and constitutes in situ-formed micritic carbonate. The mean grain size is mostly fine silt (8.7-10.8 µm). Sediments are poorly sorted, and GSDs are mostly near symmetrical and mesokurtic. As all the white marl layers, low MS and moderate FDMS were recorded. The ostracod assemblage only contains *C. lacustris* valves which indicate a deep lacustrine depositional environment. This white layer can be easily traced across the sampling location with W1 at section T1 with the absence of erosional surface or any stratigraphic breaks. Furthermore, both show good correlation in the mean grain size and MS patterns (Fig. 8.2, Fig. 10.2). Additionally, the ostracod assemblages are more or less identical and strongly support the correlation (Fig. 14.2). The alternative correlations of the white marl layer in section T3 with W2 or W3 in section T1 have some drawbacks either due to the different topographic position or the significant differences in the ostracod assemblages (Fig. 14.2). In addition, the lithologically distinct and varicoloured beds of the three sediment sections T1, T2 and T3 exhibit lateral continuity in the partially exposed sediments in between these sections along the Dachangliang mountain ridge. Specifically, lateral continuity of the prominent white marl layers, being apparently consistent and correlative throughout sections, permits the T1-T3 sediments to be stratigraphically and lithologically correlated (Fig. 17.2). The ostracod assemblages of the white layers further support the correlation between the T1-T3 sections using the colour of the sediments and the presence of carbonate in these layers. These inferences permit the establishment of a 86.2-m thick, more or less continuous synthetic composite sedimentary section (NH-T) with six sedimentological zones (Fig. 17.2).

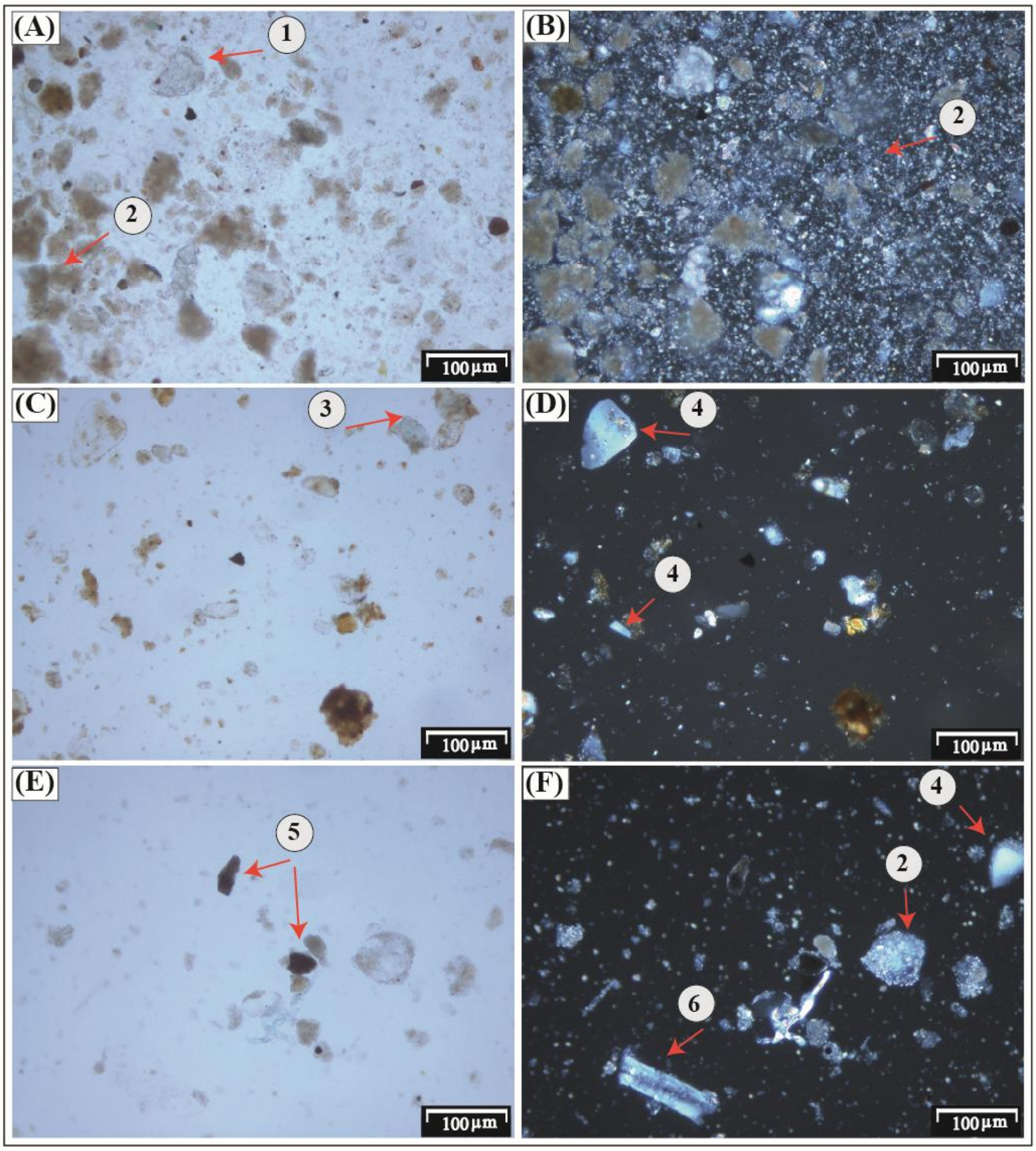

Figure 16.2 *Photomicrographs of the mineral constituents encountered in the white layers (W1-W3). All figures were taken at ×50 magnification under transmitted white light. Figures (A, C, E) were in plane-polarized light, and (B, D, F) were in cross-polarized light, and (B, D, F) were in cross-polarized light. 1) lithoclast of limestone, 2) micritic carbonate 3) carbonate-coated quartz grain or rock fragment 4) quartz grain, 5) rock fragments, 6) weathered feldspar grain*

2.5.2 Depositional cycles and palaeoenvironment of the Dachangliang (DCL) section during ca. 1.7-0.9 Ma

In the study area, the vertical sediment succession of the NH-T section shows minor changes in grain size with recognizable variations in sediment colour, bedding structures, magnetic mineral concentrations, and the presence of ostracods. Therefore, these variations in sediment characteristics and faunal composition suggest a clear vertical sequence of six depositional settings (Fig. 18.2). Thus, the depositional environment at NH-T section represents six cycles of changing hydrodynamic conditions from 1) wetland and lake, 2) wetland, 3) wetland and alluvial plain, 4) wetland and lake, 5) wetland and alluvial plain, and ultimately, 6) wetland and lake. NH-T cycles obey Walther's Law (Walther, 1894) and possibly occurred side-by-side spatially.

The first sedimentary cycle (0.0-15.5 m) represents the dominance of a wetland environment replaced by abrupt episode of alluvial plain (3.5 m) and a shallow ephemeral lake (14.0 m). The second cycle (15.5-30.4 m) marks a distinct period of stable wetland setting. The third cycle (30.4-39.3 m) is a transitional phase of increased fluvial activity and gradual reduction in wetland setting. Sediments of the fourth cycle (39.3-57.5 m) probably deposited in different environmental conditions of a wetland to shallow ephemeral lake setting including periods of deeper lake facies. The fifth cycle (57.5-79.0 m) is characterized by a thicker stratigraphic interval of wetland-alluvial plain sediments in comparison with the third cycle. The sixth cycle (79.0-86.2 m) represents changing conditions from wetland to shallow ephemeral lake settings including periods of deeper lake facies similar to the sedimentary patterns of the fourth cycle.

The general assessment of the late Cenozoic sedimentary evolution of the Nihewan Basin by Chen et al. (2015) implied three stages of rapid expansion, contraction and extinction of the basin during 3.6-2.6 Ma, 2.6-1.8 Ma and 1.8 to 0.11 Ma, respectively. They also suggested that the Pleistocene sediments near the northeastern margin of the basin were mainly deposited in a braided river (Nihewan Formation, 2.15-1.8 Ma) to alluvial fan environment (Xiaodukou Formation, 1.8-0.2 Ma; Chen et al., 2015). A braided river setting in the region agrees with our inference of mostly wetland conditions at the NH-T section. Nevertheless, the sporadically recorded lake beds show an upward-fining trend from

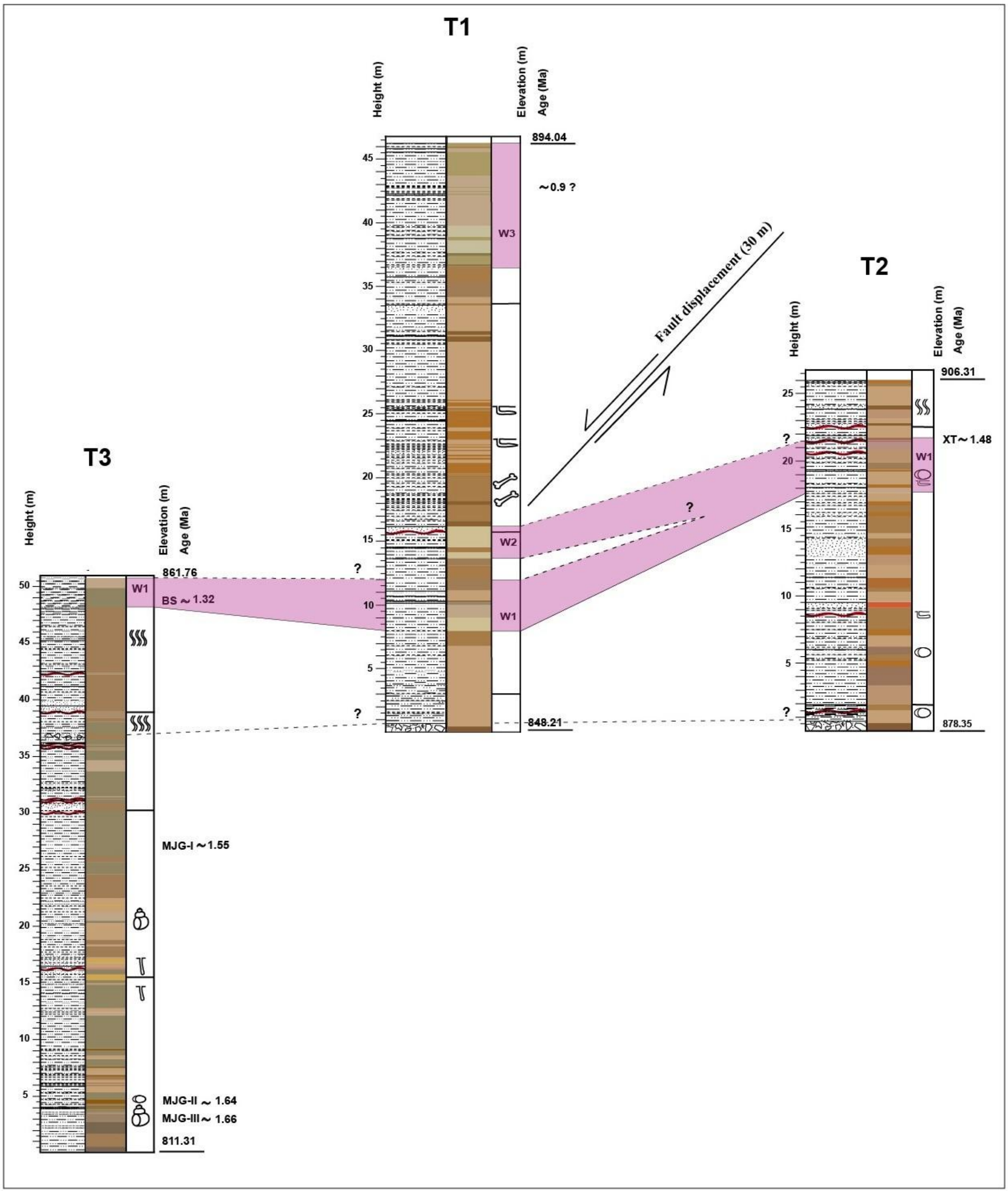

Figure 17.2 *Stratigraphic correlation of the sediment sections T1 to T3. Positions of four horizons in section T3 and one horizon in section T2 are linked stratigraphically to neighbouring artefact-bearing layers previously dated at Majuangou (MJG) and Xiantai (XT; Zhu et al., 2004; Ao et al., 2010)*

shallower deposits near the section base to deeper and thicker deposits towards the top during ca. 1.7 to 0.9 Ma. In contrast, Zhu et al. (2004) suggested that the depositional environment at MJG (1.66 to 1.32 Ma) was lacustrine with brief intervals of wetland and lake-margin settings which is comparable with the inference of wetland and lake facies associations of cycles 1 and 2 at the lower part of NH-T. Both MJG and NH-T sections are located near the eastern margin of the basin, and their sediments are well correlated by three distinctive coloured layers (red, gray and yellow), although our multi-proxy study indicates that sediments mostly represent wetland deposits rather than prevailing lacustrine conditions (Zhu et al. 2004). Yang et al. (2022) suggested a shallow lacustrine environment during hominin activity (1.324-1.317 Ma) at the Banshan site, which later experienced lake expansion and lake-level rise (1.318-1.310 Ma). This aligns with our interpretation of the facies association of cycle 4, including wetland, shallow and deep lake deposits. Li et al. (2008) investigated the XDK section in the basin center and also at Donggutuo and Xiaochangliang sections near the eastern margin of the basin and inferred a river-dominated to a lake depositional setting for their cycle II which resembles the cycles 5 and 6 of the NH-T section. Bi et al. (2022) inferred that the Datong Basin, located to the west of the Nihewan Basin, underwent a transition from dominant fluvial conditions (7.0-4.2 Ma) to the development of lacustrine environments (4.2-1.8 Ma) due to dip-slip fault activities, and ultimately, a gradual shrinkage of the lake after 1.8 Ma.

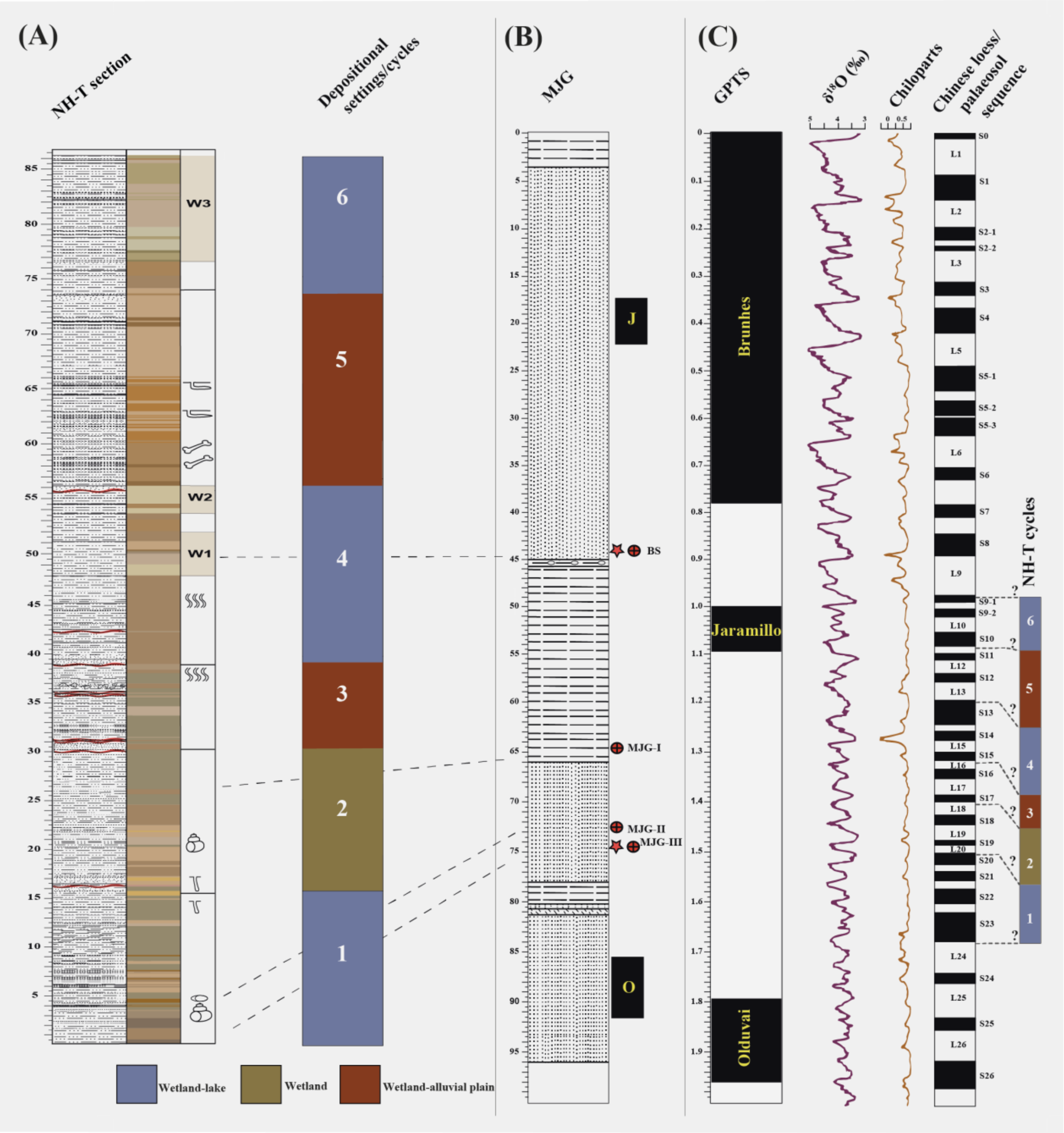

Figure 18.2 (A) Depositional settings in the Nihewan Basin during the Early Pleistocene. (B) Stratigraphic section of MJG redrawn from Zhu et al. (2004). (C) Geomagnetic Polarity Time Scale (GPTS) by Hilgen et al. (2012), in comparison with climate records in the in the region: stacked benthic $\delta^{18}O$ record (Lisiecki and Raymo, 2005), Chinese loess Chiloparts timescale (Ding et al., 2002), and Chinese loess/palaeosol sequence (L loess, S palaeosol) by Liu et al. (1985)

2.5.3 Implications for the reconstruction of Early Pleistocene climate change in the Nihewan Basin

Considering that the sediments of the NH-T section probably formed between 1.7 to 0.9 Ma, we identified patterns of sedimentary facies types A and B which are indicative of wetter conditions, while facies type C marks drier conditions (Figs. 8.2-10.2). The three facies types A, B and C are defined on the basis of lithology as silt, sandy silt and silty sand, respectively. The facies code range (1-7) at each type are ascendingly sorted from unimodal to trimodal grain-size distribution curves. Additionally, three dominant fine- to coarse silt-sized components and the ostracod-assemblage changes were observed in the sediments. These observations collectively suggest three distinct cycles 1, 4 and 6 as indicative periods of warmer and wetter climate, whilst cycles 2, 3 and 5 represent three periods of colder and drier climate. The NH-T section is ca. 90 m thick, and sediments likely formed over a period of ca. 800 ka. Assuming that the sediment accumulation occurred relatively constantly without major changes of the depositional rate, sedimentary cycles of 15 to 20 m thickness may represent periods of roughly 150 ka. Thus, the cycles inferred for the NH-T section possibly represent several long-term climatic fluctuations. In the early Pleistocene, astronomically driven global glacial-interglacial cycles (Milankovitch cycles) had periodicities of ca. 41-ka (Ruddiman et al., 1989). We may speculate that cycles of roughly 150-ka duration at the NH-T section may represent four of such global glacial-interglacial cycles. The Quaternary loess sequences of the CLP recorded long-term glacial-interglacial fluctuations as loess-soil couplets, probably most appropriate to attempt a correlation of the NH-T section with a long-term record of global climate change due to their proximal geographic location in the southwest of the Nihewan Basin.

Our detailed assessment of the NH-T sediment characteristics is typically not available for similar sections in the region. Results of the sedimentological analysis indicate only few minor flooding events and do not include significant evidence for high-energy deposits formed in the river channel. These findings suggest that larger parts of the section probably experienced only limited influence by the dynamic changes of the Sanggan River course. Thus, we argue that the sediments are rather indicative of regional climate conditions over the estimated period. The wetland-lake settings inferred from NH-T probably suggest prevailing warm and wetter conditions resulting from a stronger East Asian Summer monsoon. These conditions likely correspond to the interglacial periods S_{23}-S_{20}, S_{15}-S_{13} and S_{10}-S_9 which were previously inferred from paleoclimatic records from CLP (Ding et al., 2002; Fig. 18.2). Conversely, the inferred wetland-alluvial plain settings in the NH-T section are probably contemporaneous with the predominantly cooler and drier conditions of the glacial periods L_{20}-L_{18}, L_{17}-L_{16} and L_{13}-L_{11} (Fig. 18.2). Nevertheless, the occasionally recorded influx of coarsest sediment type C represents brief episodes of the coolest and driest conditions, predominantly observed within the wetland-alluvial plain settings (Figs. 8.2-10.2).

Meng et al. (2018) studied dolomite and calcite contents of three sediment sections on the CLP as proxies of rainfall-controlled carbonate dissolution to reconstruct East Asian summer monsoon (EASM) rainfall intensity. Their findings show an overall increasing trend of interglacial EASM rainfall from 1.65 Ma to 0.5 Ma which is apparently supported by our observed upward increases in the thickness of white marl layers in the NH-T section. The warm cycles 1, 4 and 6 at NH-T section probably correspond to three inferred warm periods reflected by high MS in the unit from 1.66-1.55 Ma of the XT section (Ao et al., 2010), recorded by pollen data at the BS site (1.324-1.310 Ma; Yang et al., 2022) and as the upper lacustrine deposits (stage 3) of the XDK section (Li et al., 2008), respectively. Magnetite and hematite were identified as the dominant ferrimagnetic minerals in the eastern Nihewan Basin by Ao et al. (2009) and Liu et al. (2018). Olive green/pale-brown silts of the NH-T section have low MS values, whilst yellowish-brown silts/fine sands have typically high MS values. The higher MS values of the sand-dominated layers probably result from the redeposition of pedogenized loess and soils that were eroded and transported in the catchment during interglacials (Wang et al., 2008). Through the NH-T section, the χ_{FD} values are predominantly characterized by low and relatively constant values < 2 % which suggests the absence of paramagnetic grains influenced by Fe-reducing bacteria in soils (Dearing, 1999). Occasionally, there are moderate values between 2-11.4 %, indicating soil formation and the incorporation of pedogenic ultrafine magnetite/maghemite grains into the NH-T sediments. The rarely higher χ_{FD} values > 16 % are observed in the inferred wetland and wetland-lake settings, indicating intensified soil formation and related warmer and wetter conditions when soil-derived particles were washed to wetlands and lakes. In contrast, the few high peaks observed in the inferred wetland-alluvial plain settings probably indicate soil erosion during colder climate conditions. For the corresponding drier intervals, Ao et al. (2009) reported an increased cooling coupled with an intensified aridification for the neighbouring XT section during 1.9-0.1 Ma, with low MS in the unit from 1.54-1.45 Ma as investigated by Ao et al. (2010) which probably corresponds to the cooler cycles 2, 3 at NH-T section. The pollen record from the Jinyuan Cave in NE China is characterized by a cooling and drying trend with large fluctuations from ca. 2.0 to 0.4 Ma and a transition from forest to forest-steppe vegetation between 1.7 and 1.5 Ma to the dominance of forest steppe until the Mid-Pleistocene Transition between 1.2 to 0.7 Ma (Shen et al., 2021). East Africa has experienced progressive aridification over the past few million years with precession-paced environmental shifts from closed forested ecosystems to open grassland ecosystems driven by moisture availability (Magill et al., 2013a, 2013b). Thus, the available evidence suggests that the high-latitude Nihewan Basin was characterized by significant environmental and long-term climatic fluctuations during the Early Pleistocene ca. 1.7 to 0.9 Ma. Therefore, early hominins apparently inhabited the environment of the Nihewan Basin from 1.66 to 0.78 Ma (Zhu et al., 2007), but probably not year-round or during cold periods (Dennell, 2013).

2.7 Conclusions

The exposed sediments of three sections T1-T3 (up to 50-m thick) in NE Nihewan Basin predominantly comprise varicoloured reworked silt-sized materials of aeolian origin, partially interbedded with calcareous and fine-grained sand layers and minor contributions of clay-sized particles. Laminations of variable thickness, horizontal and ripple bedding, and bioturbation features have been recorded. Most of the sediments show unimodal GSDs with the occasional occurrence of bimodal and trimodal distributions. The sediments are poorly sorted, positive (fine-grained) skewed, and characterized by mesokurtic and leptokurtic distributions. MS values of the sediment are generally low, and higher values were determined for the coarser-grained sediments. The recorded ostracod assemblages of the sediments are dominated by *Limnocythere* sp., *Ilyocypris* sp. and *Leucocythere* sp. The sediments also contain remains of gastropod shells. Prominent marker beds of white marl are apparently consistent and correlative throughout sections. Valves of *C. lacustris* were exclusively found in these white marl layers that support the correlation between the T1-T3 sections using the colour of the sediments and the presence of in situ-formed micritic carbonate in these beds. The correlation allowed to build a synthetic composite sedimentary section of 86.2-m thickness (NH-T) that was probably formed between ca. 1.7 and 0.9 Ma. Evidence from sedimentological and ostracod-assemblage data of the composite NH-T section suggests six remarkable depositional cycles of changing hydrodynamic conditions between dominantly a wetland with periods of lake and alluvial plain settings. The identified cycles evolve sequentially from 1) wetland and lake, 2) wetland, 3) wetland and alluvial plain, 4) wetland and lake, 5) wetland and alluvial plain, and ultimately, 6) wetland and lake conditions. This suggests that the high-latitude Nihewan Basin was characterized by significant environmental fluctuations during the time frame of the sediments studied here. The climate variability of Early Pleistocene is traced by three dominant grain-size components and ostracod-assemblage changes in the studied sediments. Three intervals of warmer and wetter climate and three intervals of colder and dryer climate are inferred. The inferred climate cycles likely represent climatic changes associated with astronomical (Milankovitch) forcing. Nevertheless, an independent age model was not yet established for our sediment sections at Dachangliang, and further correlations with earlier studied sedimentary sequences with established magnetostratigraphy in the region will improve the chronological framework of inferred climate conditions. Furthermore, new analyses of sediments from additional sections within the eastern Nihewan Basin have good potential to better understand the cyclicity of environmental and landscape change in the basin during the Early Pleistocene.

2.8 Supplementary information

Table 1 *Litho- and bio-facies characteristics of the T1 section*

Sz	Height (m)	Sediment type	Grain-size parameters	Colour	Bedding [a]	MS & FDMS	ostracod valves /30 g	Interpretation
4	33.7-46	– Primarily coarse to very coarse silt, with less abundant medium silt and rarely very fine sand, containing carbonate at 36.4-46 m (W3)	– Primarily unimodal, with occasionally bimodal GSDS – Main mode is fine (7.9-22.8 µm), with less abundant coarse mode (41.5-65 µm), and rare modes at >65 µm – Primarily poorly and rarely very poorly with one bed of moderately sorted sediments at 35.8-36 m – Primarily positive (fine-grained) to strongly positive (fine-grained) skewed (pfs) with sporadically near symmetrical (ns), and rarely negative (coarse-grained) skewed (ncs) GSDS – Primarily leptokurtic, with less abundant mesokurtic and very leptokurtic	– Primarily pale yellow and light gray, with occasionally light yellowish brown, and rarely white, pale brown, pale olive, and very pale brown	– HB at 35 m, 36.4-45.6 m – RL at 35.5-36.4 m	– Low MS (<2) – Primarily low (< 2), with occasionally moderate FDMS (2-5.5)	– Leuc (174) – Limn (25) – Ilyo (12) – H-sal (1) – C-lac (188) – Cand (63)	Mixture of fluvio-aeolian and Lacustro-aeolian facies
3	15.5-33.7	– Primarily coarse to very coarse silt, with less abundant medium silt, and rarely fine to very fine sand and medium sand	– Primarily unimodal, with occasionally bimodal, and one bed of trimodal GSDS at 33.4 m – Main mode is fine (7.4-22.6 µm), with less abundant coarse mode (>65 µm), and rare modes at 41.1-64.5 µm. – Primarily poorly, with rarely very poorly sorted sediments – Primarily strongly pfs with less abundant pfs and ns GSDS – Primarily leptokurtic with less abundant mesokurtic, and occasionally very leptokurtic	– Primarily very pale brown, brownish yellow, and light yellowish brown, with rarely yellowish brown	– HB at 27-33.5 m – RL at 17-18.3 m, 21.2-22.1 m, and 22.6-23.9 m. – XB at 15.8-16.6 m	– Low MS (<2) – Primarily low (< 2), with occasionally moderate FDMS (2-4.5)	– Leuc (135) – Limn (40) – Ilyo (88) – H-sal (5) – C-lac (3)	Fluvio-aeolian facies
2	3.0-15.5	– Primarily medium-coarse silt, with sporadically fine and very coarse	– Primarily unimodal, with occasionally bimodal, and one bed of trimodal GSDS at 3.3 m	– Primarily very pale to pale brown, light yellowish brown and pale yellow, with occasionally	– HL at 10-11.2 m – HB at 4.8-8.0 m, and	– Low MS (<2) – Primarily low (< 2), with	– Leuc (68) – Limn (215) – C-lac (169)	Mixture of fluvio-aeolian and Lacustro-aeolian facies

		silt, and rarely very fine sand, containing carbonate at 8.0-12.1 m (W1) and 13.7-15.8 m (W2)	– Main mode is fine (7.4-22.6 µm), and less abundant coarse mode (>65 µm), with rare modes at 41.1-64.5 µm – Primarily poorly, with occasionally very poorly sorted sediments – Primarily pfs to strongly pfs with ns, and rarely ncs GSDS – Primarily mesokurtic and less abundant leptokurtic and platykurtic	brownish yellow, yellowish brown, light gray, light olive gray, and light olive brown	13.6-15.1 m – RB at 8 m	occasionally moderate FDMS (2-5.9)		
1	0.0-3.0	– Primarily medium silt, with occasionally fine, coarse, and very coarse silt – Reddish-brownish rounded and sub-angular gravel layer, with limestone (white particles) at the bottom	– Primarily unimodal, with occasionally bimodal GSDS – Main mode is fine (4.5-11.7 µm), with rare modes at 56.1 µm and >65 µm – Primarily poorly and rarely very poorly sorted sediments – Occasional occurrences of pfs to strongly pfs and ns GSDS – Primarily mesokurtic and less abundant platykurtic and leptokurtic sediments	– Very pale brown	– HL at 1.4-3.0 m	– Low MS (<2) – Primarily low (< 2), with occasionally moderate FDMS (2-11.4)	– Leuc (2) – Limn (36) – Ilyo (9) – H-sal (8)	Fluvio-aeolian facies

[a] The sediments are otherwise homogeneous.

***Table 2** Litho- and bio-facies characteristics of the T2 section*

Sz	Height (m)	Sediment type	Grain-size parameters	Colour	Bedding [a]	MS&FDMS	ostracod valves /30 g	Interpretation
3	22.5-26.0	– Primarily coarse silt, with less abundant very fine to fine sand, and rarely very coarse silt and medium sand	– Primarily unimodal, with occasionally bimodal GSDSs between 25.3-26 m – Main mode is fine (14.1-27.6 µm), with rare modes at 50.5->65 µm – Primarily poorly, with one bed of very poorly sorted sediments at 25.7 m – Primarily pfs with less abundant strongly pfs GSDS	– Primarily pink, very pale brown, light yellowish brown with rarely yellowish brown, brownish yellow and light reddish	– HB at 23.0 - 25.8 m – XB at 22.8 m	– Low MS (<2) – Low FDMS (< 2)	– Leuc (56) – Limn (3) – Ilyo (24) – H-sal (5) – Prio (2)	Fluvio-aeolian facies

			– Primarily leptokurtic with less abundant mesokurtic, and rarely very leptokurtic and platykurtic					
2	2.2-22.5	– Primarily coarse-very coarse silt with sporadic very fine sand, containing carbonate at 19.7 m (W1)	– Primarily unimodal, with occasionally bimodal and one bed of trimodal GSDS at 22.2 m – Main mode is fine (5.5-23.2 µm), and less abundant coarse mode (41.1-62.3 µm), with occasional modes at >65 µm – Primarily poorly, with rarely very poorly sorted sediments – Primarily pfs to strongly pfs, with rarely ns GSDS – Primarily leptokurtic and mesokurtic, with rarely platykurtic and one bed of very leptokurtic at 17.6 m	– Primarily very pale to pale brown, light yellowish brown and brownish yellow, with occasionally pink, light brown and rarely light reddish brown, light gray, light red, reddish yellow, and pale red	– HB at 5.8-8.2 m, 12.4-14.7 m, and 17.5-22 m. – HL at 5.3 m, and 21 m – RL at 9 m – RB at 16.2 m – FT at 21.6 to 21.8 m	– Low MS (<2) – Primarily low (< 2), with occasionally moderate FDMS (2-5.4)	– Leuc (167) – Limn (7) – Ilyo (45) – H-sal (22) – Prio (7)	Mixture of fluvio-aeolian and Lacustro-aeolian facies
1	0.0-2.2	– Primarily coarse silt, with rarely very fine sand – Single-grained rounded gravel layer and weathered conglomerate rock at uppermost part of basement	– Primarily unimodal, with occasionally bimodal GSDS – Main mode is fine (14.1-25.8 µm), with rarely modes at >65 µm – Primarily poorly, with rarely very poorly sorted sediments – Primarily pfs, with rarely strongly pfs and ns GSDS – Primarily mesokurtic and rarely platykurtic and leptokurtic	– Primarily pale brown with rarely light yellowish brown and pink		– Primarily moderate MS (2-5.3) and rarely low MS (<2) – Primarily low (< 2), with one bed of moderate FDMS (3.8)	– Leuc (13)	Fluvio-aeolian facies

[a] The sediments are homogeneous otherwise.

***Table 3** Litho- and bio-facies characteristics of the T3 section.*

Sz	Height (m)	Sediment type	Grain-size parameters	Colour	Bedding [a]	MS&FSMS	ostracod valves /30 g	Interpretation
4	39.3- 50.5	– Primarily medium-coarse silt, with one bed of very coarse silt, containing carbonate at 49.5 m (W1)	– Primarily unimodal, with occasionally bimodal, and one bed of trimodal GSDS at the base – Main mode is fine (5.2-16.6 μm), with rarely modes at 50-61.3 μm and >65 μm – Primarily poorly, with rarely very poorly sorted sediments – pfs to very pfs and ns GSDS – Primarily mesokurtic and rarely platykurtic	– Primarily pale brown, with occasionally light olive gray, and rarely light gray and light yellowish brown	– HL at 39.8-45.58 m – RM at 42.3 m	– Low MS (<2) – Primarily low (< 2), with rarely moderate FDMS (2-4.6)	– Leuc (4) – Limn (996) – Ilyo (130) – H-sal (92) – C-lac (51)	Mixture of fluvio-aeolian and Lacustro-aeolian facies
3	30.4-39.3	– Primarily medium silt with less abundant coarse silt, and rarely very coarse silt, and fine to very fine sand	– Primarily unimodal, with occasionally bimodal and two beds of trimodal GSDS at the top – Main mode is fine (6.1-17.6 μm), with rare modes at >65 μm and 54.6-61.9 μm – Primarily poorly, with rarely very poorly sorted sediments – Primarily pfs and ns GSDS with rarely strongly ncs GSDS – Primarily mesokurtic with occasionally platykurtic and leptokurtic sediments and rarely very leptokurtic	– Primarily light olive gray, light yellowish brown pale brown, and rarely light gray	– HL at 31.4-33.8 m, and 35.7 m – XB at 36 m – RM at 31.2 m and 38.8 m	– Primarily low MS (<2) and rarely moderate (2-4.5) – Primarily low (< 2), with occasionally moderate (2-11) and rarely high FDMS (> 16)	– Leuc (1) – Limn (231) – Ilyo (328) – H-sal (17) – Cand (1)	Fluvio-aeolian facies
2	15.5-30.4	– Primarily medium silt, with occasionally coarse silt and rarely fine, very coarse silt, and very fine sand	– Primarily unimodal, with occasionally bimodal and one bed of trimodal GSDS at 16.2 m – Main mode is fine (6.7-17.4 μm), with rare modes at >65 μm – Primarily poorly, with one bed of very poorly sorted sediments at 29.6 – - Primarily pfs and ns GSDS with rarely ncs and strongly pfs GSDS	– Primarily light olive gray, very pale to pale brown, with rarely yellow, light gray, light reddish brown	– HL at 17.3-19.2 m, and 22.5-24.6 m	– Low MS (<2) – Primarily low (< 2), with occasionally moderate (2-7.9) and rarely high FDMS (> 16)	– Leuc (38) – Limn (596) – Ilyo (554) – H-sal (162) – Cand (47)	

			– Primarily mesokurtic and occasionally platykurtic sediments and rarely leptokurtic and very leptokurtic					
1	0.0-15.5	– Primarily medium-coarse silt, with occasionally fine and very coarse silt and rarely very fine sand	– Primarily unimodal, with occasionally bimodal and rarely trimodal GSDS – Main mode is fine (5.5-20.4 µm), with occasional coarse mode (44-58.5 µm) and rare modes at >65 µm – Primarily poorly, with occasionally very poorly sorted sediments – Occasional occurrences of pfs to strongly pfs and ns GSDS – Primarily mesokurtic and less abundant leptokurtic and platykurtic sediments with rarely very leptokurtic	– Primarily light olive gray, very pale to pale brown, light yellowish brown, with rarely grayish brown, light gray, light brownish gray, and yellow	– HL at 0-2.3 m, 5.8-6.7 m, and 9-12 m. – XB at 3.5 m	– Low MS (<2) – Primarily low (< 2), with occasionally moderate (2-13) and rarely high FDMS (> 14)	– Leuc (296) – Limn (341) – Ilyo (431) – H-sal (162) – C-lac (9) – Cand (3)	Mixture of Fluvio-aeolian and Lacustro-aeolian facies

[a] The sediments are otherwise homogeneous.

MS Magnetic susceptibility (χ_{LF}), **FDMS** frequency-dependent magnetic susceptibility (χ_{FD}), **GSDS** grain-size distribution, **Sz** sedimentological zones, **HB** horizontal bedding, **RB** ripple bedding, **XB** cross bedding, **RL** ripple lamination, **HL** horizontal lamination, **RM** ripple marks, **FT** filling troughs, **Leuc** *Leucocythere* sp., **Limn** *Limnocythere* sp., **Ilyo** *Ilyocypris* sp., **H-sal** *Heterocypris salina*, **Cand** Juv. Candoninae, **C-lac** *Cytherissa lacustris*, **Prio** *Prionocypris* sp.

Manuscript II

3 The East Asian monsoon variability in the Nihewan Basin, northern China, during the Early Pleistocene: a grain size end-member modelling analysis

3.1 Abstract

The Pleistocene sediments of the Nihewan Basin in northern China preserve a detailed terrestrial sediment archive for reconstructing the palaeoenvironment and palaeoclimate changes during early times of hominin occupation in E Asia, following the earliest locations outside of Africa. In this study, we investigate the composite 86.2-m long NH-T section of Dachangliang which was formed with an astronomically tuned age between ca. 1.66 and 0.78 Ma. Parameterized grain size end-member modelling analysis is applied for the first time in the Nihewan Basin to unravel the characteristics of sediment sources, transportation dynamics, and climatic signals in the region. The grain-size distributions of the NH-T sediment samples are attributed to a mixture of four distinct end members (EMs 1-4). EM 1 represents a global atmospheric fine silt component (mode at 7.9 µm) which probably resulted from high-altitude westerly transport from distal sources. EM 2, a medium silt component (mode at 27.6 µm) was probably transported by the low-level westerly winds during the spring from a relatively proximal source in comparison to EM 1. EM 3, a coarse silt component (mode at 59.9 µm), represents short distance suspended materials that were blown out by N or NW winds of the East Asian winter monsoon (EAWM). EM 4 is a fine sand component (mode at 221.1 µm), probably representing fluvial deposits carried by overland flow. Therefore, the temporal fluctuations in the abundances of EMs 1-3 are used to infer the history of the East Asian summer monsoon (EASM) (EM 1), of dust-storm outbreaks during springtime (EM 2), and of the EAWM (EM 3). The NH-T climate record shows an overall increase in EM 3 peaks, accompanied by a decrease in EM 1 minima from ca. 1.45 to 0.82 Ma, indicating a long-term aridification and cooling trend in the Nihewan Basin. At ca. 1.20 Ma, the EM patterns transition from short-frequency to longer fluctuations, apparently coinciding with the onset of the Mid-Pleistocene transition (MPT). Periods of stronger EASM with more frequently warm and wet conditions probably occurred in the basin between ca. 1.66-1.62, 1.52-1.20 and after 0.82 Ma. Intensified EAWM conditions probably prevailed in the basin during the intervening periods from ca. 1.62-1.52 and 1.20-0.82 Ma. The inferred warmer and wetter conditions likely supported hominin activities in the Nihewan Basin, in contrast to mostly colder and drier conditions. The relatively consistent patterns observed between the variations of a median grain-size stack of the Chinese Loess Plateau (CLP MD) and EM 3, and of the magnetic susceptibility stack of the CLP (CLP MS) and EM 1, indicate the climatic sensitivity of these EMs in response to the long-term glacial/interglacial oscillations previously inferred from the CLP. However, significant differences in the CLP MD and CLP MS on the one hand side and in the trends of the EMs 3 and 1 on the other suggest that regional climate conditions varied between the

CLP and the Nihewan Basin. Further research is required to explore such regional climate differences and their possibly underlying factors in the Early Pleistocene.

3.2 Introduction

Wind-blown dust deposits are widely distributed in China and are one of the most important terrestrial archives to study the East Asian monsoon variability over the geological past (Liu, 1985). Studies of Quaternary loess accumulation in N China suggest that the loess-like deposits found at the edge of the Gobi Desert, as well as those on the Chinese Loess Plateau (CLP) and the N China Plain, are part of a unified Asian aeolian depositional system (Sun et al., 2018; Zan et al., 2018; Jia et al., 2019; Li et al., 2020).The Nihewan Basin, located in northern China, is significant in Quaternary geological research in China due to its relatively continuous sedimentation. It also preserves fossil remains of the Pleistocene megafauna and lithic artefacts (Barbour, 1924; Teilhard de Chardin and Piveteau, 1930; Deng et al., 2008; Yang et al., 2019). Despite the importance of the basin and the number of conducted studies, there is possibly the misconception that the thick sedimentary infill of the Nihewan Basin is exclusively composed of lacustrine and fluvial sediments (for example, Barbour, 1924; Li et al., 2000; Min et al., 2002, Hu et al., 2005; Li et al., 2008; Chen et al., 2015). Nevertheless, Moghazi et al. (2024a) interpreted the exposed Early Pleistocene sediments at the location Dachangliang in the Nihewan Basin as mainly fluvially reworked, originally aeolian deposits which accumulated under changing hydrodynamic conditions transitioning between wetland, alluvial plain and lacustrine settings. Considering these new insights together with the basin’s location at the eastern margin of China's loess distribution and its location ca. 400 km SW of the Chifeng area in Inner Mongolia where early Pleistocene loess deposits have been found in river valleys and hills (Zeng et al., 2011, 2016), the Nihewan Basin has possibly potential to provide a valuable long-term record of the past atmospheric dustiness in relation to the variations of the East Asian monsoon, possibly comparable with the Pleistocene monsoon evolution that was previously inferred from the Chinese loess deposits. Notably, late Pleistocene or Holocene loess deposits are widespread in the basin (Deng et al., 2008). However, the basin has no reported sediment record of original early Pleistocene loess deposits for comparison so far.

Terrigenous deposits typically represent a mixture of sediments that are often transported by multiple processes and/or from multiple sources. Thus, they are characterized by bi- or polymodal grain-size distributions (GSDs) (McLaren and Bowles, 1985; Rea and Hovan, 1995; Prins and Weltje, 1999; Sun et al., 2002, 2004; Xiao et al., 2009, 2015; Vandenberghe, 2013) which are challenging to interpret in terms of past climate or environmental conditions (Meyer et al., 2013). With the aid of high-resolution grain-size data generated by laser grain-size analysers, several mathematical methods were introduced to define and unmix the various grain-size components of the bulk sediment with GSDs reflecting specific provenances or/and transport dynamics. These methods follow three different approaches: (1) end-member modeling analysis (EMMA) (Weltje, 1997; Dietze et al., 2012; Paterson and Heslop, 2015), (2) the decomposition of GSDs into Weibull distributions (Sun et al., 2002, 2004), and (3) the log-normal distribution function fitting method (Xiao et al., 2009; Gammon et al., 2017). These analyses have greatly extended the application of grain-size analysis in the differentiation and evolution of short- and long-distance dust transport (Sun et al., 2002; Qin et al., 2005; Prins et al., 2007), and contributions of fluvial (Kranck et al., 1996; Påsse, 1997), and aeolian inputs (Sun et al., 2002; Qin et al., 2005). Understanding whether Nihewan deposits evolved by aeolian or aqueous transport media or both remains ambiguous, and no reliable, quantitative method has yet been applied to address this issue.

Accordingly, this study investigates the composite 86.2-m long NH-T section of Dachangliang formed between ca. 1.7 and 0.9 Ma (Moghazi et al., 2024a), using EMMA for the first time in the Nihewan Basin to unravel the characteristics of sediment sources, transportation dynamics, and their links with the climatic conditions in the region during the Early Pleistocene.

3.3 Study area

Geographically, the Nihewan Basin is situated at a northern latitude of 40°. It is a semi-arid region within the transition zone between the N China Plain and the Inner Mongolian Plateau, the eastern Mu Us Desert and adjacent to the northeastern CLP (Fig. 19.3b). The CLP lies up-wind of the Nihewan Basin with the prevailing winds in the region usually propagating from high-altitude NW into SE downwind regions.

The basin is bounded by the Xiong'er Mountain to the N, the Liuleng Mountains to the S, the Fenghuang Mountains to the E and the Guancen Mountain to the SW, with the Sanggan River and a major tributary, the Huliu River, flowing through the basin (Fig. 19.3a).

Geologically, the onset of basin deposition resulted from tectonic down-faulting during the early Pliocene prior to ca. 3.6 Ma (Liu et al., 2018), synchronous with the onset of thick loess deposition on the CLP (Ding et al., 2002). The Youfang dip-slip fault may have played a significant role in the formation of the Nihewan paleolake (Deng et al., 2008). Barbour et al. (1926) recognized the deposition of the aeolian red clay formation in the Nihewan Basin during the Early Pliocene, similar to the so-called “Hipparion red clay” that is exposed on the CLP (Teilhard de Chardin and Young, 1930). This complex depositional history of sedimentation processes resulted in the formation of a ca. 700-m thick sequence of Pliocene to Holocene lacustrine, fluvial, and windblown deposits (Zhou et al., 1991; Zhu et al., 2007; Deng et al., 2008).

Theses sediments were collectively named Nihewan Beds (Barbour, 1924) or the Nihewan Formation (Deng et al., 2008; Ao et al., 2013a). The sedimentary sequence is assumed to have recorded the climatic and tectono-sedimentary processes of the Nihewan Basin during the Plio-Pleistocene (Deng et al., 2008). Despite characteristic fluctuations in the sedimentary facies and sediment-accumulation rates, the deposits of the basin represent a long continuous stratigraphic record (Wang et al., 2004).

Palaeontologically, the Nihewan sequence contains a rich source of Pleistocene mammalian faunas known as the Nihewan Fauna sensu lato, including the Xiashagou Fauna (the Nihewan Fauna sensu stricto) (Deng et al., 2019; Teilhard de Chardin and Piveteau, 1930).

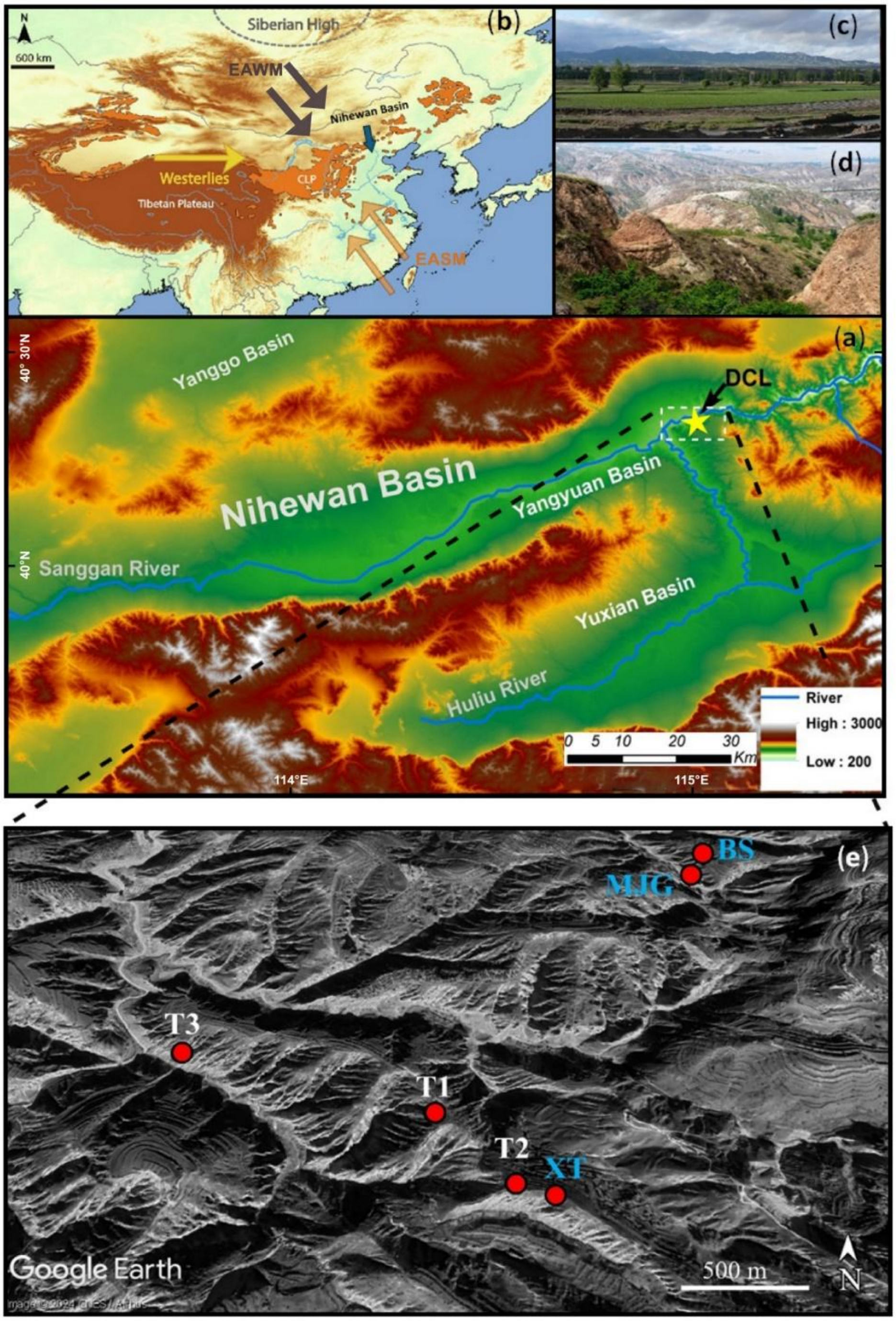

Figure 19.3 *(a) Location of the study area Dachangliang (DCL) marked by yellow star in the Nihewan Basin. (b) The general position of the Nihewan Basin in Asia, highlighting the main atmospheric circulation patterns (modified after Guo et al., 2024). CLP-Chinese Loess Plateau; EASM-East Asian Summer Monsoon; EAWM-East Asian Winter Monsoon. (c), (d) Present-day environment and terrain of the Nihewan Basin, including the modern Sanggan River. (e) Locations of the T1, T2 and T3 sediment sections (white labels) and the neighbouring Paleolithic sites (Majuangou (MJG), Banshan (BS) and Xiantai (XT); blue labels*

Archaeologically, the basin is recognized as an important centre of early human occupation in northern China (Yang et al., 2020). The hominin occupation in the basin dates back to ca. 1.66 Ma (Zhu et al., 2004) whereas it began no later than 2.43 Ma in Asia (Shen et al., 2020). Along the eastern margin of the basin, there is a sequence of well-preserved Palaeolithic sites from all stages of the Pleistocene, particularly of the Early Pleistocene (Deng et al., 2019; Yang et al., 2020).

Climatically, the basin experiences the East Asian monsoon climate characterized by cold and dry winters, while summers are relatively warm and humid as the rainfall during summer amounts to 80% of the total annual precipitation (Chen, 1988). The mean January temperature is ca. -16°C with a mean July temperature of ca. 29°C (Yangyuan County Weather Station, 1980-2019; data source: China Meteorological Data Network, http://data.cma.cn). The annual regional precipitation is 359-418 mm (Yuan et al., 2011; Ao et al., 2012). The vegetation in the region varies from temperate deciduous shrubland in the mountainous regions to temperate steppe in the interior of the basin (Mu et al., 2015).

3.4 Materials and Methods

3.4.1 Previously conducted sediment sampling and grain-size analysis

The sampling site consists of three sediment sections which were newly exposed on the SW slope of the Dachangliang ridge at 40.2199 °N and 114.6589 °E (T1), 40.2190°N and 114.6598°E (T2) and 40.2212 °N and 114.6549 °E (T3), respectively (Fig. 19.3e). The tops of the T1, T2 and T3 sections are located at an elevation of 894.04, 906.31 and 861.76 m, respectively (Moghazi et al., 2024a). During the summers of 2018 and 2019, the lithology of the exposed sediments was assessed, including the grain size, colors, sedimentary bedding structures and pedogenic features. Macroscopic fossils, mainly gastropod shells, were identified. A total of 414 sediment samples were collected at intervals of 27 cm on average from the three sections T1, T2, and T3, representing a combined thickness of 112.5 m (45.8 m at T1, 26 m at T2, and 50.5 m at T3). The recorded ostracods (micro-crustaceans) of laterally apparently consistent white marl beds were used to stratigraphically correlate these sections. The resulting composite section NH-T with 86.2 m thickness (Moghazi et al., 2024a) was further correlated with the three proximal artefact-bearing sections Majuangou, Banshan and Xiantai which have published magnetostratigraphic data (Zhu et al., 2004; Ao et al., 2010).

The grain-size analysis was conducted at the Key Laboratory of Western China’s Environmental Systems, Lanzhou University, involving detailed sample preparation steps and precise measurement with the Mastersizer 2000 laser analyzer (Moghazi et al., 2024a). The grain-size classification followed the Wentworth scale (Wentworth, 1922), and grain-size parameters were computed using GRADISTAT v.8 (Blott and Pye, 2001), based on Folk and Ward's reference formulas (Folk and Ward, 1957).

3.4.2 End-member modeling analysis (EMMA)

The GSDs of 302 samples, representing the 86.2-m thick NH-T composite section were parameterized and decomposed using AnalySize v.1.2.0, a MATLAB-based graphic user interface (GUI) package (https://github.com/greigpaterson/AnalySize) (Paterson and

Heslop, 2015), employing the Gen.Weibull Distribution function (Wu et al., 2020). This algorithm aims to establish a physical mixing model that transforms the original distribution into a limited number of non-negative and unimodal end members (EMs) that can be interpreted individually (Meyer et al., 2020; Eltijani et al., 2022). The optimal number of EMs representing the GSDs was determined by evaluating the linear correlation (R^2) and the mean angular deviation (θ) between the number of EMs and the original GSDs. Relatively higher R^2, lower θ, and fewer EMs indicate a better statistical fit (Paterson and Heslop, 2015). For meaningful interpretation of the observed sedimentological variations within the investigated composite NH-T section, sedimentary zones were determined based on the stratigraphic distribution of the relative EM abundances, using the change point detection option in the software PAST.

3.4.3 Correlation analysis

The Pearson correlation between each grain-size EM mean particle size (MZ), magnetic susceptibility (MS), and frequency-dependent magnetic susceptibility (χ_{FD}) was assessed using the statistical coding program R, version 4.1.3 (http://www.rstudio.com/). The MZ, MS, and χ_{FD} values were extracted from the original datasets provided by Moghazi et al. (2024a). This correlation will allow us to better analyze the differences and connections between transport mechanisms behind the EMs (Kong et al., 2021).

3.4.4 Cluster analysis

A Stratigraphically Constrained Incremental Sum of Squares (CONISS; Grimm, 1987) hierarchical cluster analysis, conducted in RStudio with the rioja package (Juggins, 2022) was used to identify potentially climate-linked stratigraphic zones based on the variation trends in the EMs 1 and 3.

3.4.5 Cyclostratigraphy and orbital tuning

Moghazi et al. (2024a) argued that the sediment-accumulation timeframe at Dachangliang is between ca. 1.7 and 0.9 Ma, constrained by geomagnetic reversals from the lower boundary of the Oldovai subchron and the Brunhes-Matuyama boundary (Deng et al., 2006a, 2006b). To refine this chronological frame and develop a more reliable age model for the NH-T sediment section, we carried out a cyclostratigraphic analysis based on the stratigraphic variations of EM 3. This was performed with the WaverideR (Arts, 2023) and Astrochron (Meyers, 2014) R packages. We first performed a 2π Multi-Taper Method (MTM) (Thomson, 1982) of spectral analysis on the EM 3, identifying significant periodic components, particularly the obliquity cycles (~41 ka) (Supplementary Figure S 1). A Taner filter (Taner, 2000) was then applied to isolate this obliquity signal (Supplementary Figure S 2). The resulting time series was then astronomically anchored to La2004 astronomical solution (Laskar et al., 2004). The astronomical calibration method and the step-by-step times-series analysis of the EM 3 record are detailed in the supplementary material. The anchored ages derived from the EM 3 record were then applied to the CLP MD stack over the last 1.6 Ma using data from Ao et al. (2023) and for 1.7-1.6 Ma interval using data from Han et al. (2020) for comparison with our astronomically tuned NH-T section.

3.5 Results

Four distinct EMs were determined from the decomposing approach of GSDs of the NH-T sediment samples (Fig. 21.3a). The R^2 statistics show that the four-EM model can explain on average 98% of the total variance in the dataset and that applying more EMs does not improve the result significantly (Fig. 20.3). The GSD of EMs reveals differently pronounced modeled mean grain sizes in respect to their peak values at 7.9 µm, 27.6 µm, 59.9 µm, and 221.1 µm, respectively (Table 1.3). EM 1 is characterized by a wide peak area with a relatively lower frequency, while EM 3 shows the narrowest peak area with the highest frequency (Fig. 21.3a).

EM 1 represents fine silt. It is mainly composed of silt-sized materials (77.6 %) with significant contribution of clay-sized materials (21.8 %) and a minimal presence of sand particles (0.6 %). EM 2 represents medium silt. The content of silt-sized materials dominates in EM 2 (95.2 %). EM 2 has a relatively higher contribution from sand particles representing (4.8 %). EM 3 represents coarse silt. The EM 3 content of silt and sand particles is 53.6 % and 46.4 %, respectively. EM 4 represents fine sand and is dominantly composed of sand 95.6 %, accompanied by 4.4% of silt particles.

The mean contributions of EMs 1-4 are 51.4, 20.2, 24.0 and 4.4%, respectively. The relative abundance of all EMs fluctuates within the range of complete absence 0 to 100%, with the exception of EM 2, which attains its maximum value at 66%.

The sorting (σ_{ϕ}) values are 1.28 ϕ in EM 1, 0.72 ϕ in EM 2, 0.64 ϕ in EM 3 and 0.91 ϕ in EM 4. The skewness (Sk_{ϕ}) values of EMs 1-4 are 0.03, 0.02, 0.01 and 0.16, respectively. The EMs have kurtosis (K_{ϕ}) values of 0.98 in EM1, 0.97 in EM 2, EM 3 and 1.01 in EM 4 (Table 1.3).

Table 1.3 *The statistical grain-size parameters of the four EMs of the NH-T sediment samples.*

EMs	**Mean (MZ)**	**Sorting (σ_{ϕ})**	**Skewness (Sk_{ϕ})**	**Kurtosis (K_{ϕ})**	**Clay%**	**Silt%**	**Sand%**
EM 1	7.9	1.28	0.03	0.98	21.8	77.6	0.6
EM 2	27.6	0.72	0.02	0.97	0.0	95.2	4.8
EM 3	59.9	0.64	0.01	0.97	0.0	53.6	46.4
EM 4	221.1	O.91	0.16	1.01	0.0	4.4	95.6

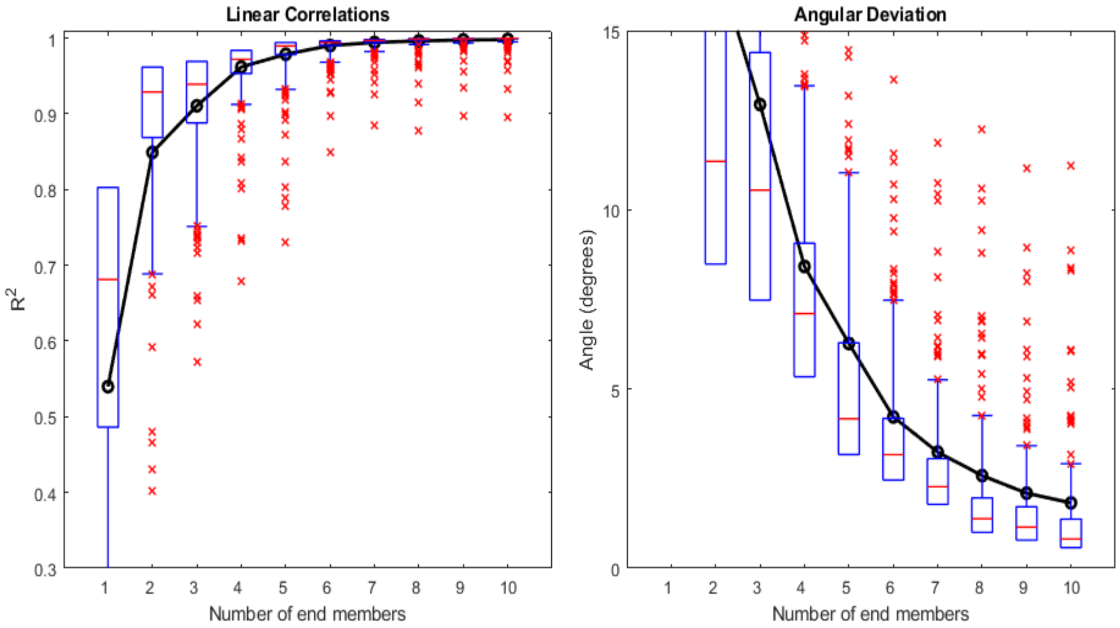

Figure 20.3 *Variation in the linear correlation (R2) and mean angular deviation (θ) as a function of the number of EMs and the original grain-size data set of the NH-T sediment samples*

3.6 Discussion

3.6.1 Sedimentation dynamics inferred from EMs

The grain-size composition of the sediments from the NH-T composite section is mostly silt to sandy silt (Fig. 24.3). The multimodal GSDs of these sediments are decomposed into four EMs 1-4, each one representing a distinct unimodal GSD with potential links to specific sediment source or/and transport mechanism. According to Dietze and Dietze (2019), sediment from various sources can be transported and deposited by a multitude of sedimentological processes. These processes are closely associated with climate conditions, vegetation patterns, geological features, and geomorphological dynamics.

Building upon the context of six depositional cycles suggested by Moghazi et al. (2024a) and based on the stratigraphic EM variations, fifteen associated subcycles have been further identified (Fig. 22.3, Supplementary Table S 1), possibly related to seasonal changes or episodic events, primarily driven by climatic forces with a secondary influence from local

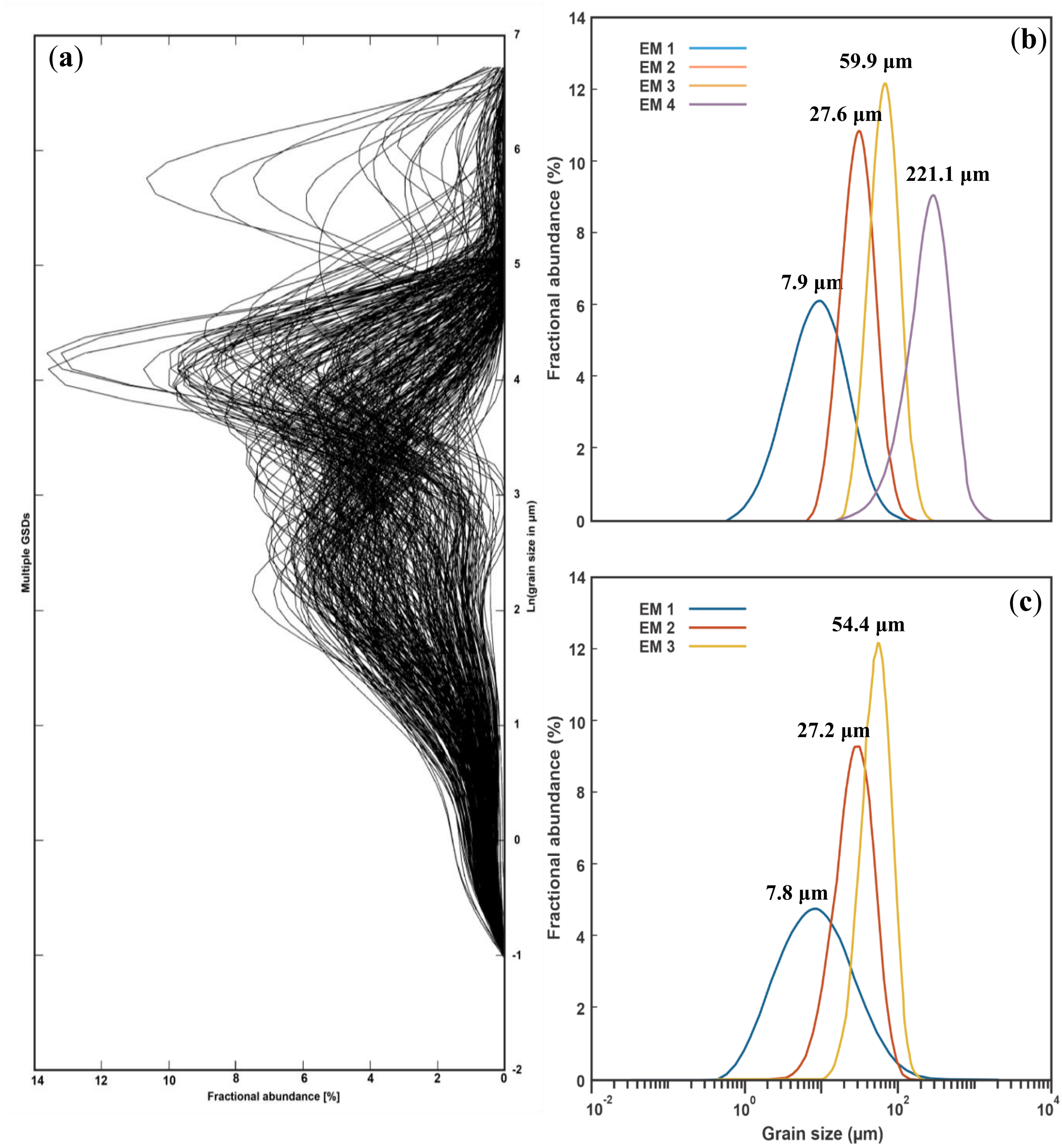

Figure 21.3 *(a) Original grain-size frequency-distribution curves for NH-T sediment samples. (b) Parametric end-member frequency-distribution curves and modeled mean grain sizes based on the four-end-member model for NH-T sediments, in comparison with the three-end-member model for Harbin loess sediments from NE China, redrawn from Wu et al. (2023)*

tectonics and extreme weather conditions. This model with four EMs, thus, provides a valuable framework for reconstructing the palaeomonsoonal climate dynamics, variety of sediment sources, and multiple transport mechanisms during the Early Pleistocene.

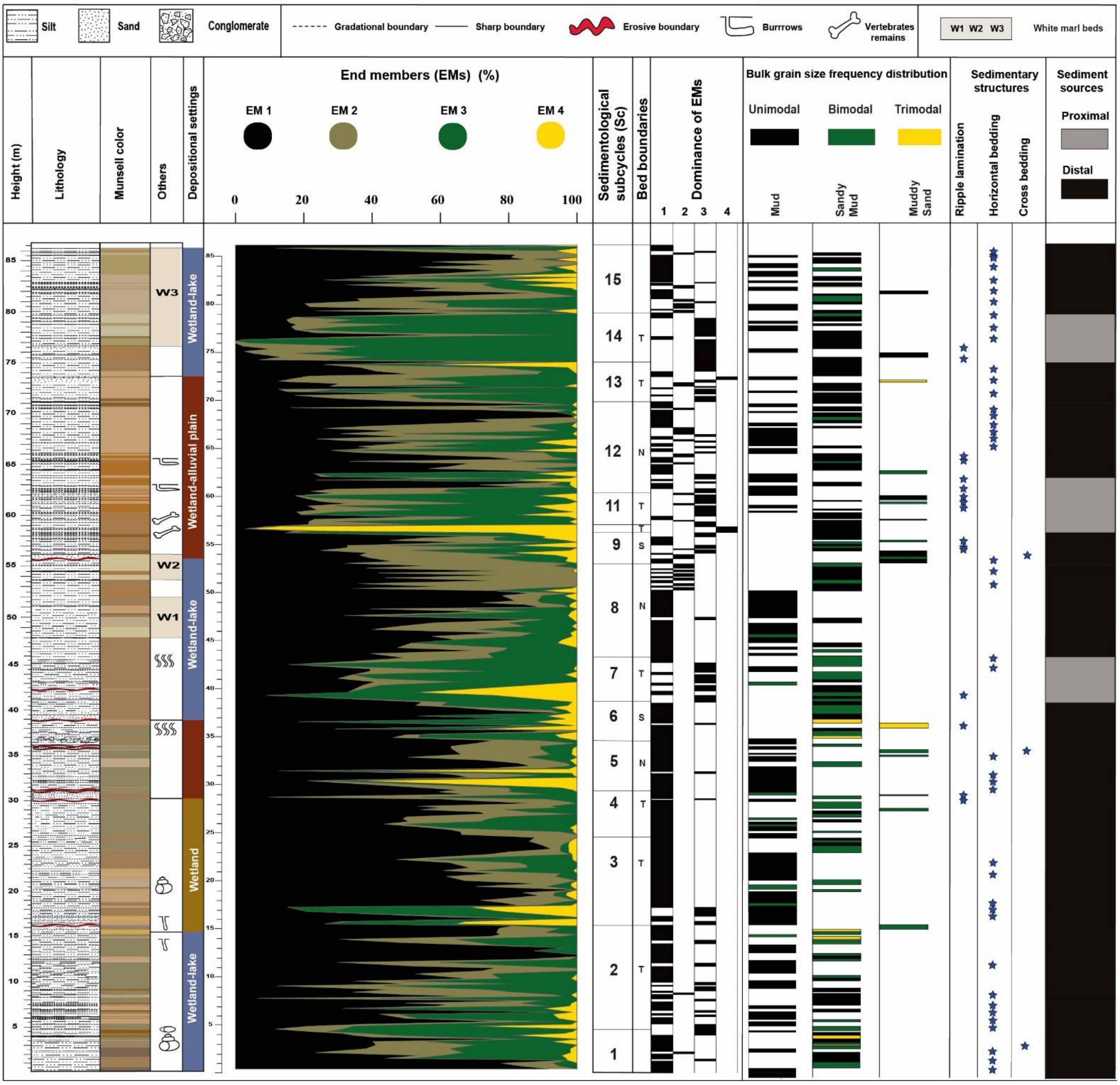

__Figure 22.3__ Stratigraphy of the sediment section NH-T, encompassing lithology, colour, positions of white marker layers (W1-W3), depositional settings (after Moghazi et al., 2024a), relative contribution of four EMs, sedimentological subcycles, bed boundaries, dominance of EMs, types of GSDs, sedimentary structures and inferred sediment sources at right

Characteristics of EM 1

The mean grain size of EM 1 is fine silt at 7.9 μm. EM 1 particles are lithologically composed of a higher portion of the silt fraction (77.6 %) with significant contribution of the clay-sized fraction (21.8 %) and a negligible content of the sand fraction (0.6 %). EM 1 shows the poorest sorting among the four EMs with near symmetrical and mesokurtic distribution. Moreover, the EM 1 peak is characterized by a relatively low frequency with the widest grain-size range than the other EMs (Fig. 21.3a). Thus, the deposition of EM 1 was possibly under low-energy conditions from suspension.

Table 2.3 *Correlation coefficients (r) between EMs, MZ, MS and* χ_{FD} *of the NH-T sediment samples.*

	EM 1	EM 2	EM 3	EM 4	MZ	MS	χ_{FD}
EM 1	1						
EM 2	-0.2	1					
EM 3	-0.8	-0.3	1				
EM 4	-0.3	-0.3	0.0	1			
MZ	-0.5	-0.2	0.3	0.6	1		
MS	-0.1	-0.3	0.1	0.3	0.5	1	
χ_{FD}	0.1	0.0	-0.1	-0.1	-0.1	-0.1	1

Loess is a clastic sediment, predominantly composed of silt-sized particles (Pye, 1995). In the loess deposits of the CLP, the fine-grained silt mode (5-15 μm) represents the aeolian background dust that is typically transported in high-suspension westerly winds over long distances before settling (Sun et al., 2002; Prins et al., 2007). Liang et al. (2019) reported a similar fine silt mode (5-10 μm) in one of the sediment components deposited in temporary depressions of modern alluvial plains in the Yardang corridor, NW China.

EM 1 represents the dominant EM that is present in 98.7 % of all samples throughout the NH-T section with an average contribution up to 51.4 %. Prins et al. (2007) interpreted a comparable fine-grained loess component EM 3 (modal size: 11 μm), to our EM 1, as atmospheric background dust, primarily deposited during the autumn and winter, and partially supplied by the westerly winds rather than dust-storms of the winter monsoon.

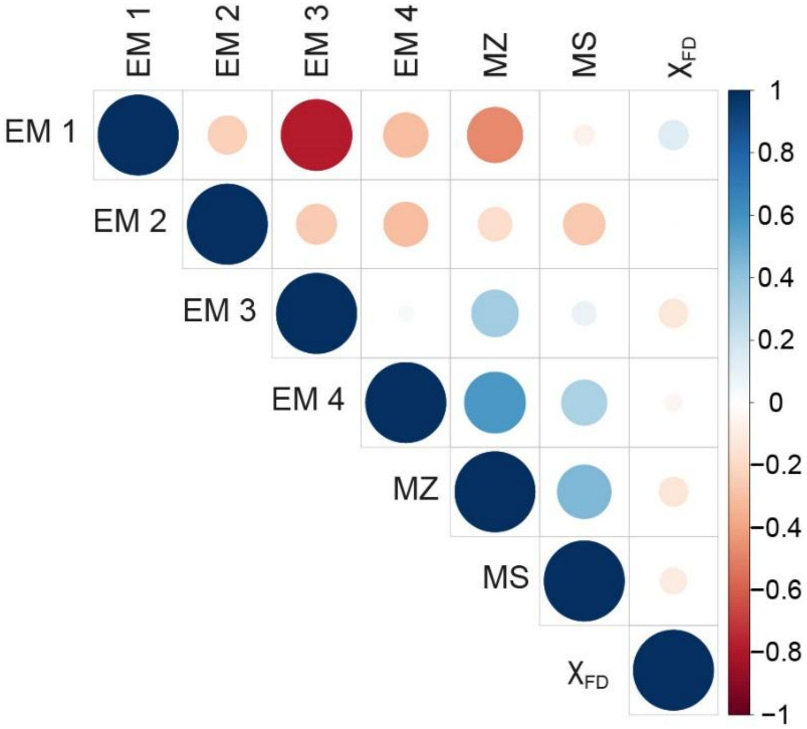

Figure 23.3 *Pearson correlation coefficients between each EM with MZ, MS and* χ_{FD} *of the NH-T sediment samples*

The Nihewan Basin's topography likely enhanced the deposition of fine-grained dust on the downwind side of the mountains, while coarser dust fractions were likely intercepted by topographic barriers (Pye, 1995). Thus, we infer that the EM 1 was probably transported by a high-latitude strong westerlies wind system over large distances from Central Asia. Field observations of the NH-T sediment colour indicate that the sediments are predominantly very pale brown (10YR 7/3-4), yellowish brown (10YR 5/4-8), light olive gray (5Y 6/2), and brownish yellow (10YR 6/8). The pale brown, yellowish brown and brownish yellow colours might be due to subaerial conditions while the light olive gray colour probably resulted from the pedogenic modification of the sediment including organic matter enrichment in soils that formed under forest steppe or steppe vegetation (Lehmkuhl et al., 2016).

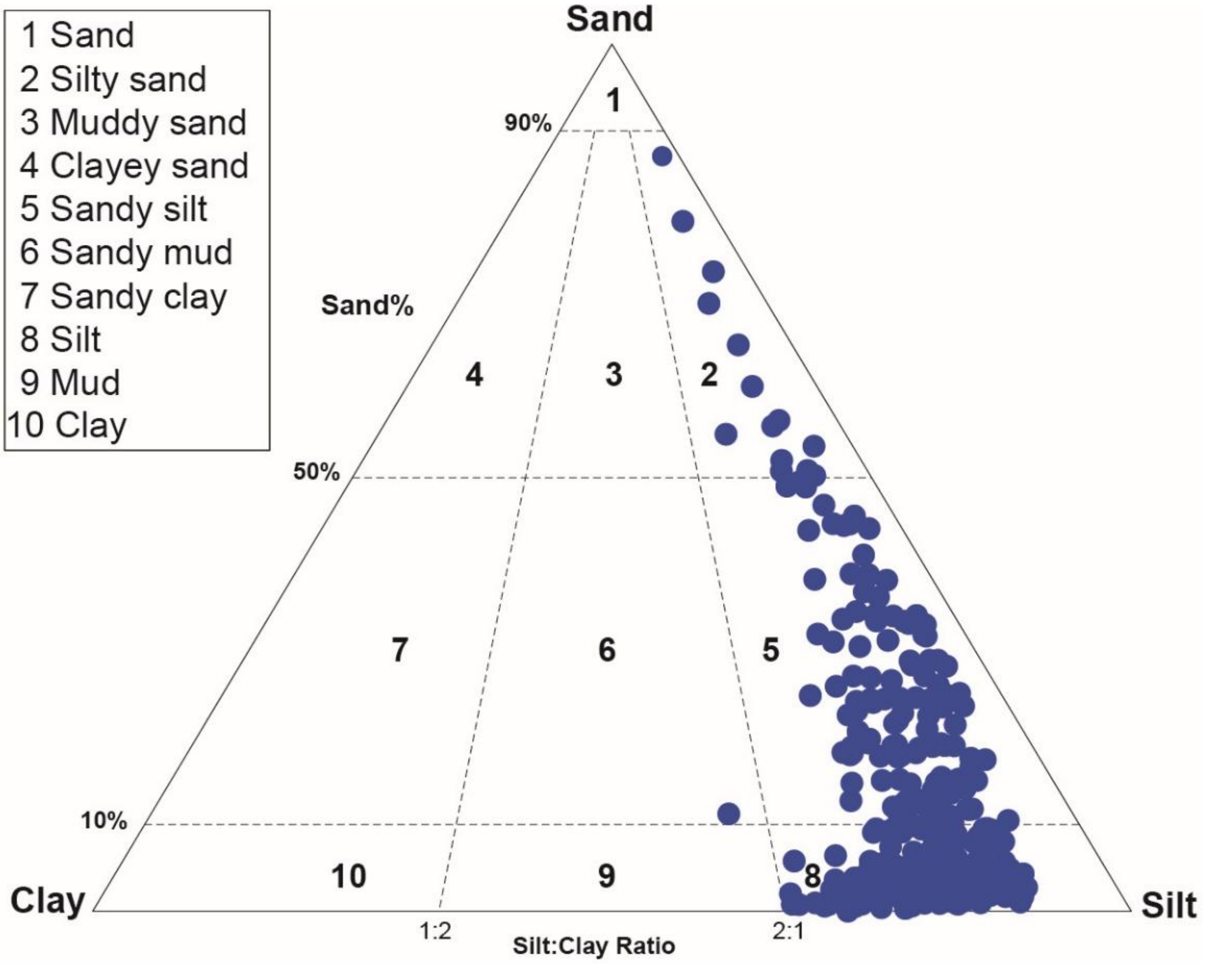

Figure 24.3 *Ternary plot of the sand-silt-clay abundances in the NH-T section (after Folk, 1954)*

Moghazi et al. (2024a) also reported the presence of carbonate nodules in the sediments at the lower part of NH-T section (0.0-15.5 m) which additionally shows a discernible level of pedogenesis. Furthermore, EM 1 is uniquely characterized by a weak positive correlation with χ_{FD} in contrast to the other EMs, indicating soil formation processes (Lu et al., 2008) that affected part of EM 1 sediments after deposition (Table 2.3, Fig. 23.3). Moreover, high EM 1 abundances are observed in the three distinct white marl layers (W1-W3) in NH-T section which were inferred to have been deposited in deeper phases of shallow lacustrine settings supported by the ostracod assemblage (Fig. 27.3; Moghazi et al., 2024a). Otherwise, final sediment accumulation probably occurred mostly in a wetland setting on an alluvial plain. We conclude that EM 1 was primarily transported as background dust by high-altitude westerly winds, and that accumulated sediments were partly affected by weathering and pedogenic processes. High proportions of EM 1 in the sediments represent periods when potential contributions of more locally sourced, coarser aeolian sediments, transported as a result of the EAWM or during strong dust storms, were reduced. Such conditions probably existed during warmer and wetter periods which supported a denser vegetation cover in the region, representing interglacial periods. Thus, EM 1 can be used as an indirect proxy for the strength of the EASM, during intervals when the EAWM and spring dust storms were relatively inactive.

Characteristics of EM 2

EM 2 with a mean grain size of 27.6 μm mainly represents medium silt. EM 2 is dominantly composed of the silt fraction (95.2 %) with a relatively higher proportion of the sand fraction (4.8 %) compared to EM 1. It is characterized by moderate sorting, and near symmetrical and mesokurtic distribution. The relatively higher EM 2 peak with a narrower grain-size range compared to EM 1 (Fig. 21.3a), suggests that the EM 2 deposition was probably under moderate energy conditions.

The mean-grain size of EM 2 falls within the silt fraction range (modal size: 16-44 μm) in the Quaternary Chinese loess (Vandenberghe et al., 1997) and resembles the silt particles (modal size: 25 μm) in the Red Clay (Vandenberghe et al., 2004). EM 2 is also comparable to the sediment type 1.b.3 in Vandenberghe (2013) which represents the commonly recognized medium-silty windblown dust as source of loess deposits. EM 2 possibly has a similar origin to the loess type deposited from near-surface to low-suspension clouds associated with the weakening Siberian High-Pressure Cell (Tsoar and Pye, 1987; Prins and Vriend 2007; Vandenberghe 2013).

Thus, we suggest that the low-level westerly winds were the driving force behind the deposition of EM 2 particles.

In the NH-T section, 87.4 % of all samples contain EM 2 with a significantly lower average contribution of 20.2 % than EM 1. The EM 2 with its relatively low sand content may resemble the suspension and saltation components of the aeolian materials transported in the spring dust-storm events in the Hulun Lake region, Inner Mongolia (Xu et al., 1989).

The EM 2 sediments are less well sorted which resulted in a lower kurtosis compared to the typical Chinese loess (Prins et al., 2007). However, the better sorting of EM 2 particles than EM 1 probably resulted from the fluvial reworking which subsequently flushed these particles into a wetland-lake setting. Additional evidence of reworking is the occasional presence of sedimentary structures in the NH-T section which include horizontal and ripple lamination and horizontal bedding (Fig. 25.3, Supplementary Table S1; Moghazi et al., 2024a).

The highest average abundance of EM 2 (24.2 %) is found in the wetland-lake interval (39.3-55.8 m) of NH-T section, while the wetland-alluvial interval (30.4-39.3 m) shows the lowest average abundance of EM 2 (12.0 %), indicating a difference in the depositional conditions with EM 1 (Table 3.3).

These observations of the changing sedimentary conditions behind the EMs 1-2 closely resemble the conditions of the floodplain facies c of reworked loess (Vandenberghe et al., 2021). Based on their inferences, this facies is indicative of calm, low energy flooding events, with fluvial and/or fluvio-aeolian sedimentation, resulting in stagnant pool formation with lacustro-aeolian sedimentation in oxbow lakes.

We conclude that the primary EM 2 was transported by prevailing low-level westerly winds (westerly jets during spring times) from a source that, while still distal, was more proximal than the source of EM 1. Subsequently, the EM 2 was reworked by overland flow before sediment eventually accumulated in a wetland-lake setting on an alluvial plain.

Characteristics of EM 3

The peak of EM 3 is centered around coarse silt at a mean grain size of 59.9 µm. EM 3 is dominated by silt fraction (53.6 %) and a relatively high content of the sand fraction (46.4 %). EM 3 is moderately well-sorted. It has the highest frequency peak and a narrower grain-size range than EMs 1-2, representing a significantly better sorting. This suggests a relatively higher energy setting of deposition or higher aeolian activity, probably indicating a closer source area. However, the skewness and kurtosis of the three EMs are relatively similar (Table 1.3). The silt fraction of EM 3 falls within the coarse dust subgroup 1.b.1 (51-60 µm) following the classification of Vandenberghe (2013). The coarse dust (>32 µm) is primarily carried in the air for short distances under strong winds and travels closer to the ground than the fine dust (Tsoar and Pye, 1987; Stuut et al., 2009). Prins et al. (2007) suggest that their coarse-grained loess component EM 1 (modal size: 55 µm) was produced from the episodic suspension fall-out of moderate-to-coarse dust, transported by surface-level monsoonal winds from proximal N to NW sources over the northern CLP. Prins et al. (2009) noted the presence of coarse silt components and very fine sand particles in the loess closely associated with the Yellow River floodplain. Accordingly, we suggest that our EM 3 particles were primarily transported from local sources by short-term suspension clouds of the winter monsoon forced by the Siberian High-Pressure Cell.

The notable presence of sand particles within EM 3 suggests the proximity to larger sand deposits, probably on an alluvial plain. This is supported by the high proportion of mica particles in the collected sediment samples, indicating eroded materials from the local bedrock. The EM 3 sediments have a lower kurtosis compared to the typical Chinese loess (Prins et al., 2007), further supporting mixing aeolian sediments with locally eroded alluvial materials. Accumulation of the EM 3 sediments probably occurred eventually in an alluvial plain setting.

EM 3 is the second dominant EM in the NH-T section after EM 1, present in 83.4% of all samples with an average contribution of 24.0 %. The highest average abundance of EM 3 (36.3%) occurs in the upper wetland-lake interval (74.0-86.2 m) of NH-T section, while the wetland interval (15.5-30.4 m) has the lowest (14.6%), showing an opposite pattern to EM 1 (Table 3.3).

In the Holocene Yaohecun loess-palaeosol section in E Guanzhong, Shaanxi Province, Wang et al. (2018) found that their fine silt EM 1 (modal size: 12.7 µm) has the highest abundance in the palaeosol interval S_0, while the loess interval L_0 shows the lowest abundance, an opposite pattern to their coarser EM 3 (modal size: 21.4 µm) (Wang et al., 2018). This observation is relatively comparable to the anti-correlation pattern between our EM 1 and EM 3. In a study on the Harbin loess in NE China, Wu et al. (2023) interpreted their dust component EM 3 (54.4 µm), resembling our EM 3 (Fig. 21.3b) as representative of the strength of EAWM intensity.

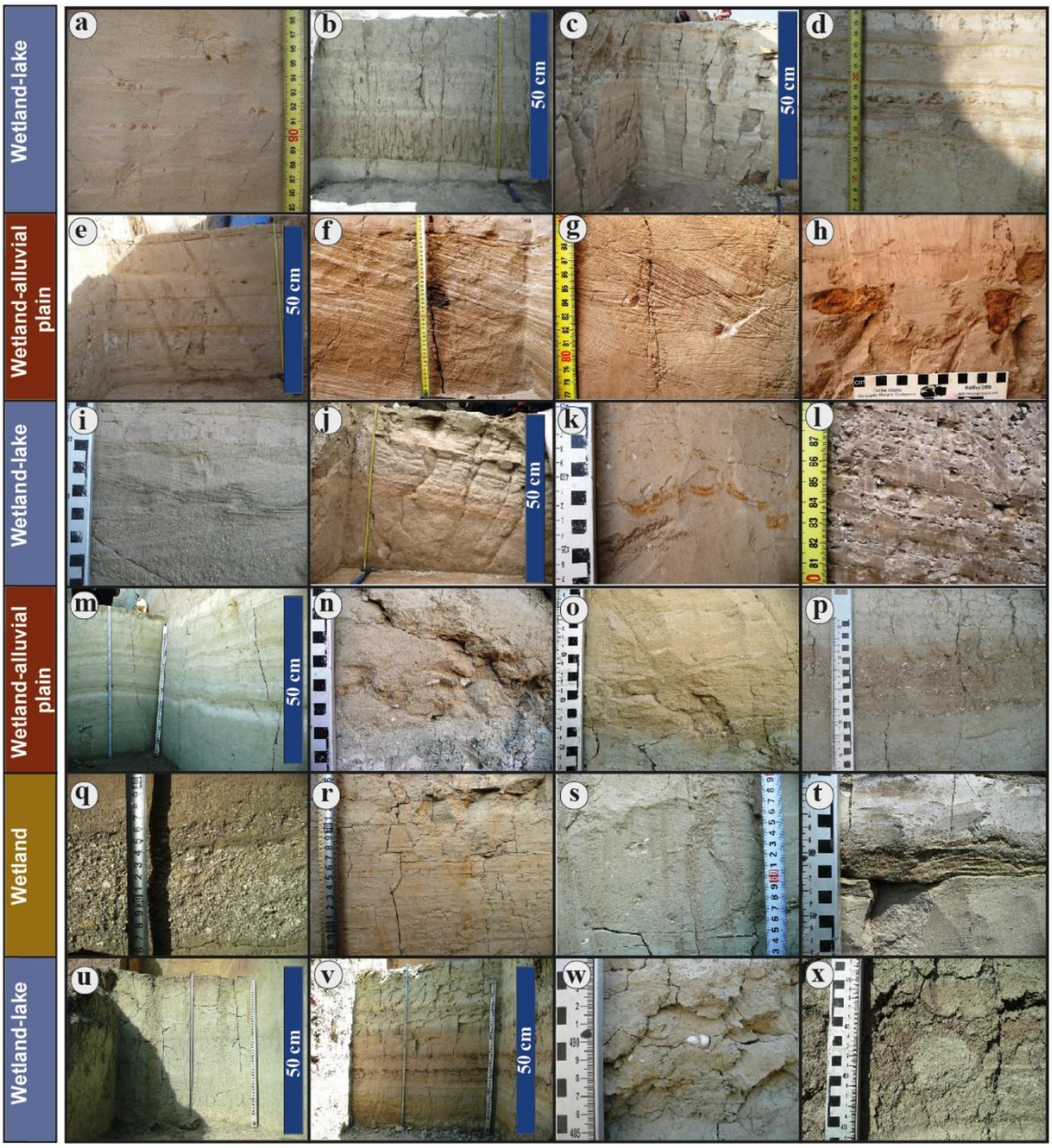

Figure 25.3 *Field observations of the sedimentary structures recognized in the NH-T sediments. (a) Ripple lamination with troughs, (b), (c), (d) and (e) Horizontal bedding ca. 1-cm thick, (f) Cross bedding, (g) Ripple lamination, (h) Massive (structureless), (i) Wave ripple lamination, (j) Horizontal bedding ca. 1-4 cm thick, (k) and (l) Massive, (m) Horizontal bedding ca. 2-8 cm thick, (n) Massive, (o) Cross bedding, (p) Massive, (q) Massive (event layer), (r) Horizontal bedding ca. 1-2 cm thick, (s), (t) and (u) Massive, (v) Horizontal bedding ca. 1-2 cm thick, (w) Massive with gastropod shells, (x) Massive with mud ball*

Xiao et al. (2013) observed that the eolian dust trapped in the ice of the central Daihai Lake, Inner Mongolia, predominantly shows a modal size of 50 µm, comparable to the modal size of our EM 3. They attributed the deposition of this coarser dust fraction to modern dust-storm events, which prevail in the region particularly during strong north-westerly winds (Chinese Academy of Sciences, 1984).

Thus, we conclude that the primary coarse dust materials of EM 3 were probably mainly transported from short-distance sources by N or NW winds of the EAWM, driven by the Siberian High-Pressure Cell. Such conditions probably dominated during the colder, glacial periods of the Early Pleistocene in the Nihewan Basin. EM 3 represents a proxy for the strength of the EAWM intensity.

Characteristics of EM 4

EM 4 has a peak at the largest grain size at 221.1 µm, mainly fine sand, representing the coarsest EM. EM 4 is dominantly composed of the sand fraction 95.6 %, with a lower portion of the silt fraction 4.4%. The sediments of EM 4 are moderately sorted, positive (fine-grained) skewed, and mesokurtic. This implies a high-energy depositional setting.

EM 4 occurs in 55.5 % of all samples over the NH-T section, and with a portion of 4.4 %, contributing the least of all EMs. EM 4 has a relatively significant and moderate positive correlation with MZ and MS, respectively.

Therefore, we suggest that EM 4 primarily represents sand-sized erosional material, possibly transported over a short distance from nearby sandy areas (such as riverbeds) or derived from the adjacent mountains by strong overland flow during heavy rainfall. Consequently, EM 4 may serve as a sensitive indicator of hydrodynamic conditions within the catchment.

The modern riverbed sands deposited near the mouths of the Muhua and Gongba rivers within the Daihai Lake catchment area, Inner Mongolia, show modal grain sizes of 300 and 395 µm, respectively (Xiao et al., 2013). These modal sizes, similar to our EM 4, fall within the 200-400 µm range, characteristic of the dominant saltation component of typical fluvial deposits.

In addition, the sandy materials of EM 4 might have resulted from neotectonic periods of relief rejuvenation with the establishment of surface ruptures along faults in the Nihewan Basin, particularly the Youfang Fault, which was reported to have caused a vertical displacement of approximately 30 m in the sediment sections in the study area (Deng et al., 2008; Moghazi et al., 2024a).

We conclude that the fine sands of EM 4 probably point to occasional extreme hydrologic events such as the occurrence of heavy summer-monsoon rains in the basin, and also to erosion of unconsolidated sediments exposed along surface ruptures of tectonic faults.

Correlation between EMs

Statistical analysis shows that EM 1 is negatively correlated with both MZ and other EMs. However, the strength of this negative correlation varies from the weakest with EM 2 to the strongest with EM 3 (Table 2.3, Fig. 23.3). The resulting correlation supports the above-mentioned interpretation about the difference in the original loess-source areas behind the

EMs 1-3. Moreover, the moderate negative correlation between EM 1 and MZ indicates that EM 1 probably originated from more remote sources than the other EMs.

The lower negative correlation of EM 2 with MZ in comparison with EM 1 implies that the EM 2 sediments were probably deposited at a nearer-sediment source by shorter-distance transport. The moderate positive correlation of EM 3 with MZ, and its moderate and strong negative correlation with EM 2 and EM 1, respectively, support the origin of EM 3 from relatively local loess sources with different transport dynamics than EMs 1 and 2.Following these correlations and inferences, we suggest that the relative abundances of the EMs 1 and 3 in the NH-T section (Fig. 22.3, Fig. 27.3) are valuable proxies to better understand the climate-driven environmental changes in response to the changes in Asian monsoon intensity in the Nihewan Basin during 1.66-0.78 Ma.

CONISS cluster analysis produced nine distinct zones (stages 1-9) based on the stratigraphic variations of the relative abundance of both EM 1 and EM 3 to comprehensively track the evolution of the EASM and EAWM over a period of 0.88 Ma in the basin.

Table 3.3 *Variations in the average contribution of EMs through the six depositional environments in the Nihewan Basin identified by Moghazi et al. (2024a)*

Height (m)	Depositional environments	EM 1 %	EM 2 %	EM 3 %	EM 4 %
74.0- 86.2	Wetland-lake	38.4	22.6	36.3	2.6
55.8-74.0	wetland-alluvial plain	42.0	23.2	27.8	6.8
39.3-55.8	Wetland-lake	52.2	24.2	19.8	3.5
30.4-39.3	Wetland- alluvial plain	62.0	12.0	19.5	6.3
15.5-30.4	Wetland	64.2	17.2	14.6	3.8
0.0-15.5	Wetland-lake	56.2	17.3	23.6	2.8

3.6.2 Relationship between the NH-T sediment section and the palaeoclimatic record of the CLP

The inference to use EMs 1 and 3 as proxies of the EASM and EAWM, respectively, implies that these EMs might have responded to global climate change in a comparable way as the soil and loess horizons in the CLP. Two distinct coarse loess marker layers L_{15} and L_{9-1} at ca. 1.25 and 0.9 Ma (glacial stages MIS 38 and MIS 22), respectively, were recognized in the median grain size stack of the CLP (CLP MD) for the last 1.6 Ma (Fig. 27.3; Liu, 1985; Ao et al., 2023). These two prominent horizons of coarse loess probably correspond to the two pronounced peaks in the EM 3 component curve at 41.3 and 76 m (Fig. 27.3). Above L_{15}, the exceptional palaeosol horizon S_{13} (ca. 1.17 Ma) was identified by Han et al. (2020) based on the high MS (Fig. 27.3b). This period of prevailing EASM likely corresponds to the maximum of EM 1 at 49 m in the NH-T section. The stratigraphic distribution of these three marker layers in the NH-T section supports the proposed timeframe of sediment accumulation between ca. 1.7 and 0.9 Ma suggested by Moghazi et al. (2024a). Based on these three marker layers, additional correlations of the CLP and EM 3, and of the MS stack of the CLP (CLP MS) and EM 1, respectively, MD stack suggest that the CLP and Nihewan Basin experienced similar palaeoenvironmental changes as a result of global climate variations in the Early Pleistocene (Fig. 27.3; Ao et al., 2023). We also observed that the overall pattern of the EM variations in the NH-T section is characterized by moderate oscillations at shorter intervals in the lower part (0.0-35.8 m), large oscillations with relatively longer intervals in the middle (35.8-77.0 m), and a return to moderate oscillations with shorter intervals in the upper part of the section (77.0-86.2 m). This pattern is relatively comparable with the pattern observed in the CLP record (Fig. 27.3b; Ao et al., 2023). The similar patterns support the inferred stratigraphic consistency of the Early Pleistocene NH-T sediment section and the climatic sensitivity of the identified EMs in response to the long-term glacial/interglacial oscillations previously inferred from the CLP records.

Astronomical age model of the NH-T sediment section

The cycle-to-cycle matching of EM 1 and EM 3 to the CLP MD and CLP MS stacks resulted in an age frame corresponding to the palaeosols S_{23}-S_7 and loess L_{23}-L_{9-1} layers (Fig. 27.3). This correlation is consistent with the orbital tuning results obtained from the correlation of EM 3 and the CLP MD record (Fig. 26.3). As a result, the NH-T sediment section is assigned an astronomically tuned age range of 1.66-0.78 Ma.

3.6.3 Palaeoenvironmental and palaeoclimatic changes in the Nihewan Basin during 1.66-0.78 Ma

Based on the discussion of the EMs 1-3 and related sources and transport mechanisms, the history of the EASM (EM 1), of dust-storm outbreaks during springtime (EM 2), and of the EAWM (EM 3) is inferred from the NH-T section.

Stage 1 (0.0-1.2 m) represents a high EM 1 peak. ***Stage 2*** (1.2-10.4 m) is characterized by dominant high EM 3 peaks (Fig. 27.3a). During ***stage 3*** (10.4-39.0 m), EM 1 predominates. ***Stage 4*** (39.0-48.1 m) is characterized by the prevalence of EM 3, whilst ***stage 5*** (48.1-57.0 m) is dominated by high peaks of EM 2. EM 3 dominates in ***stage 6*** (57.0-61.0 m). ***Stage 7*** (61.0-74.0 m) shows a highly oscillated pattern of EM distributions, with EMs 1-3 showing relatively equal proportions of predominance throughout this stratigraphic zone. EM 3 clearly dominates in the sediments of ***stage 8*** (74.0-78.9 m). ***Stage 9*** (78.9-86.2 m) is dominated by EM 1. This pattern suggests that the NH-T section probably underwent a strong EASM (warm-wet) period in ***stage 1***. Subsequently, one main predominating EAWM (cold-dry) period is identified in ***stage 2***, whilst ***stage 3*** is characterized by seven warm-wetter periods alternating with six cold-dry intervals. Moreover, the NH-T section apparently experienced seven main cold-drier periods interrupted by five warm-wetter intervals in ***stages 4-8***. Eventually, in ***stage 9***, two main warm-wetter periods are identified. These climatic conditions are possibly synchronous with the interglacials (S_{23}-S_7), and glacial periods (L_{23}-L_{9-1}) in the CLP (Fig. 27.3b; Ao et al., 2023). Furthermore, the U-ratio (16-44 μm/5.5-16 μm) (Vandenberghe et al. 1985, 1997) and grain size index (GSI: 21-52 μm/<21 μm) (Antoine et al., 2009) are commonly used proxies for tracking variations in the past wind intensity in the CLP records (Ao et al., 2023). Through the NH-T section, low and relatively constant U-ratios and GSI values <2% are observed in ***stages 1***, ***3***, ***5*** and ***9*** indicating weak winds, consistent with dominant EASM conditions in these stages (Fig. 27.3a). In contrast, higher U-ratios and GSI values are found in ***stages 2***, ***4***, ***6*** and ***8***, reflecting stronger winds, associated with dominant EAWM conditions (Fig. 27.3a).

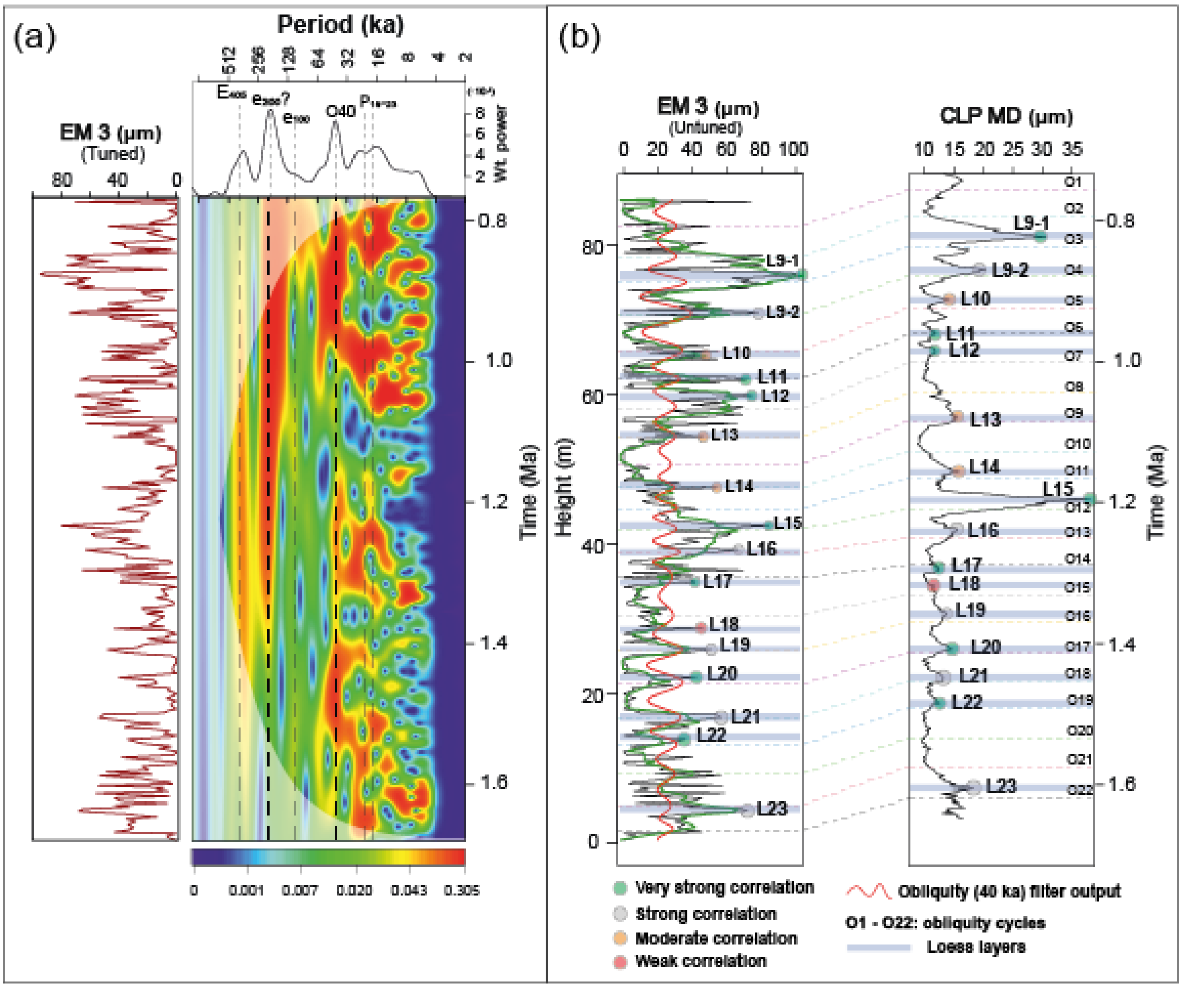

Figure 26.3 *Cyclostratigraphic analysis of the NH-T section using the EM 3 proxy. (a) Continuous Wavelet Transform (CWT) of the EM 3 proxy after orbital tuning to La2004 (Laskar et al, 2004) astronomical solution. (b) Correlation of the interpreted obliquity filter output (see Supplementary Figure S 2 for details) to the 41-ka obliquity filter of the EM 3 after tuning, plotted against the tuned CLP MD record. Colourful dashed lines indicate obliquity tie points, anchored to the La2004 astronomical solution (Laskar et al., 2004)*

Thus, the climate archive of the NH-T section indicates a change from strong EASM conditions in ***stage 1*** into EAWM conditions in ***stage 2*** and then a return to EASM conditions in ***stage 3*** during ca. 1.66-1.62, 1.62-1.52 and 1.52-1.20 Ma, respectively. The EAWM dominated during ***stages 4***, ***6*** and ***8*** between ca. 1.20-0.82 Ma whilst the EASM was at least partly strong during the intervening ***stages*** *5* and *7*, and also subsequently in ***stage 9*** after ca. 0.82 Ma.

A comparison of the MD stack of the CLP and EM 3, and the MS stack and EM 1 shows that glacial conditions in the Nihewan Basin may have been less pronounced during the formation of loess layers L_{20} and L_{17}. In contrast, the Nihewan Basin probably underwent more enhanced glacial conditions than in the CLP during the accumulation of loess layers L_{18} and L_{13}. On the other hand, interglacial conditions were apparently more prominent in the Nihewan Basin during the formation of palaeosols S_{21} and S_{16}, and less prominent during the formation of S_{20} and S_{14}. The intensified Siberian High possibly drove more pronounced glacial conditions during the L_{18} and L_{13} periods in the Nihewan Basin compared to the CLP under global cooling. In contrast, the stronger glacial conditions in the CLP during the L_{20} and L_{17} periods were probably due to increased continental aridification in the Asian interior relative to the Nihewan Basin. The enhanced interglacial conditions during the S_{18} and S_{14} periods in the CLP, and in contrast in the Nihewan Basin during the S_{22} and S_{16} intervals, possibly resulted from spatial variations in monsoonal precipitation and moisture source areas (Liu et al., 2014).

In the eastern part of the N China Plain, Zhou et al. (2018) reconstructed the vegetation history derived from pollen records, suggesting that the region was predominantly covered by closed needle-leaved and broadleaved mixed forest between ca. 1.7-1.2 Ma. During ca. 1.2-0.9 Ma in the N China Plain, there was a decline in coniferous forest and a significant increase in *Artemisia*, Chenopodiaceae and Poaceae grassland plants, indicating an overall aridification trend (Zhou et al., 2018). This recognizable vegetation change is consistent with the shift from dominant warm-wet conditions in ***stages 1*** and ***3***, into the up-section increasing trend of dominant cold-dry conditions from ***stage 4*** to ***8*** (Fig. 27.3a). Additionally, the up-section gradual decreasing trend of EM 1 from the lower part of ***stage 3*** to ***stage 8*** (Fig. 27.3a) is possibly synchronous with the long-term decreasing trend in chemical weathering intensity inferred from the mineral magnetic record of the Jingbian loess/paleosol sequence at the northern margin of the CLP due to the increasing Asian aridification and cooling over the last 2.6 Ma (Deng et al., 2006a, 2006b).

Ao et al. (2023) stated that the intensification of the glacial Asian climate coincided with Northern Hemisphere ice-sheet expansion in the context of the global cooling at the onset and in the middle of the Mid-Pleistocene transition (MPT) (ca. 1.25-0.9 Ma). The Mu Us Desert adjacent to the Nihewan Basin also underwent a southward expansion at ca. 1.25 Ma (Ding et al., 2005). Zeng et al. (2016) argued that the loess accumulation since ca. 1.22 Ma coincided with the large expansion of the Eurasian loess belt during the late Early Pleistocene. Therefore, we speculate that the enhanced aridity and cooling conditions in ***stage 6*** within the age interval of L_{12} (1.0-0.96 Ma) were related to the expansion of ice sheets and deserts. This expansion resulted in the strengthening of the EAWM which probably dominated the NW transport pathways and increased the coarse dust supply towards the Nihewan Basin more than to the CLP during this period. With the lowering of the global sea level during the MPT (Lisiecki and Raymo, 2005; Rohling et al., 2014), most of the Yellow Sea and significant parts of the E China Sea and S China Sea may have turned into land and made N China nearly twice as remote from maritime influences (Nakagawa et al., 2008; Dai et al., 2023; Xu et al., 2024). These changes probably caused the stronger aridification recorded in the Nihewan Basin during the formation of L_{12}.

Corresponding to the glacial-interglacial cyclicity change documented in the marine $\delta^{18}O$ record (Lisiecki and Raymo, 2005), the change in the EM patterns from short-frequency fluctuations to longer fluctuations at 1.25 Ma apparently coincided with the onset of the MPT which marks a major shift in global climate from the symmetric 41-ka obliquity to the asymmetric 100-ka eccentricity orbital periodicities.

In conclusion, the overall increase of EM 3 peaks and related decrease of the EM 1 minima in the NH-T section from ca. 1.45-0.82 Ma indicate a long-term aridification and cooling trend in the Nihewan Basin. Higher frequency fluctuations of the EMs were replaced bylower frequency variations at 1.25 Ma, possibly as a result of the onset of the MPT. The Nihewan Basin was probably characterized by a relatively strong EASM with more frequently warm and wet conditions between ca. 1.66-1.62, 1.52-1.25, and after ca. 0.82 Ma. During the intervening periods, the EAWM prevailed with colder and drier conditions.

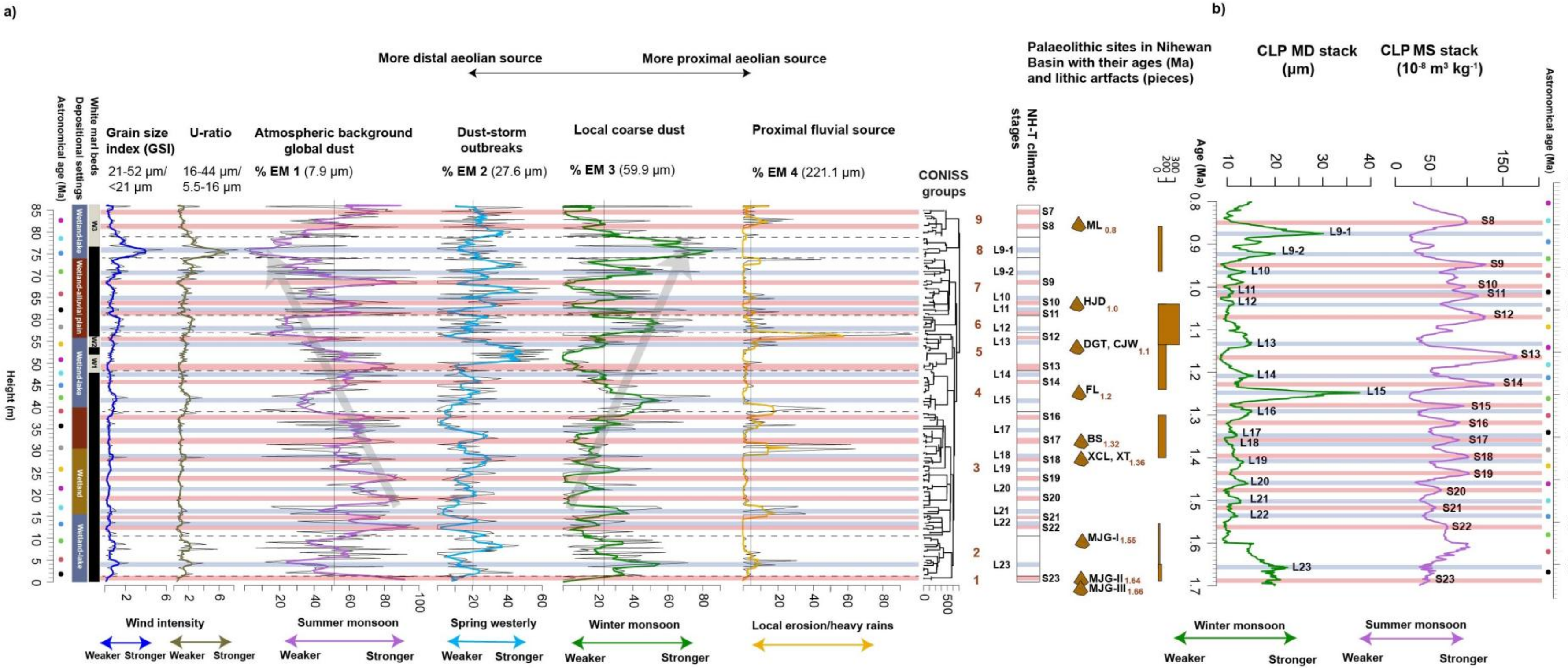

Figure 27.3 (a) Variation in the relative abundance of End Members (EMs) 1-4 through the NH-T section (5-point running means in violet, light blue, green, and yellow, respectively, with a vertical line representing the mean) plotted against height (m). Dashed horizontal lines, derived from CONISS cluster analysis of EMMA, marks the seven distinctive zones. U-ratios and GSI are calculated from the grain-size data of Moghazi et al. (2024a) (5-point running mean in blue and olive green). (b) Chinese Loess Plateau median grain size stack (CLP MD) and magnetic susceptibility stack (CLP MS) (L loess in blue, S palaeosol in red) by Ao et al. (2023). Red and blue bars in (a) and (b) respectively indicate correlated glacial and interglacial cycles between NH-T and CLP sediment sections. Below 1.6 Ma, the S_{23} from Luochuan section of the CLP is redrawn from Han et al. (2020). The Palaeolithic sites in the Nihewan Basin are MJG-III = Majuangou III (Zhu et al., 2004), MJG-II = Majuangou II (Zhu et al., 2004), MJG-I = Majuangou I (Zhu et al., 2004), XT = Xiantai (Deng et al., 2006a, 2006b), XCL = Xiaochangliang (Zhu et al., 2001), BS = Banshan (Zhu et al., 2004), FL = Feiliang (Deng et al., 2007), DGT = Donggutuo (Wang et al., 2005), CJW = Cenjiawan (Xie and Cheng, 1990), HJD = Huojiadi (Liu et al., 2010), ML = Maliang (Wang et al., 2009), Geomagnetic Polarity Time Scale (GPTS) (Hilgen et al., 2012)

3.6.4 Implications of the Early Pleistocene climate change for the hominin occupation in the Nihewan Basin

The Nihewan Basin in the Old World is a key region for the long early human activities in northern China. The archaeological excavations in the basin have yielded key findings of stone tools dating back from ca. 1.66 Ma to 11.7 ka (Yang et al., 2019). The overall evidence of our study suggests that the relatively high-latitude Nihewan Basin was marked by significant environmental and long-term climatic fluctuations during the period from 1.66-0.78 Ma. The presented evidence shows that the Nihewan Basin tracked the interglacial-glacial oscillations, and a long-term aridification and cooling trend which was recorded as distinct vegetation shift from coniferous forest to grassland plants by Zhou et al. (2018, 2023) in the North China Plain and by Wu et al. (2007) in the CLP. Zhu et al. (2007) argued that early humans apparently inhabited the environment of the Nihewan Basin between 1.66-0.78 Ma. From 1.1-0.96Ma, the warm climate conditions inferred from two significant EM 1 peaks equivalent to S_{12} and S_{11}, imply favorable conditions for early humans. Subsequently, the cold climate conditions inferred from the densely spaced EM 3 maxima between 1.0 (L_{12}) and 0.82 Ma (L_{9-1}) might have driven early humans to relocate to more hospitable locations in E Asia. The inferred climate change from warm to cold conditions possibly explains the dramatic up-ward decline in hominin site numbers and artefact densities between 1.0-0.9 Ma in the Nihewan Basin and North China (Yang et al., 2021).

This observation aligns with Dennell's (2013) suggestion that early humans were probably not year-round or during cold periods in the Nihewan Basin. Accordingly, the majority of the Early-Middle Pleistocene hominin sites of the basin corresponds to the interglacial periods of the marine oxygen isotope record (Zhang et al., 2024). Yang et al. (2019) further suggested that the continuous presence of early humans in relatively high latitudes such as the Nihewan Basin was not possible prior to the late Pleistocene (after 0.126 Ma). Alternatively, Xu et al. (2023) stated that early humans inhabited the Nihewan Basin at the onset of the MPT since they adapted successfully to the harsh local environments and developed flexible and innovative technological strategies. Their findings are supported by the suggestion of Pei et al. (2019) that early humans might have continuously rather than sporadically occupied the Nihewan Basin.

Our inferences, coupled with previously documented archaeological findings and the updated chronostratigraphic framework of Nihewan sediments (Fig. 27.3a; Tu et al., 2022; Ye et al., 2024), indicate that relatively warm and wet conditions in the Nihewan Basin during ca. 1.66-1.62, 1.52-1.20 and after 0.82 Ma supported hominin activities whilst colder and drier conditions between ca. 1.62-1.53 and 1.20-0.82 Ma provided a less hospitable background for hominins. However, a higher number of discovered Palaeolithic sites and lithic artefacts were recorded during ca. 1.2-1.0 Ma (Yang et al., 2019), suggesting the successful adaptability of hominins to the local environmental conditions in the first half of the MPT despite of the prevailing harsh colder climate.

3.7 Conclusions

Based on a first application of unmixing Early Pleistocene grain-size data for sediment samples from the Nihewan Basin with EMMA, the following conclusions are drawn:

- The four identified EMs explain 98% of the total variance within the grain-size fractions of the NH-T sediment samples.
- The four EMs represent either distal sources of a) fine silt-sized sediments (EM 1; 7.9 μm), b) medium silt-sized sediments (EM 2; 27.6 μm), or proximal sources of c) coarse silt-sized sediments (EM 3; 59.9 μm) and d) fine sand-sized sediments (EM 4; 221.1 μm) with mean contributions of 51.4, 20.2, 24.0 and 4.4 %, respectively.
- The EMs 1-3 resemble the loess deposits of the CLP and serve as valuable proxies to track the intensity of the EASM, the dust-storm outbreaks during spring and the EAWM, respectively, indicating the three main dynamics which controlled dust transport to the study region between ca. 1.66-0.78 Ma.
- An overall increase in EM 3 peaks, along with a decrease in EM 1 minima in the NH-T section from ca. 1.45 to 0.82 Ma, point to a long-term aridification and cooling trend in the Nihewan Basin.
- The shift in the EM patterns from short-frequency fluctuations to longer fluctuations at ca. 1.20 Ma apparently coincided with the onset of the MPT.
- Stronger EASM conditions prevailed in the Nihewan Basin between ca. 1.66-1.62, 1.52-1.20 and after 0.82 Ma, whereas the EAWM intensified significantly in the intervening intervals from ca. 1.62-1.52 and 1.20-0.82 Ma.
- Inferred mostly warmer and wetter conditions in the Nihewan Basin from ca. 1.66-1.62, 1.52-1.20 and after 0.82 Ma provided a more favorable environment for hominin activities in contrast to mostly colder and drier conditions between ca. 1.62-1.52 and the MPT (1.20-0.82 Ma).
- Nevertheless, additional geochemical analyses of the major, trace, and rare earth element (REE) compositions of the studied sediments and those of other sections in the basin are necessary to further support inferences of the sediment sources and the reconstructed palaeoenvironmental and palaeoclimatic conditions inferred from EMMA.

3.8 Supplementary information

Table S1 *Litho- and bio-facies characteristics of the NH-T composite section*

Sedimentary zones	**Height (m)**	**Facies types**	**Lithofacies code**	**Lithological description**	**Sedimentary structures** ^{a}	**MS & χ_{FD}** ^{b}	**Ostracods & other fauna**
15	78.7-86.2	2	**F** (Sh)	Primarily medium- very coarse massive silt	Three HB at 79.1-79.5, 79.7-82.0, 82.2-85.8 m	χ_{FD}^{++} at 79.3-80.1, 82.5 m	*Cytherissa lacustris****, *Leucocythere* sp.** , Juv. Candoninae**
14	74.2-78.7	3	**F** (Sh + Sr)	Mostly very coarse massive silt	HB at 75.4-76.8 m RL at 76.0-76.6 m	χ_{FD}^{++} at 78.4 m	*Leucocythere* sp.***, *Ilyocypris* sp.**, *Cytherissa lacustris**
13	69.0-74.2	2	**F** (Sh)	Mainly coarse-very coarse massive silt	Three HB at 69.0-70.5, 70.9-71.2, 71.7-73.8 m	χ_{FD}^{++} at 69.5 m	*Leucocythere* sp. ***
12	60.1-69.0	3	**F** (Sh + Sr)	Primarily medium-coarse massive silt with burrows	HB at 67.3-69.0 m Five RL at 61.5-61.7, 61.9-62.4, 62.9-63.1, 64.1, 65.8-66.3 m	χ_{FD}^{++} at 69.0 m	*Ilyocypris* sp. ***
11	57.1-60.1	6	**F** (Sr)	Mostly very coarse massive silt	Two RL at 57.4-57.6, 58.1-58.6 m		*Ilyocypris* sp.***, *Limnocythere* sp.**, vertebrate remains*
10	56.2-57.1	5	**F + S** (Sp)	Mainly coarse silt-medium massive sand	XB at 56.2-56.9 m	MS^{++} at 56.4-56.6 m	*Limnocythere* sp. ***
9	53.0-56.2	2	**F** (Sh)	Primarily coarse massive silt	Two HB at 53.9-54.7, 54.9-56.2 m		*Limnocythere* sp. ***
8	43.2-53.0	2	**F** (Sh)	Mostly medium-coarse massive silt with burrows	HB at 45.2-45.6 m	χ_{FD}^{++} at 43.6, 47.6, 50.4, 52.2 m	*Limnocythere* sp.***, *Cytherissa lacustris***, *Leucocythere* sp.**
7	38.6-43.2	3	**F** (Sh + Sr)	Mainly coarse massive silt	HB at 39.8-40.3 m Two RL at 38.6-38.8, 42.1-42.2 m	MS^{++} at 39-39.6 m	*Limnocythere* sp.***, *Ilyocypris* sp.**, *Heterocypris salina***
6	34.6-38.6	4	**F** (Sh + Sr + Sp)	Primarily medium-coarse massive silt with and burrows	HB at 35.7-35.9 m RL at 38.3-38.6 m XB at 36 m	MS^{++} at 38.6, χ_{FD}^{++} at 35.6-35.8 m	*Ilyocypris* sp.***, *Limnocythere* sp.**, *Heterocypris salina**
5	29.3-34.6	3	**F** (Sh + Sr)	Mostly medium-coarse massive silt	HB at 31.4-33.8 m RL at 31.1-31.2 m	χ_{FD}^{+++} at 32.3, 33.4 m, χ_{FD}^{++} at 29.4-29.7 m, 30.7-31, 31.4-31.6, 34 m	*Limnocythere* sp.***, *Ilyocypris* sp.**
4	24.1-29.3	2	**F** (Sh)	Mainly medium-coarse massive silt	HB at 24.1-24.6 m	χ_{FD}^{+++} at 26.9, 27.4 m, χ_{FD}^{++} at 24.8, 26.4, 27.6 m	*Ilyocypris* sp.***, *Heterocypris salina***, *Limnocythere* sp.**

3	15.3-24.1	2	**F** (Sh)	Primarily medium massive silt with burrows	Three HB at 17.2- 18.4, 18.5-19.2, 22.5-24.1 m		χ_{FD}^{+++} at 19.4, 23.3 m, χ_{FD}^{++} at 16.1, 19.7-21.8 m	*Limnocythere* sp.****Ilyocypris* sp***Heterocypris salina***Juv. Candoninae*gastropods*
2	4.6-15.3	2	**F** (Sh)	Mostly medium-coarse massive silt with burrows	Seven HB at 5.8-5.9, 6.0-6.1, 6.4-6.6, 6.7-6.8,7.3-7.4, 8.9-9.1, 12.0-12.1 m		χ_{FD}^{+++} at 7.3 m, 14.2 m, χ_{FD}^{++} at 4.8 m, 9.8-13.6 m, 14.4-15.1 m	*Ilyocypris* sp.*** *Limnocythere* sp.** *Leucocythere* sp.***Cytherissa lacustris**
1	0.0-4.6	1	**F** (Sh + Sp)	Mainly coarse-very coarse massive silt with carbonate nodules	Two HB at 0-1.7, 2.3-2.4 m	XB at 3.4-3.5 m	χ_{FD}^{+++} at 3.7 m, χ_{FD}^{++} at 1.3-1.8 m and 4.3 m	*Leucocythere* sp.****Ilyocypris* sp.***Limnocythere* sp.** gastropods*

[a] The sediments are otherwise homogeneous.

[b] The sediments have otherwise low magnetic susceptibility (MS) and frequency-dependent magnetic susceptibility (χ_{FD}) (≤ 2).

***Dominant **Common **rare $^{+++}$high $^{++}$moderate

F Massive caly and silt, **Sh** Horizontally bedded, **Sp** Planar cross-bedded, **Sr** Ripple-bedded

HB horizontal bedding, **RB** ripple bedding, **XB** cross bedding, **RL** ripple lamination, **HL** horizontal lamination, **RM** ripple marks

Lithofacies codes follow the lithofacies associations of Miall (1978)

Times-series analysis and orbital tuning of the EM 3 record

Time-series analysis was performed on the EM 3 signal. Prior to analysis, the EM 3 data series was detrended and interpolated linearly at 28.5 cm intervals (average sampling spacing). Cyclicities were estimated using the Multi-taper Method (2π-MTM) (Thomson, 1982) using Astrochron R package (Meyers, 2014). The MTM is coupled with AR1-CL (Autoregressive Confidence Level) and F-test harmonic confidence level estimate. The resulting power spectrum (Supplementary Figure S 1) shows prominent cycles at 17 m, 6 m, 5 m and 4 m often exceeding 95% of the statistical CL. The initial timescale was provided by Moghazi et al. (2024a) and suggests that the total duration of the NH-T section is 0.8 Ma. This implies that the 4-6 m wavelength band is interpreted as the Earth axial tilt (obliquity cycles) component of the astronomical frequencies in the EM 3 signal. The Continuous Wavelet Transform (CWT) techniques serve to assess the evolution of astronomical components in the EM 3 proxy and to track the sediment-accumulation rate variations along the studied section. Prominent orbital cycles (in the stratigraphic domain) were extracted by band-pass filtering using the Taner filter (Taner, 2000) of the "Filtering" function using *Astrochron* R package (Supplementary Figure S 2). The observed cycles are then linked to their corresponding astronomical cycles, followed by manually tracking the period of the best expressed 41-ka cycles in wavelet scalograms using the "*track_period*" function under Waverider R package (Arts, 2023). The resulting tracked obliquity cycles (Supplementary Figure S 3b) were used to tune the EM 3 record to the La2004 (Laskar et al., 2004) obliquity cycles between 0.8 Ma and 1.7 Ma, using astro_anchor.R function of the Waverider R package (Arts, 2023). The point-by-by-point anchoring processes is shown in Supplementary Figure S 6b. The EM 3 data series is therefore tuned to absolute times offering an independent timescale for the analysed section. Afterwards, we carried out the MTM analysis of the tuned EM 3 signal, which shows a strong and significant expression of the 41-ka obliquity cycles (Supplementary Figure S 4). An additional powerful peak appeared around 200-ka cycles which could be linked to the 200-ka orbital eccentricity (its corresponding filter is shown in Supplementary Figure S 6c). The resulting anchored ages were then applied to the CLP MD record, where colored horizontal lines (Fig. 26.3b in the main manuscript) representing these tie points were plotted on the CLP data to assess their alignment with key features (mainly powerful emerging peaks and trough) in the reference stack. The strong correlation observed between the obliquity-tied points in the EM 3 record and the CLP MD variations indicates a consistent and reliable alignment. This visual correlation supports the accuracy of the astronomical calibration, and the alignment of these tie points with significant transitions in the CLP MD record further validates the chronostratigraphic framework of our EM 3 signal, reinforcing its reliability for paleoclimatic reconstructions.

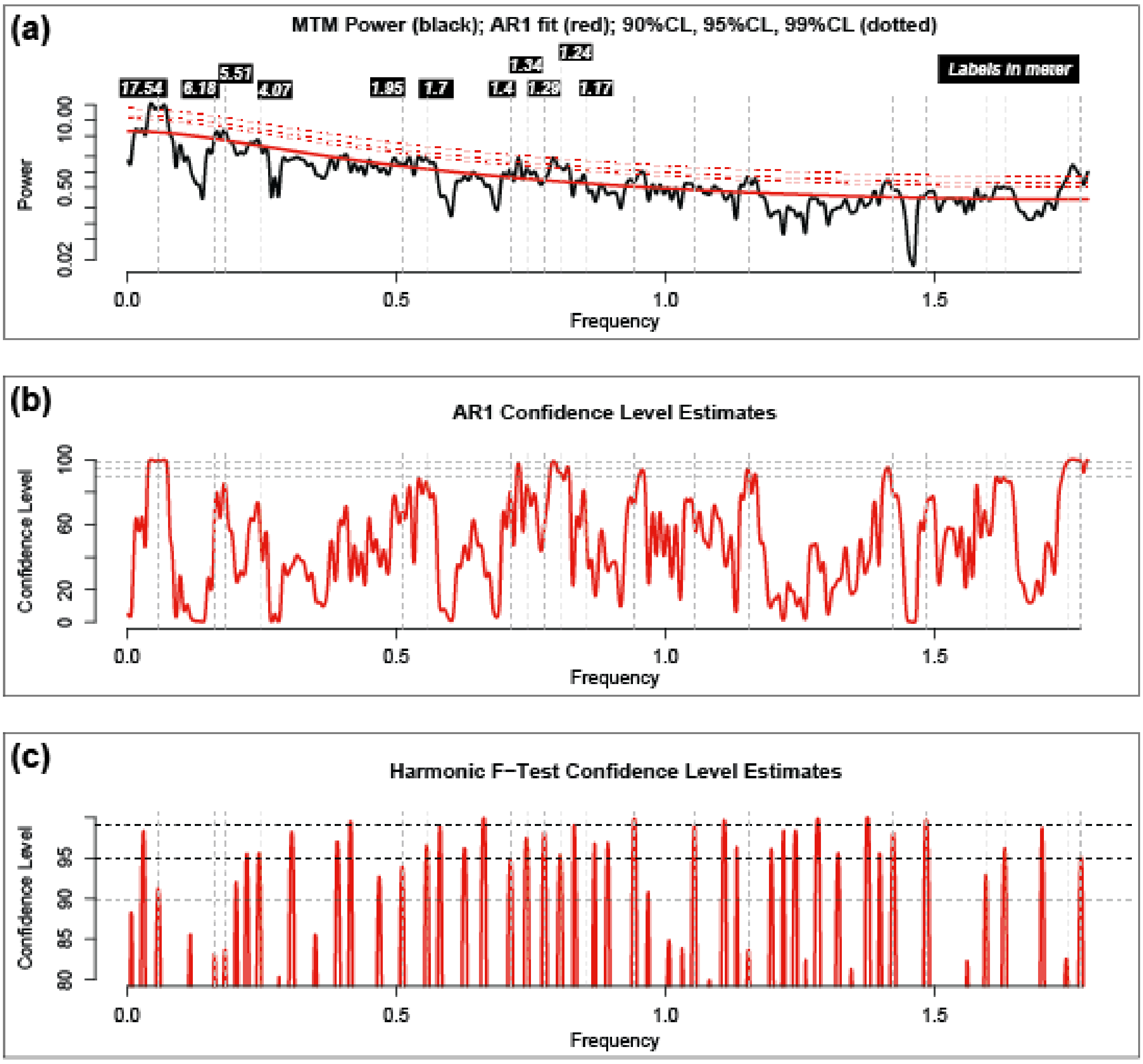

Fig. S.1 *2π-MTM (Thomson, 1982) power spectrum of the EM 3 record in depth domain showing (a) several prominent high-power peaks (wavelengths in m) and their corresponding statistical tests of (b) AR1 confidence level and (c) harmonic F-test level. The MTM was performed using Astrochron R package*

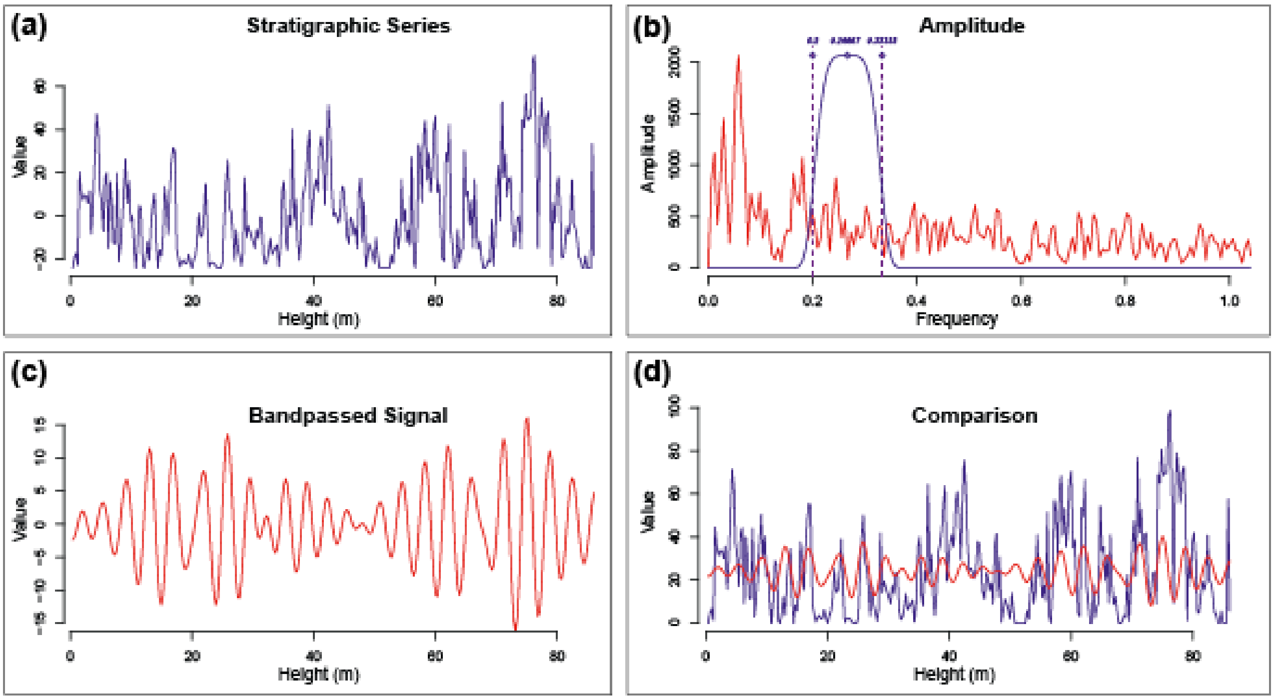

Fig. S.2 *Band-pass Taner filtering of the interpreted obliquity cycles (in depth domain) from the EM 3 signal. (a) The original stratigraphic record of the EM 3 proxy. (b) Taner-filter bandwidth as well as its central frequency (in blue) plotted on the MTM spectral power (in red). (c) The resulting output filter is (d) plotted on the original EM 3 stratigraphic record*

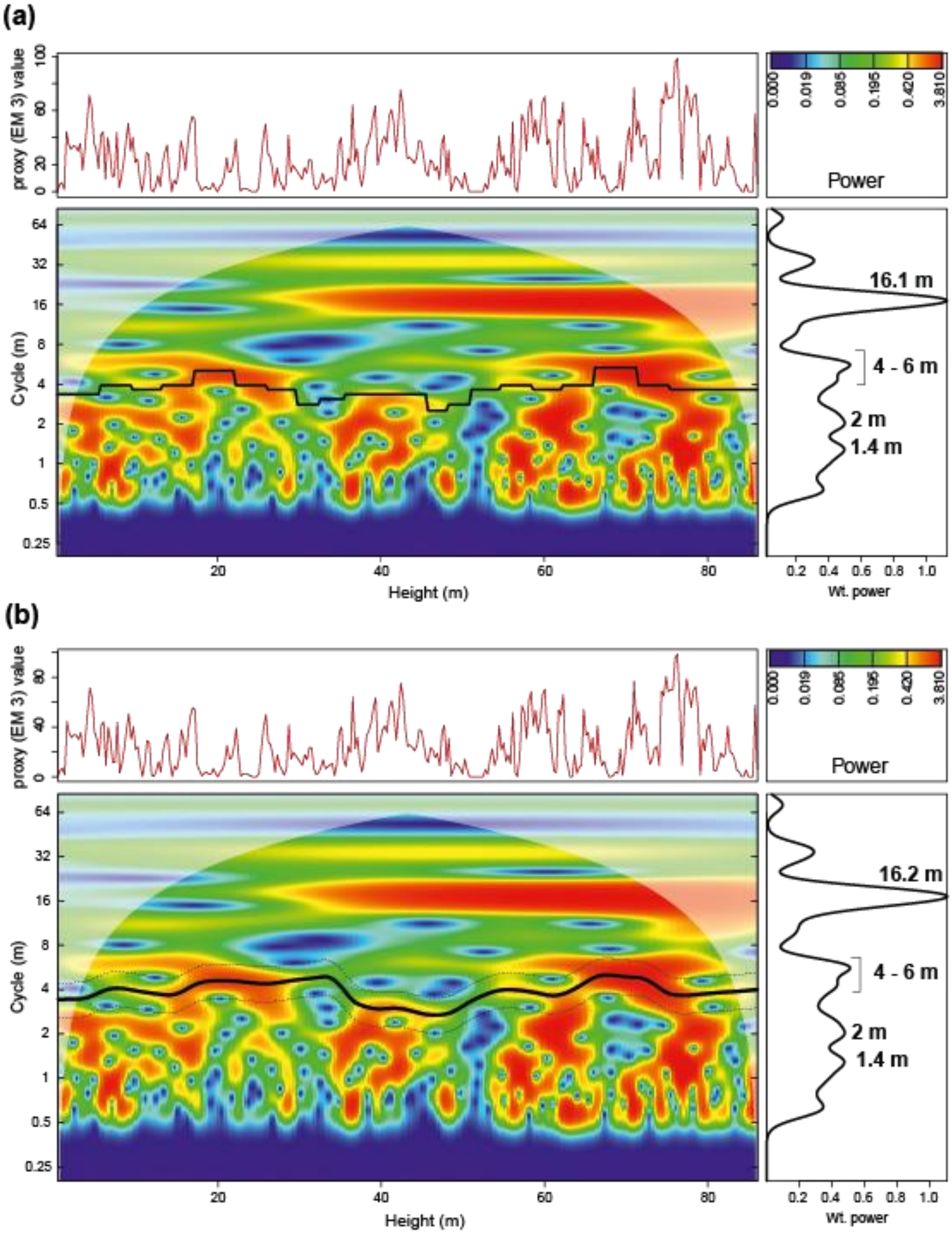

Fig. S.3 *Continuous Wavelet Transform (Morelet Wavelet) of the EM 3 record showing (a) the obliquity cycle tracking using the calculated individual thicknesses of orbital obliquity cycles derived from the 4-6 m filter output (shown in red line in Supplementary Fig. S.2.c). (b) Manually tracked obliquity cycles using "track_period" function under Waverider R package (Arts, 2023). Both tracking methods show similar paths. The tracked obliquity cycles in (b) were further used to tune the EM 3 record to the Laskar04 (Laskar et al., 2004) obliquity cycles between 0.8 Ma and 1.7 Ma*

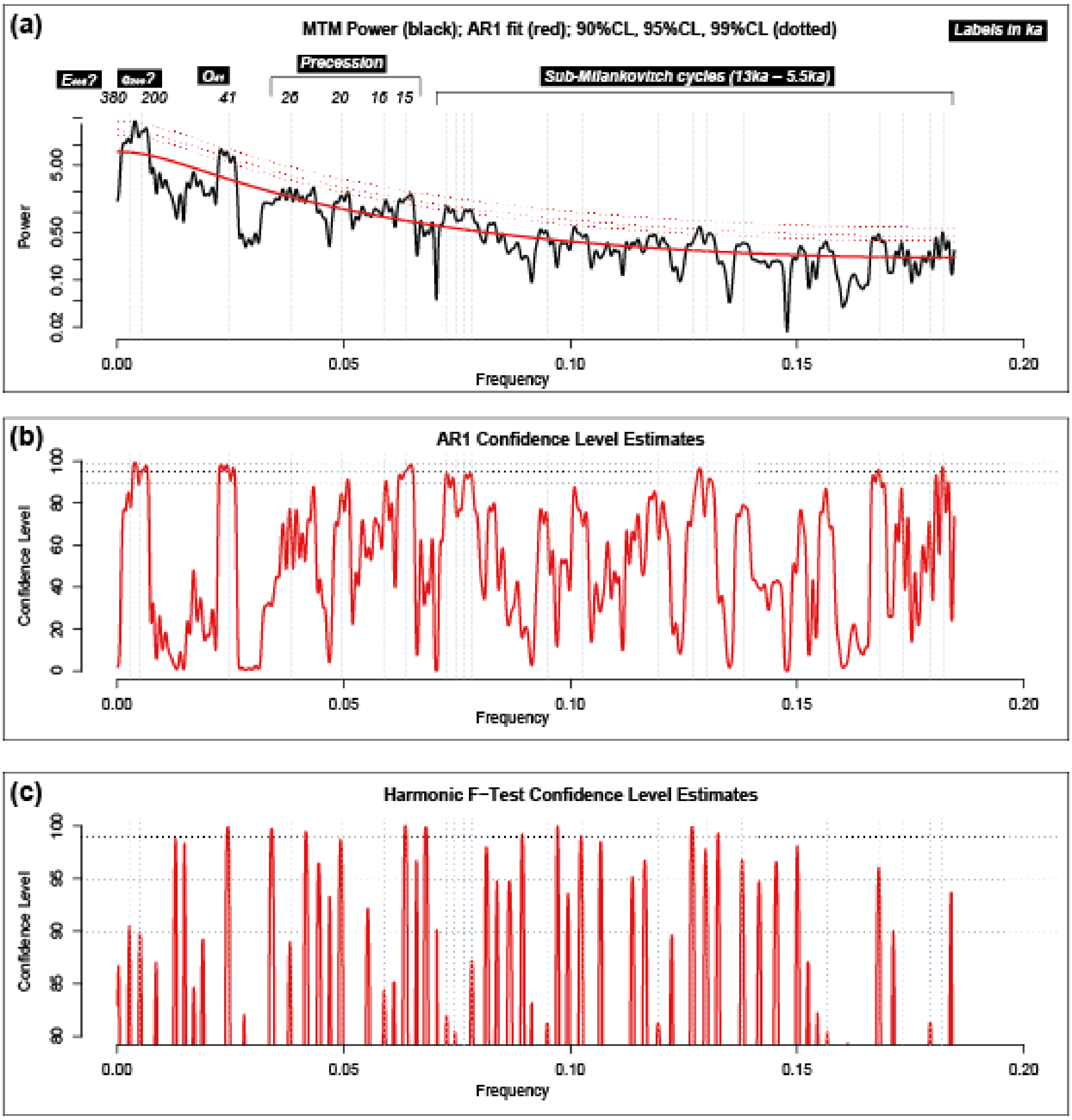

Fig. S.4 *MTM of the tuned data series. 2π-MTM (Thomson, 1982) power spectrum of the EM 3 record in time domain (after tuning to Laskar04 obliquity solution) showing (a) a strong expression of the long eccentricity cycles (referred herein as 380 ka cycles), 200 ka cycles as well as a strong expression of the 41 ka obliquity cycles. High-power peaks (period in ka) and their corresponding statistical tests of (b) AR1 confidence level and (c) harmonic F-test level. The MTM analysis was performed using Astrochron R package*

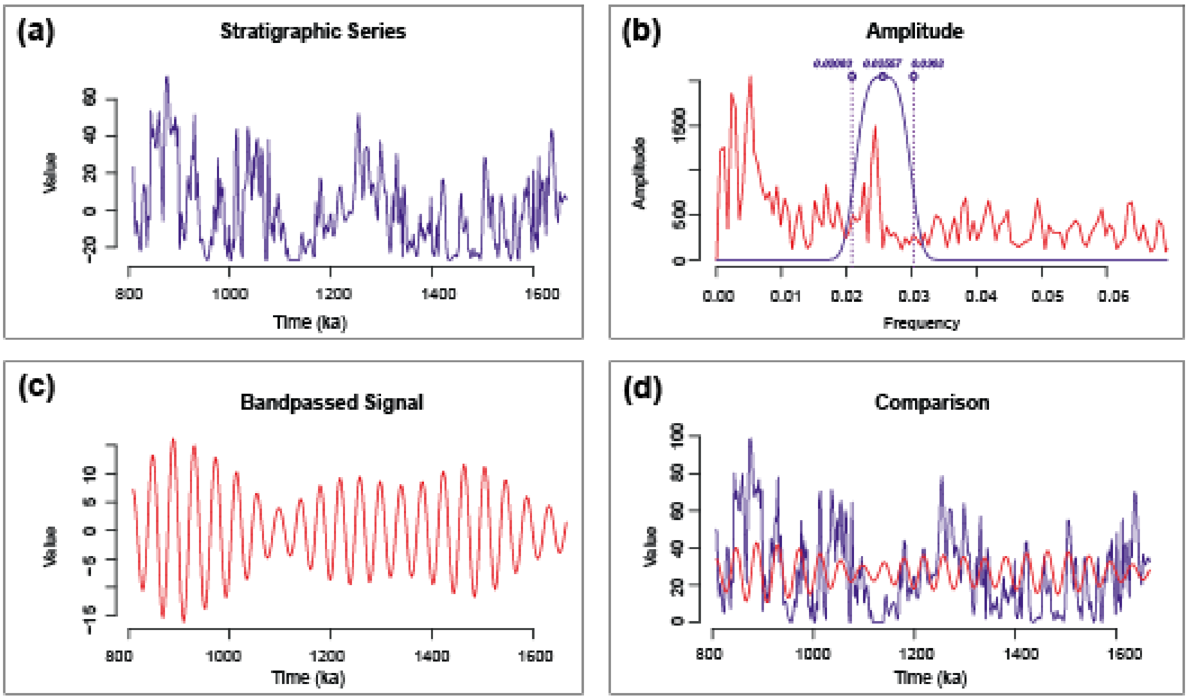

Fig. S.5 *Band-pass Taner filtering of the interpreted obliquity cycles from the EM 3 signal (a). The EM 3 data series plotted against time (ka) after tuning. (b) Taner-filter bandwidth as well as its central frequency (in blue) plotted against the MTM spectral power (in red). (c) The resulting output filter highlighting the 41 ka obliquity cycles. (d) Comparison of the tuned EM 3 record with the filtered obliquity cycles after tuning*

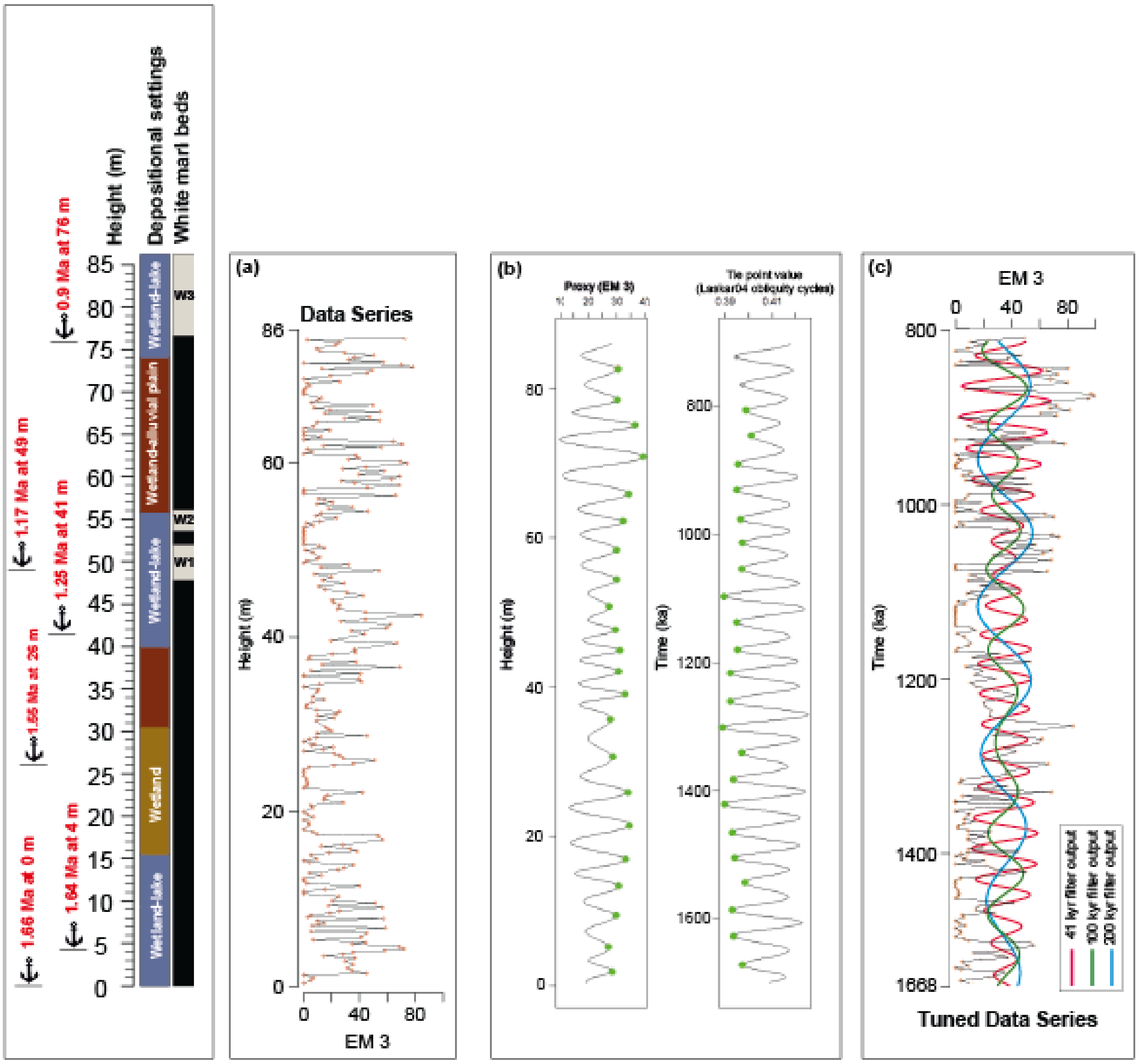

Fig. S.6 *Step-by-step astronomical tuning of the EM 3 record. The EM 3 record in the depth domain (a). Minimal tuning of the interpreted obliquity (4-6 m) filter output (left filter) to the Laskar04 (Laskar et al., 2004) obliquity solution (right filter; b). The filter was performed using astro_anchor.R function of Waverider R package (Arts, 2023). Obliquity maxima on the EM 3 record were tuned to obliquity cycles minima because higher grain size input of particle is forced by lower insolation of obliquity cycles minima. (c) The resulting tuned EM 3 data series plotted against the 400 ka, 200 ka and 41 ka filters output*

Manuscript III

4 Concurrent hydrological closure and hominin presence in the Early Pleistocene Nihewan Basin (northern China): insights from stable isotopes

4.1 Abstract

The Nihewan Basin in northern China contains rich Early Pleistocene Palaeolithic sites, representing one of the earliest locations of hominins outside Africa. Here, we present the first long-term stable oxygen ($\delta^{18}O_{eq.cal}$) and carbon ($\delta^{13}C_{eq.cal}$) isotope record derived from ostracod shells, preserved in the composite 86.2-m NH-T sediment section at the northeastern part of the basin, with a timeframe between ca. 1.67 and 0.78 Ma. The study aimed at reconstructing the long-term climatic changes and hydrological dynamics of the Early Pleistocene Nihewan Basin and to assess their impact on hominin activities. Unexpectedly, we found a strong covariance of $\delta^{18}O_{eq.cal}$ and $\delta^{13}C_{eq.cal}$ values, clearly suggesting that the basin was mostly hydrologically closed. The dominance of evaporation implies that $\delta^{18}O_{eq.cal}$ shifts track the hydrological state at the section location between closed settings with higher water levels (more standing waters) and open settings with low water levels (more flowing waters) instead of regional changes in precipitation/evaporation ratios alone. Moreover, we observed the concurrence of high $\delta^{18}O_{eq.cal}$ and $\delta^{13}C_{eq.cal}$ values and the increase in the marine-land temperature gradient (ΔT), indicating enhanced East Asian Summer Monsoon (EASM)-driven precipitation which led to wetter climate and increased biogenic productivity. Conversely, low $\delta^{18}O_{eq.cal}$ and $\delta^{13}C_{eq.cal}$ values reflect decreased EASM-driven precipitation and drier climate and reduced biogenic productivity. The new stable isotope data, combined with the synthetic archaeological record, suggest that hominin activities in the Nihewan Basin mostly coincided with periods of higher $\delta^{18}O_{eq.cal}$ and $\delta^{13}C_{eq.cal}$ values when more standing waters bodies and wetter climate prevailed in the region.

4.2 Introduction

Studying the Early Pleistocene is critical for our understanding of the past global climate variability and its inextricable link to hominin evolution, adaptation, and dispersal (Potts et al. 2020; Yang et al., 2021). From a geoarchaeological perspective, the Nihewan Basin in E Asia represents an especially promising research area due to its well-constrained, continuous sedimentary sequence that preserves an abundance of stone artefacts. Since the 1920s, the basin has been recognized for its long paleontological succession of the Early Pleistocene megafauna, known as the Nihewan Fauna (Teilhard de Chardin and Piveteau, 1930; Qiu, 2000).Today, it represents the densest concentration of Early Pleistocene Palaeolithic sites outside Africa (Zhu et al., 2004; Deng et al., 2008; Dennell, 2008; Ao et al., 2013a; Liu et al., 2021; Tu et al., 2022; Bae, 2024). The Majuangou site in the eastern part of the Nihewan Basin contains one of the earliest records of hominin presence in northern China, dating back to ca 1.66 Ma (Zhu et al., 2004). This timeframe is approximately the same age as that of the oldest fossil *Homo erectus* cranium of ca. 1.63 Ma, discovered at Gongwangling, north of the Qinling Mountains (Zhu et al., 2015). However, the earliest cultural deposits in China are found at Xihoudu site which is radio-isotopically dated to 2.43 Ma (Shen et al., 2020).

Based on their palaeoclimate reconstructions, Moghazi et al. (2024b) suggested that the climate patterns of the Nihewan Basin, driven by variations in both the East Asian summer (EASM) and winter monsoon (EAWM) closely align with those observed in the Chinese Loess Plateau (CLP) records in response to global glacial/interglacial cyclicity throughout the Early Pleistocene. This situates the Nihewan sedimentary sequence in a regional context as a climatically sensitive terrestrial archive, comparable to the loess-palaeosol sequences of the CLP and deep-sea sediments for reconstructing Quaternary climate change. These observations collectively highlight the palaeoanthropological and palaeoclimatic significance of the high-resolution sediment record from the Nihewan Basin in E Asia.

Based on the few published $\delta^{18}O_{enamel}$ and $\delta^{13}C_{enamel}$ records of Pleistocene mammalian tooth enamel (Xu et al., 2021, 2023), the environment in the Nihewan Basin underwent a marked transition from wet, closed landscapes dominated by C_3 vegetation before 1.2 Ma to drier, open landscapes with mixed C_3/C_4 vegetation between 1.2 and 1.1 Ma. Moreover, the pollen record shows that the climate of the basin shifted from cold-wet forest to cold-dry grassland during 1.337-1.324 Ma. This was followed by warm, wet conditions with sparse forest cover from 1.324 -1.317 Ma, then warm and humid climate during 1.317-1.312 Ma with forest-dominated environment, and eventually a return to cold, dry grassland from 1.312-1.290 Ma (Yang et al., 2022). Whilst previous efforts have been made, longer-term continuous stable isotope records directly retrieved from strata in the Nihewan Basin and covering the long span of ca. 1.3 millions of years of arguably prominent or sporadic hominin occupations in the basin between ca.1.66-0.4 Ma (Zhu et al., 2004; Deng et al., 2008; Dennell, 2013; Pei et al., 2019) are still lacking.

The $\delta^{18}O_{ost}$ and $\delta^{13}C_{ost}$ of carbonate valves of ostracods (small aquatic crustaceans) have been successfully used to reconstruct palaeoclimatic conditions in continental settings (Holmes and Chivas, 2002). Their $\delta^{18}O$ values are used to characterize the hydrology of the host waterbody, regional temperature and evaporation and precipitation changes, water sources, and meltwater or groundwater inflow (Schwalb, 2003). In contrast, atmospheric pCO_2 concentration, primary productivity, modes of organic matter decay, and photosynthetic activity of aquatic plants are recorded in their $\delta^{13}C$ values (Schwalb et al., 2013). Thus, the $\delta^{18}O_{ost}$ and $\delta^{13}C_{ost}$ records from sedimentary sequences in the Nihewan Basin can be a useful tracer for hydrological, temperature and vegetation changes during the Early Pleistocene.

In this study, we present the first long-term $\delta^{13}C_{ost}$ and $\delta^{18}O_{ost}$ records from the 86.2-m composite NH-T section at the northeastern part of the basin, spanning ca. 1.67 to 0.78 Ma. This isotope record is integrated with our previously published grain-size endmember (EM) dataset (Moghazi et al., 2024b) to reconstruct the hydrological conditions in the Nihewan Basin during the Early Pleistocene. Together with the artefactual record syntheses, we attempt to explore the link between the basin's local hydrology and the Early Pleistocene hominin activities.

4.3 Geological setting and modern climate

The Nihewan Basin is a Late Cenozoic fault-controlled basin situated at the northeastern margin of the CLP, within the Inner Mongolia Plateau and the N China Plain, ca. 150 km NW of Beijing at 40° N and 114° E (Fig. 27.4). The basin's formation is linked to the extensional tectonics of the Fen-Wei Graben, due to the northward movement of the Indian subcontinent colliding with the Eurasian plate during the Cenozoic era (Sun, 2005). The basin is characterized by a large valley, ca. 80 km long and 15-20 km wide, with an average elevation of ca. 1000 m. It is surrounded by the Xiong'er Mountain to the N, the Liuleng Mountains to the S, the Fenghuang Mountains to the E and the Guancen Mountain to the SW. The basin encompasses the ENE-striking Datong, Yangyuan, and Yuxian sub-basins.

The "Nihewan Beds" (Barbour, 1924) are up to 700-m thick lacustrine, fluvial, and windblown deposits (Zhou et al., 1991). This sedimentary succession dates back from the Early Pliocene ca. 4.2 Ma to the middle Pleistocene ca. 300 ka based on the palaeomagnetic (Deng et al., 2008; Bi et al., 2022) and luminescence (Nian et al., 2014; Han et al., 2016) dating. The Nihewan Formation (Min and Chi, 2003) in the lower part of the "Nihewan Beds" represents the type section of the Early Pleistocene in northern China (Young, 1950). The exposed sediment sections are primarily distributed along the SW-NE trending Sanggan River (Sangkan Ho) and SE-NW trending Huliu River on the Cenjiawan Platform (Barbour et al., 1926) near the northeastern margin of the Nihewan Basin. The Sanggan River, the largest river in the basin, flows from west to east through the Datong and Yangyuan sub-basins whilst its major tributary, the Huliu River, runs through the Yuxian sub-basin.

The Nihewan Basin experiences EAM climate and lies between the temperate semi-humid and semi-arid zones. Winters are cold and long, controlled by the cold Mongolian High, whilst summers are warmer and more humid due to the Pacific High. Based on dataset from the Shijiazhuang meteorological station (1985-2003), ca. 235 km S of the Nihewan Basin, the mean January, July and annual air temperatures are ca. -2, 28 and 14 °C, respectively. Additionally, the mean annual precipitation (MAP) is 542 mm, with the majority falling during the summer months_(Global Network for Isotopes in Precipitation (GNIP) database: https://nucleus.iaea.org/wiser). Located on the edge of the EASM influence, the basin represents a mixed zone of C_3 and C_4 plants. Its vegetation varies from warm-temperate deciduous broadleaved forests to semi-arid and arid grasslands (Mu et al., 2015).

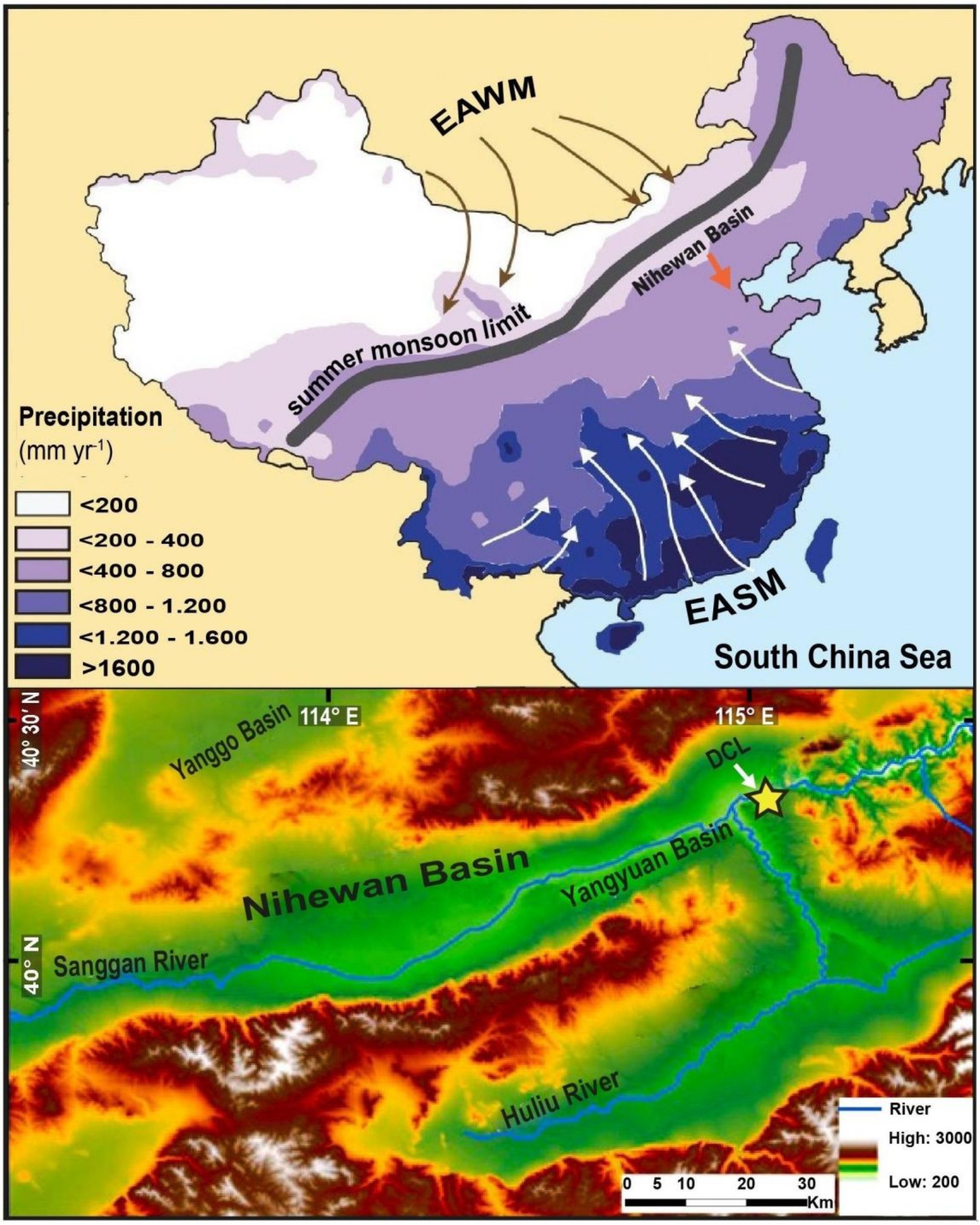

Figure 28.4 *Upper panel: mean precipitation distribution in China during 1980-2010 (modified after Blazina et al., 2014). Grey thick line = East Asian summer monsoon (EASM) limit. White arrows = EASM flow; Dark arrows = East Asian Winter Monsoon (EAWM); orange arrow = Position of Nihewan Basin. Lower panel: Nihewan Basin topography. Yellow star = Dachangliang (DCL) study site*

4.4 Materials and Methods

4.4.1 Stable isotope analysis

Material for this study derived from the 86.2-m thick composite NH-T section which resulted from the correlation of three newly exposed individual sediment sections (T1-T3) on the Dachangliang ridge (Fig. 27.4; Moghazi et al., 2024a). The NH-T section has been assigned an astronomically-tuned age range slightly revised in this study to ca. 1.67-0.78 Ma (Moghazi et al., 2024b). Stable O and C isotopes of ostracod calcite were analyzed for adult valves from a total of 90 samples selected throughout the NH-T section. Due to the absence of a single well-preserved and sufficiently abundant ostracod taxon over the whole sedimentary sequence, isotope measurements were continuously conducted on valves of mixed species assemblages (typically 10-15 valves per sample). These taxa include *Limnocythere flexa*, *Leucocythere* sp. (n = 43 samples) and *Ilyocypris* sp. (n = 41 samples). In the prominent white marl beds where other taxa were absent, valves of *Cytherissa lacustris* (n=6 samples) were exclusively used (Moghazi et al., 2024a). Valves with adhering sand grains and organic matter clumps were cleaned in 1% H_2O_2 with the aid of a fine brush under a stereomicroscope. Following the removal of H_2O_2 with a pipette, the valves were rinsed with ethanol and dried. Stable isotopes of the prepared samples were then measured at the Deutsches GeoForschungszentrum Potsdam (GFZ) using a MAT 253 ThermoFisher Scientific isotope ratio mass spectrometer coupled with an automated Carbonate Kiel IV device. During this process, the carbonate was reacted with 103% phosphoric acid (H_3PO_4) at 70°C to release CO_2. The ratios of $^{18}O/^{16}O$ and $^{13}C/^{12}C$ of the valves were expressed in permille (‰) relative to the VPDB standard, with a $\delta^{18}O$ value of -2.20‰ and a $\delta^{13}C$ value of 1.95‰ assigned to the NBS19 standard, ensuring comparability with published datasets. The analytical precision for the $\delta^{18}O$ and $\delta^{13}C$ values is <0.07‰.

4.4.2 Correction of stable isotopes for vital offsets

It was shown that the biogenic calcite of benthic ostracod valves does not precipitate in isotopic equilibrium with the host water (von Grafenstein et al., 2000). Stable isotope values for different species may have distinct systematic offsets from the values of abiotic, fine-grained bulk carbonate that precipitated under the same conditions due to so-called vital effects (i.e., biological/metabolic processes; Holmes and Chivas, 2002). To calculate the isotopic composition of abiotic calcite $\delta^{18}O_{eq.cal}$ and $\delta^{13}C_{eq.cal}$ which precipitated from host water in isotopic equilibrium, the measured $\delta^{18}O_{ost}$ and $\delta^{13}C_{ost}$ values can be reliably corrected by known species-specific vital offsets (von Grafenstein et al., 1999). Accordingly, the stable isotope data for *Limnocythere flexa* and *Leucocythere* sp. were corrected based on published offsets for *Limnocythere inopinata* because vital offsets seem to be constant for individual genera or even families. The previously reported vital offsets for *L. inopinata* are 0.78‰ for $\delta^{18}O_{ost}$ and -1.18‰ for $\delta^{13}C_{ost}$ values (von Grafenstein et al., 1999). *Cytherissa lacustris* shows species-specific offsets of 1.49‰ for $\delta^{18}O_{ost}$ and -0.13‰ for $\delta^{13}C_{ost}$ values, and vital offsets of 0.32‰ for $\delta^{18}O_{ost}$ and 3.03‰ for $\delta^{13}C_{ost}$ values were determined for *Ilyocypris* sp., as calculated from the average difference between the measured $\delta^{13}C_{ost}$ and $\delta^{18}O_{ost}$ values of *Eucypris mareotica* and *Ilyocypris sebeiensis* (Mischke et al., 2008). For most parts of the NH-T section, the vital offset of the dominant species was used. However, in stratigraphic intervals of the NH-T section where multiple species are dominantly present in roughly equal proportions, composite offsets were calculated. The calculation of these composite offsets was based on the average weighing related to the number of valves for each species. The combination of *C. lacustris* with *Ilyocypris* sp. resulted in an average correction of 0.59‰ for $\delta^{18}O_{ost}$ and -1.58‰ for $\delta^{13}C_{ost}$, whilst *L. flexa* combined with *Ilyocypris* sp. led to adjustments of 0.23‰ for $\delta^{18}O_{ost}$ and -2.11‰ for $\delta^{13}C_{ost}$ values.

4.5 Results

4.5.1 $\delta^{18}O_{ost}$ and $\delta^{13}C_{ost}$ data

The raw $\delta^{18}O_{ost}$ values of the analyzed four ostracod species in the NH-T sediment section range from -11.0 to -0.6 ‰ (VPDB) with an average of -3.9 ‰ (n = 93). The raw $\delta^{13}C_{ost}$ values vary between -8.5 and 1.3 ‰ (VPDB) with an average of -2.3 ‰ (n = 93) (Fig. 28.4). The $\delta^{18}O_{ost}$ and $\delta^{13}C_{ost}$ data show a covariance with a regression coefficient (*r*) value of 0.7 (Fig. 29.4).

In the lower part of NH-T section at 0.0-15.5 m, the wetland-lake interval defined by Moghazi et al. (2024a) shows average $\delta^{18}O_{eq.cal}$ and $\delta^{13}C_{eq.cal}$ values of -3.8 and -2.6 ‰, respectively (Fig. 28.4). In the overlying wetland interval at 15.5-30.4 m, the average $\delta^{18}O_{eq.cal}$ and $\delta^{13}C_{eq.cal}$ values are -5.6 and -4.7 ‰, respectively.

Higher up, the wetland-alluvial plain interval at 30.4-39.3 m, shows average $\delta^{18}O_{eq.cal}$ and $\delta^{13}C_{eq.cal}$ values of -4.2 and -3.1 ‰, respectively. The subsequent wetland-lake interval at 39.3-55.8 m, is characterized by average $\delta^{18}O_{eq.cal}$ and $\delta^{13}C_{eq.cal}$ values of -3.9 and -1.2 ‰. In the wetland-alluvial plain interval at 55.8-74.0 m, the average $\delta^{18}O_{eq.cal}$ and $\delta^{13}C_{eq.cal}$ values are -4.8 and -4.1 ‰, respectively. Eventually, the uppermost wetland-lake interval at 74.0-86.2 m, contains samples with average $\delta^{18}O_{eq.cal}$ and $\delta^{13}C_{eq.cal}$ values of -3.3 and -2.9 ‰, respectively.

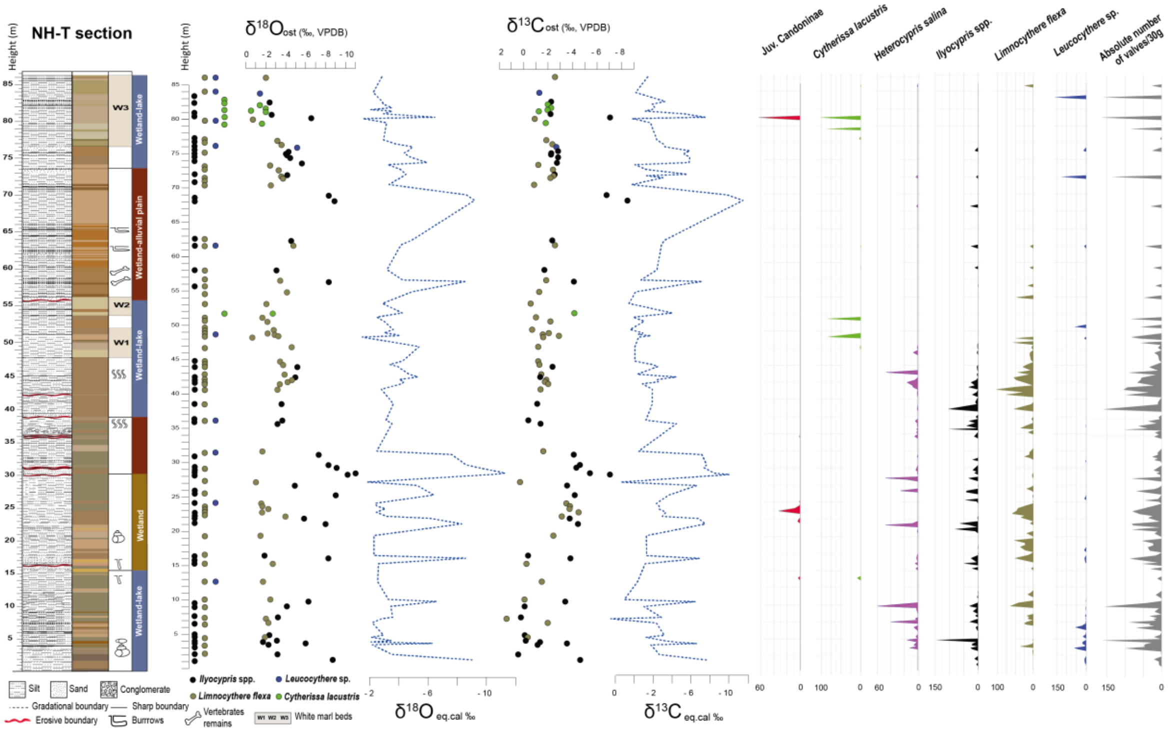

Figure 29.4 *Stratigraphy of the sediment section NH-T, showing lithology, colour, positions of white marker layers (W1-W3), depositional settings (after Moghazi et al., 2024a), stratigraphic positions of ostracod valves used for stable isotope analysis ($\delta^{18}O_{ost}$ and $\delta^{13}C_{ost}$), the vital offset corrected $\delta^{18}O_{eq.cal}$ and $\delta^{13}C_{eq.cal}$ data, and the absolute abundance of ostracod valves per 30 g of sediment*

4.6 Discussion

4.6.1 Interpretation of the $\delta^{18}O_{ost}$ and $\delta^{13}C_{ost}$ records

The high covariance between $\delta^{18}O_{ost}$ and $\delta^{13}C_{ost}$ signals with *r* value of 0.7 in the NH-T sediment section clearly suggests that the Early Pleistocene Nihewan Basin had hydrological characteristics similar to those typically observed in closed basin settings (Talbot, 1990). The overall range of $\delta^{18}O_{eq.cal}$ values is from -11.3 to -1.5 ‰ (average -4.3 ‰), whilst $\delta^{13}C_{eq.cal}$ values range from -11.5 to 2.5 ‰ (average -3 ‰). If the equation of Kim and O'Neil (1997) with the determined range of $\delta^{18}O_{eq.cal}$ values from the NH-T section for the formed carbonate and an assumed $\delta^{18}O$ value of -8 ‰ (SMOW) for the host water ($\delta^{18}O$ value of modern precipitation at the Shijiazhuang meteorological station) is solved for the water temperature, unrealistically low values mostly below 0 °C with an average of -1.7 °C are inferred. Ostracod valves must have formed at higher water temperatures. In modern lakes on the southern Tibetan Plateau, living ostracods were abundant in waters of 12-13.8 °C but not in colder waters (Börner et al., 2017). In addition, significantly higher air temperatures were inferred from Early Pleistocene pollen records of the Nihewan Basin.

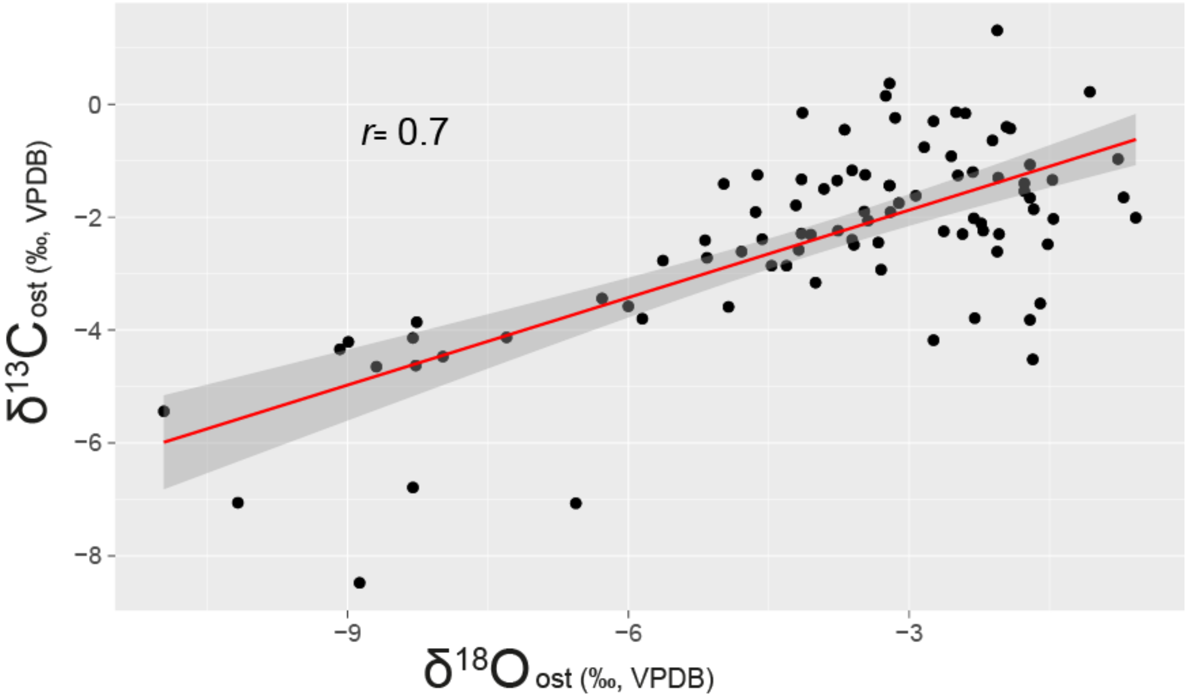

Figure 30.4 *Cross plot of the $\delta^{18}O_{ost}$ and $\delta^{13}C_{ost}$ data and correlation coefficient (r)*

Zhang et al. (2020) reconstructed average air temperatures of < 6 °C during cold periods and > 8 °C during warm periods. Therefore, temperature was apparently not the main controlling parameter which resulted in the determined $\delta^{18}O_{eq.cal}$ values for the NH-T section. Thus, the relatively large range of the $\delta^{18}O_{eq.cal}$ values (9.8 ‰ for the total range), the overall correlation of the $\delta^{18}O_{ost}$ and $\delta^{13}C_{ost}$ values, and also the low ostracod diversity of the NH-T section in comparison to modern freshwater lakes in the region (Zhai et al., 2011) suggest that water in the Early Pleistocene Nihewan Basin was mainly controlled by the precipitation/evaporation ratio or changing effective moisture similar to typical closed-basin lakes. This inference is supported by sedimentological and geochemical analyses of Li et al. (2000) who suggested that the Nihewan paleolake was "weak-saline" to "semi-saline". Additionally, the stratigraphic intervals of the NH-T section with the higher $\delta^{18}O_{ost}$ values at ca. 7 and 27 m are characterized by the dominant occurrence of *Heterocypris salina*. *Heterocypris salina* typically lives in small and marginally saline inland and coastal waters and was documented to form large populations in saline sulfurous springs (Fig. 28.4; Meisch, 2000). Although the water temperature apparently played a minor role, higher air temperatures typically cause stronger evaporation, and thus, higher $\delta^{18}O_{water}$ values of water and ostracod valves (Henderson and Holmes, 2009). Thus, we relate these $\delta^{18}O_{eq.cal}$ variations observed within the wetland-lake, wetland and wetland-alluvial plain intervals to the different $\delta^{18}O_{water}$ values of host waters (including lake and river waters) in the study area during the Early Pleistocene. Fan et al. (2014) reported that the modern $\delta^{18}O_{water}$ values of lake water in the Qarhan Salt Lake, Qaidam Basin, range between -8.5 and -4.9 ‰ (average -6.7 ‰) which are significantly higher than those of the river waters (including Golmud River and Nuomuhong River) flowing to Qarhan Lake, ranging from -11.8 to -8.8 ‰

(average -10.3 ‰). Fan et al. (2014) suggested that the higher $\delta^{18}O_{water}$ values of the lake water resulted from strong evaporation processes. Comparable isotopic variations have been also reported in the spring, river, and lake waters of the Lake Hulun Basin, Inner Mongolia (Han et al., 2019). According to their study, the average $\delta^{18}O_{water}$ values for spring, river, and lake waters recorded during 2017 were -11.9, -10.4, and -7.3 ‰, respectively. Drawing on these modern regional isotopic data as an analogous framework, the lowest and moderately higher average $\delta^{18}O_{eq.cal}$ values observed in the wetland and wetland-alluvial plain intervals probably correspond to waterbodies with minimal evaporative influence, potentially mirroring the stable isotopic signatures of spring and river waters, respectively. Conversely, the highest $\delta^{18}O_{eq.cal}$ values observed in wetland-lake intervals may reflect waterbody subjected to intense evaporation, analogous to lake waters. However, the effects of aridity and evaporation on the modern saline Qarhan Lake in the hyper-arid Qaidam Basin and in the higher latitude Lake Hulun Basin probably exceed those that affected the waterbodies of the Early Pleistocene Nihewan Basin.

To conclude, the Early Pleistocene Nihewan Basin was apparently a hydrologically closed basin, where prolonged water-residence time facilitated evaporative ^{18}O enrichment (Li and Ku, 1997; Paprocka, 2007). Consequently, the $\delta^{18}O_{eq.cal}$ variability reflects the amount of precipitation relative to the evaporation (i.e., the P/E ratio) or effective moisture and air humidity changes, and the more open (open wetland, alluvial plain) or closed (in-stream wetland, lake) nature of the waterbody at the section location (Gasse et al., 1996). Considering the variations in depositional facies reconstructed in the NH-T section in which the evaporation appears to be the dominant control, lower $\delta^{18}O_{eq.cal}$ values in the flowing stream/river waters probably resulted from drier conditions, whilst higher $\delta^{18}O_{eq.cal}$ values in more standing lake and wetland waters resulted from wetter conditions (Fig. 30.4).

In a closed basin, $\delta^{13}C_{ost}$ values track the regional hydrological balance and are mainly influenced by the $\delta^{13}C$ values of dissolved inorganic carbon (DIC) in the water column (Leng and Marshall, 2004). Enhanced pCO_2 exchange between atmosphere and DIC under warm/humid conditions reduces pCO_2 dissolution, increasing $\delta^{13}C_{DIC}$ values (Leng and Marshall, 2004). Additionally, aquatic vegetation preferentially incorporates ^{12}C during photosynthesis, further enriching DIC in ^{13}C (Liu et al., 2015). However, interpreting $\delta^{13}C_{ost}$ values is complex due to the dominant influence of $\delta^{13}C_{DIC}$ and small-scale spatial heterogeneities in the ostracod's ambient water, driven by algal and aquatic plant growth and organic matter degradation (Decrouy et al., 2011). The $\delta^{13}C_{DIC}$ values may be also controlled by the inorganic input of carbon into the waterbody. Thus, $\delta^{13}C_{eq.cal}$ data can only be indirectly used for the inference of biological activities including photosynthetic productivity, and temperatures (Zanchetta et al., 2007). Higher $\delta^{13}C_{eq.cal}$ values in the NH-T section probably indicate increased biogenic productivity, driven by higher air temperatures, and/or enhanced evaporation effects in more standing lake or wetland waters, indicating wetter conditions (Fig. 30.4). Conversely, lower values suggest reduced biogenic productivity in the flowing stream/river waters, reflecting drier conditions (Fig. 30.4).

By combining these new $\delta^{18}O_{eq.cal}$ and $\delta^{13}C_{eq.cal}$ records with the reconstructed EAM climate changes between warm, humid interglacials, and cold, dry glacials based on the grain-size end-member (EM) dataset of the same NH-T section (Fig. 30.4, Fig. 31.4; Moghazi et al., 2024b), we provide a detailed picture of the hydrological changes during ca. 1.67-0.78 Ma.

4.6.1 Evolution between 1.67 to 1.30 Ma, the pre-MPT period

The depositional facies at the NH-T section represent six cycles of changing hydrodynamic conditions from 1) wetland-lake (ca. 1.67-1.52 Ma), 2) wetland (ca. 1.52-1.38 Ma), 3) wetland-alluvial plain (ca. 1.38-1.30 Ma), 4) wetland-lake (ca. 1.30-1.08 Ma), 5) wetland-alluvial plain (ca. 1.08-0.90 Ma), to 6) wetland-lake conditions (ca. 0.90-0.78 Ma) (Fig. 31.4; Moghazi et al., 2024a).

Wetland-lake interval (ca. 1.67-1.52 Ma)

In this interval, the $\delta^{18}O_{eq.cal}$ and $\delta^{13}C_{eq.cal}$ values are covariant with *r* value = 0.5. High $\delta^{18}O_{eq.cal}$ and moderately high $\delta^{13}C_{eq.cal}$ values dominate, punctuated by occasional excursions of moderately low to low values relative to the overall average and standard deviation ($\delta^{18}O_{eq.cal}$ -4.3 ± 2.15 ‰, and $\delta^{13}C_{eq.cal}$ -3.0 ± 2.9 ‰). In contrast to the highly variable $\delta^{18}O_{eq.cal}$ values, $\delta^{13}C_{eq.cal}$ values show gradually increasing trend (Fig. 31.4). The dominance of high or moderately high values indicates that wetter conditions with more standing waters, higher evaporation effects and increased biogenic productivity prevailed. The EM data support the interpretation of the stable isotope data, indicating an intensified EASM, with apparently increased regional precipitation and elevated water level. Following the cycle-by-cycle correlation between the chronology of loess-paleosol record on CLP and the higher-resolution EM record of NH-T section and additional orbital tuning to astronomical solution (Fig. 31.4; Moghazi et al., 2024b; Laskar et al., 2004), this wetland-lake interval corresponds to the paleosols S_{23}-S_{21} and loess L_{23}-L_{22} deposits.

Wetland interval (ca. 1.52-1.38 Ma)

The covariance of $\delta^{18}O_{eq.cal}$ and $\delta^{13}C_{eq.cal}$ strengthens in this interval with *r* value = 0.8. The $\delta^{18}O_{eq.cal}$ values remain highly variable, while $\delta^{13}C_{eq.cal}$ values show an overall decrease trend towards the top of the interval (Fig. 31.4). The fluctuations between low and high $\delta^{18}O_{eq.cal}$ and $\delta^{13}C_{eq.cal}$ values indicate changes in the hydrological state, shifting back and forth between flowing and standing waters in contrast to the earlier wetland-lake interval when standing waters prevailed most of the time. $\delta^{18}O_{eq.cal}$ and $\delta^{13}C_{eq.cal}$ minima are lower than observed in the earlier wetland-lake interval, suggesting drier conditions and more open water with reduced evaporation effects and reduced biogenic productivity, especially near the top of the interval. This is consistent with EM data that show mixing EAM conditions with the slight dominance of EAWM conditions. This interval synchronously occurred with the L_{21}-L_{18} and S_{20}-S_{18} periods on CLP.

Wetland-alluvial plain interval (ca 1.38-1.30 Ma)

The $\delta^{18}O_{eq.cal}$ and $\delta^{13}C_{eq.cal}$ values in this interval maintain a strong covariance of *r* value = 0.8. The dominating high $\delta^{18}O_{eq.cal}$ and moderately high $\delta^{13}C_{eq.cal}$ values, along with the gradually increasing $\delta^{13}C_{eq.cal}$ trend, indicate a return to a more stagnant setting and higher water-residence time probably due to intensified wetter climatic conditions accompanied by increased biogenic productivity. EM data confirm the stronger influence of the EASM but indicate also locally increased input of terrestrial materials (Fig. 31.4). Based on the dominance of the high $\delta^{18}O_{eq.cal}$ values in this interval which probably result from strong effects of evaporative enrichment, sediments likely accumulated in an in-stream wetland with dense vegetation (Mischke et al., 2021) and slow water flow. The reconstructed in-stream wetland was apparently more strongly affected by evaporation than the open-basin wetland inferred for the sediments below in the NH-T section (Moghazi et al., 2024a). The timeframe of this interval corresponds to the S_{17}-S_{16} and L_{17} periods on CLP.

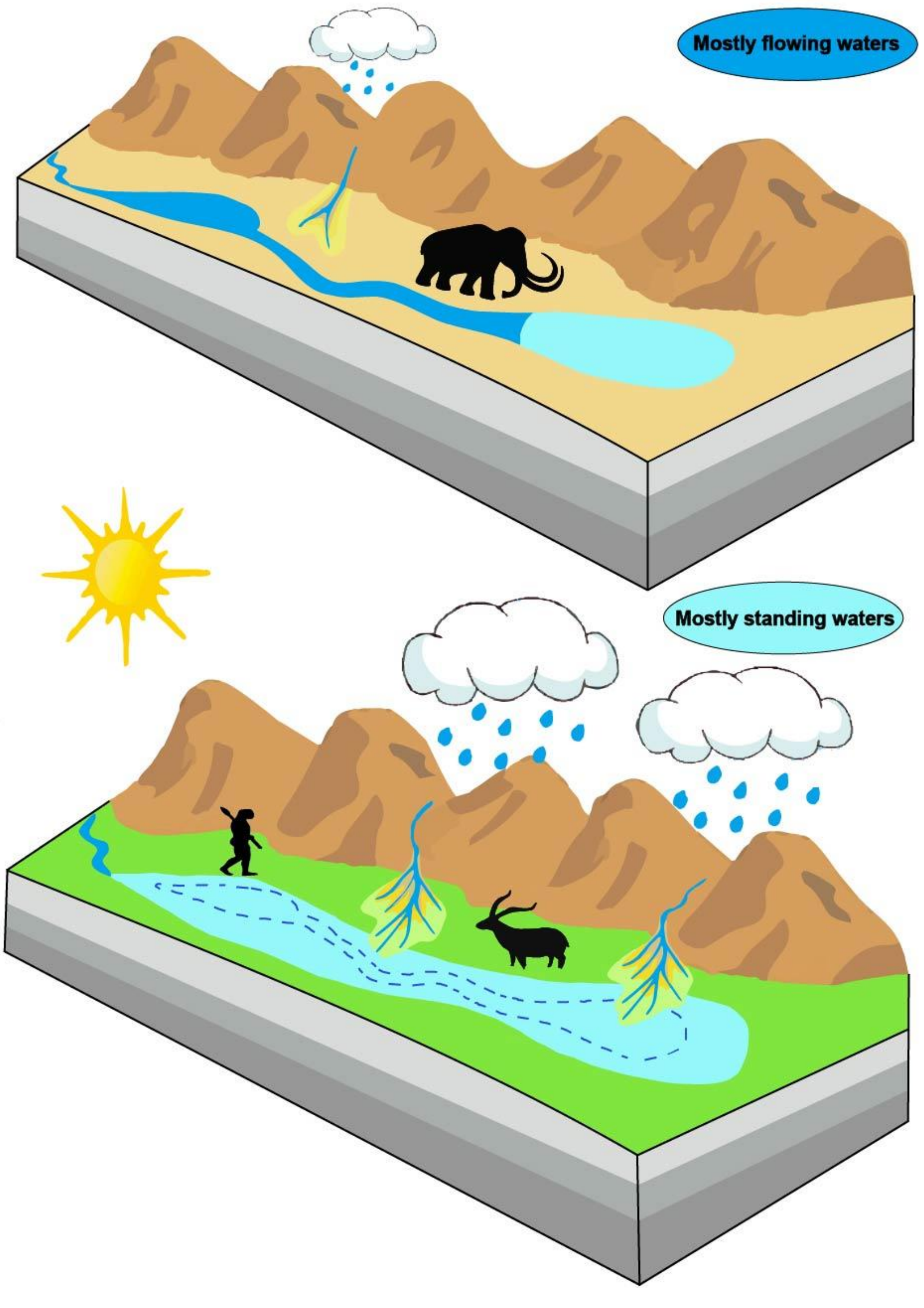

Figure 31.4 *Schematic model showing the hydrological state shifts between standing and flowing waters in the Early Pleistocene Nihewan Basin*

4.6.2 Evolution between 1.67 to 1.30 Ma, the pre-MPT period

Wetland-lake interval (ca. 1.30-1.08 Ma)

The $\delta^{18}O_{eq.cal}$ and $\delta^{13}C_{eq.cal}$ values here are not correlated (*r* value = 0.1). However, the dominance of moderately high $\delta^{18}O_{eq.cal}$ values in this interval indicates a high water-residence time, resulting in strong evaporative effects. More standing rather than flowing waters at the NH-T section location reflect dominantly wetter climate conditions. The concurrently moderately high to high $\delta^{13}C_{eq.cal}$ values suggest relatively increased biogenic productivity in comparison to the wetland-lake interval at the section's base. Although a strong $\delta^{18}O$-$\delta^{13}C$ covariance typically indicates a hydrologically-closed lake (Talbot, 1990), a low or absent covariance in such closed systems may either imply a stabilized lake level or a period of elevated pCO_2 (Li and Ku, 1997). We favor the interpretation of exceptionally higher pCO_2 concentrations in this interval as the absent covariance is accompanied by higher $\delta^{13}C_{eq.cal}$ values, especially at the top of the interval. The EM data support the interpretation of the stable isotope data because they indicate a transition from the dominance of EAWM conditions in the lower part to the dominance of EASM conditions in the middle and upper part of this interval (Moghazi et al., 2024b). The wetland-lake interval corresponds to the timeframe of L_{15}-L_{13} and S_{14}-S_{12} deposits on CLP.

Wetland-alluvial plain interval (ca. 1.08-0.90 Ma)

The $\delta^{18}O_{eq.cal}$ and $\delta^{13}C_{eq.cal}$ values of this interval are strongly positively correlated with *r* value = 0.8. The fluctuations between low and moderately high $\delta^{18}O_{eq.cal}$ and low and high $\delta^{13}C_{eq.cal}$ values suggest hydrological state changes between flowing and standing waters, probably reflecting high climate variability. The $\delta^{18}O_{eq.cal}$ and $\delta^{13}C_{eq.cal}$ minima and maxima are less extreme compared to the large stable isotope shifts observed in the wetland interval (ca. 1.52-1.38 Ma), suggesting shorter water residence times and weaker evaporative effects (Fig. 31.4). Also, relatively large oscillations of the EMs suggest fluctuating EAWM and EASM conditions. This interval aligns with the L_{12}-$L_{9\text{-}2}$ and S_{11}-S_9 periods on CLP (Fig. 31.4).

Wetland-lake interval (ca. 0.90-0.78 Ma)

The $\delta^{18}O_{eq.cal}$ and $\delta^{13}C_{eq.cal}$ values here are covariant again with *r* value = 0.7. Moderately high to high $\delta^{18}O_{eq.cal}$ and $\delta^{13}C_{eq.cal}$ values predominate this interval, reflecting the dominance of standing waters as a result of wetter climate with intensified monsoonal precipitation, enhanced evaporation effects, and elevated biogenic productivity. The EM data agree with this interpretation indicating prevailing EASM conditions for the middle and upper part of the interval. This uppermost wetland-lake interval correlates to the $L_{9\text{-}1}$ and S_8-S_7 periods on CLP (Fig. 31.4).

4.6.3 The NH-T stable isotope record and regional climate change

To assess whether the stable isotope variations recorded in the NH-T section reflect basin-specific hydrological dynamics or include regional climate signal, we here compare these variations with established marine and terrestrial palaeoclimatic records from the South China Sea (SCS) and CLP.

Qian et al. (2024) suggested that the change in the marine-land temperature gradients (ΔT) possibly affected the hydroclimate in East Asia. They observed shifts in the East Asia hydroclimate from overall dry to wet conditions together with increased ΔT. Interestingly, we also noticed that the $\delta^{18}O_{eq.cal}$ variations apparently track similar patterns of change in ΔT which might be indicative of the available moisture transported to the land. This ΔT typically fuels the EASM circulation. ΔT is calculated here from the difference between sea surface temperature (SST) at the Ocean Drilling Program (ODP) site 1146 in the SCS and land-surface temperature (LST) at the Lingtai section of CLP (Fig. 31.4; Clemens and Prell, 2003; Lu et al., 2022).

The concurrence of the $\delta^{18}O_{eq.cal}$ maximum at 12 m above the section's base with the EM-inferred strengthened EASM, the S_{22} interglacial on the CLP and a prominent increase in ΔT at ca. 1.55 Ma suggests that an EASM-driven precipitation increase led to a wetter climate in the monsoon region including Nihewan Basin. Moreover, Wang et al. (2004) reported a period of $\delta^{13}C$ maxima during 1.65-1.55 Ma at ODP site 1143 in the SCS, aligning with the dominance of higher $\delta^{18}O_{eq.cal}$ and gradually increasing $\delta^{13}C_{eq.cal}$ values in the wetland-lake interval (ca. 1.67-1.52 Ma) (Fig. 31.4). Similarly, Da et al. (2015) observed a brief increase in pCO_2 concentrations on CLP between ca. 1.6 and 1.5 Ma.

The highly variable $\delta^{18}O_{eq.cal}$ and gradually decreasing $\delta^{13}C_{eq.cal}$ values in the wetland interval from ca. 1.52-1.38 Ma align with the decrease in ΔT relative to the earlier wetland-lake interval (Fig. 31.4). Thus, a regional shift to colder and drier conditions is inferred. The three main $\delta^{18}O_{eq.cal}$ maxima of the interval correlate with the S_{20}-S_{18} periods, and the comparison with the variations in ΔT indicates S_{18} as the time of stronger EASM-driven precipitation in comparison to S_{20} and S_{19}.

A return to generally wetter conditions is reflected by high $\delta^{18}O_{eq.cal}$ and increasing $\delta^{13}C_{eq.cal}$ values in the in-stream wetland interval (ca 1.38-1.30 Ma), coinciding with a period of high ΔT. The $\delta^{18}O_{eq.cal}$ maxima aligned with S_{17} and S_{16} at 1.36 and 1.32 Ma match a strong and a moderate ΔT peak, respectively, supporting the inference of higher EASM-driven precipitation (Fig. 31.4).

The $\delta^{18}O_{eq.cal}$ minima and maxima in the following wetland-lake interval (ca. 1.30-1.08 Ma), corresponding to S_{14} and S_{13}, respectively, match with a similar pattern of variation in ΔT. This suggests the gradual intensification of EASM-driven precipitation, especially towards the top of the interval (Fig. 31.4).

The wetland-alluvial plain interval (ca. 1.08-0.90 Ma) aligns with a decreasing ΔT trend, reflecting reduced moisture transport to northern latitudes. The early stage of this interval was marked by an episode of increased $\delta^{18}O_{eq.cal}$ and $\delta^{13}C_{eq.cal}$ values. This episode coincides with a reported period of $\delta^{13}C$ maxima during 1.04-0.97 Ma at ODP site 1143 in the SCS (Fig. 31.4; Wang et al., 2004). Wang et al. (2004) noticed that the timing of the MPT with expansion of the ice sheets was following this period of inferred high CO_2 levels in the global ocean. We also noticed a following pronounced $\delta^{18}O_{eq.cal}$ minimum during the S_9 period correlates with a lower ΔT (Fig. 31.4). This feature probably resembles Weak Monsoon Intervals (WMIs) documented in speleothem records and attributed to ice-sheet dynamics in the Northern Hemisphere (Cheng et al., 2009; Ziegler et al., 2010).

The increasing $\delta^{18}O_{eq.cal}$ and $\delta^{13}C_{eq.cal}$ values of the uppermost wetland-lake interval (ca. 0.9-0.78 Ma) correspond to a rising ΔT, pointing to enhanced EASM-driven precipitation (Fig. 31.4). Moreover, a $\delta^{18}O_{eq.cal}$ maximum during the S_8 period corresponds with high ΔT. This inference is supported by a reported increase in pCO_2 on CLP (Yamamoto et al., 2022).

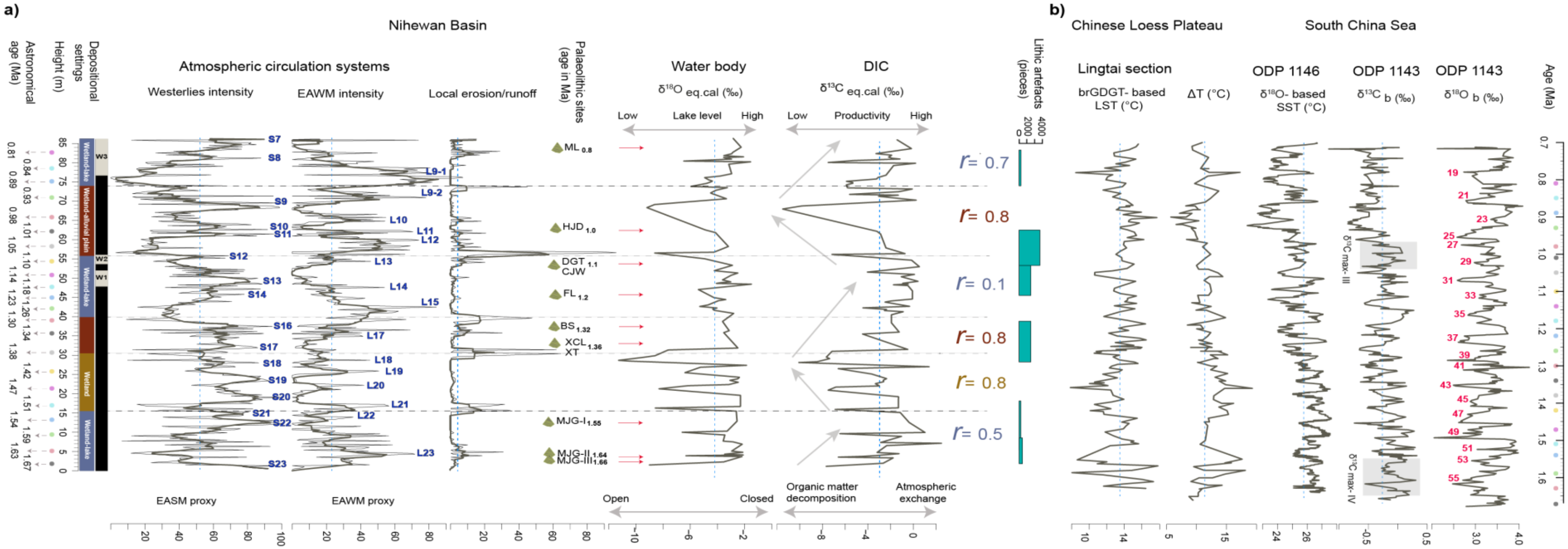

Figure 32.4 *a) Variation in the relative abundance of end members (EMs) 1, 3 and 4 as proxies for EASM, EAWM and local runoff with the revised astronomical age of NH-T section (Moghazi et al. 2024b). The correlated S (palaeosol) and L (loess) periods of CLP are marked in blue (Moghazi et al. 2024b). Dashed horizontal lines mark the boundaries of six cycles of changing hydrodynamic conditions (Moghazi et al. 2024a). The Palaeolithic sites in the Nihewan Basin are MJG-III = Majuangou III (Zhu et al., 2004), MJG-II = Majuangou II (Zhu et al., 2004), MJG-I = Majuangou I (Zhu et al., 2004), XT = Xiantai (Deng et al., 2006a, 2006b), XCL = Xiaochangliang (Zhu et al., 2001), BS = Banshan (Zhu et al., 2004), FL = Feiliang (Deng et al., 2007), DGT = Donggutuo (Wang et al., 2005), CJW = Cenjiawan (Xie and Cheng, 1990), HJD = Huojiadi (Liu et al., 2010), ML = Maliang (Wang et al., 2005). Red arrows mark the concurrence between the Palaeolithic sites and higher* $\delta^{18}O_{eq.cal}$ *and* $\delta^{13}C_{eq.cal}$ *values. b) GDGT-derived LST on the CLP (Lu et al., 2022), the difference in sea and terrestrial temperatures (ΔT),* $\delta^{18}O$*-derived SST record of ODP site 1146 on the SCS (Clemens and Prell, 2003), benthic* $\delta^{13}C_b$ *and* $\delta^{18}O_b$ *records of ODP site 1143 on the SCS (Tian et al., 2002, 2004; Wang et al., 2004, 2010). Grey boxes mark the intervals of two* $\delta^{13}C$ *maxima identified in the* $\delta^{18}O_b$ *record of ODP site 1143:* $\delta^{13}C_{max-III}$ *(1.04-0.97 Ma) and* $\delta^{13}C_{max-VI}$ *(1.65-1.55 Ma) (Wang et al., 2004)*

4.6.4 Relationship between Early Pleistocene hydrological changes and hominin occupation

Archaeological excavations in the Nihewan Basin have uncovered hominin-produced stone tools dating back from ca.1.66-0.4 Ma (Dennell, 2013). Throughout this timeframe, the basin sustained mixed grassland and woodland habitats (Ao et al. 2013a). However, the archaeological record is not continuous, showing significant gaps between 1.5-1.4 Ma, 1.3-1.2 Ma, 1.0-0.9 Ma, and 0.8-0.4 Ma (Yang et al., 2019). Sun et al. (2018) suggested that these hiatuses were probably due to the inhospitable climatic conditions in northern latitudes, in contrast to the more continuous record found in southern China.

The characteristics of the waterbodies in the northeastern part of the basin apparently changed from hydrologically closed systems during wetter conditions and accompanied by increased productivity in the wetland-lake interval ca. 1.67-1.52 Ma, shifting to mixed hydrological conditions when the climate became steadily drier in the wetland interval ca. 1.52-1.38 Ma. Then, a return to a hydrologically-closed system with wetter conditions and enhanced productivity occurred in an in-stream wetland (ca. 1.38-1.30 Ma). At the oldest well-dated site, Majuangou (1.66-1.32 Ma), the pollen assemblage shows two different phases: one with forest/woodland dominance and the other with open grassland dominance (Potts and Faith, 2015). This trend towards increasing aridity is further supported by findings from the Xiantai site (1.36 Ma), where pollen are dominated by *Artemisia* and Chenopodiaceae, indicating a grassland environment and that the climate gradually became drier (Deng et al., 2006). In contrast, a brief warm and wet interval is evidenced at the Banshan site (1.324-1.318 Ma), characterized by a predominating *Pinus* forest during the period of human activity (Yang et al., 2022). This implies that the shifts in our stable isotope data are corroborated by pollen data from these early sites in the basin.

The inferred habitats range from the open grasslands at Feiliang (1.2 Ma; Pei et al., 2017) to the more humid forest-grassland mosaic at Donggutuo (1.10 Ma; Pei et al., 2009). This inference aligns with our findings which indicate progressively wetter conditions and increased productivity during the wetland-lake interval ca. 1.30-1.08 Ma. In contrast, the stable isotope results of Xu et al. (2023) suggest an opposite pattern, shifting from a wet and closed pure C_3 vegetation prior to 1.2 Ma, to drier and more open C_3/C_4 mixed vegetation during 1.2-1.1 Ma.

Our stable isotope data reveal a high climate variability, alternating between wetter and drier climate conditions during the wetland-alluvial plain interval ca. 1.08-0.90 Ma. Between 1.1 and 1.0 Ma, the density of stone artefacts increased, and lithic technology became more advanced (Fig. 31.4; Yang et al., 2021). We therefore associate the increased toolmaking skills and technological innovations of hominins with the wetter climatic phases in the transition from the end of the wetland-lake interval ca. 1.30 to 1.08 Ma and the early stage of the wetland-alluvial plain interval ca. 1.08-0.9 Ma (Fig. 31.4). The archaeological gap between 1.0 and 0.90 Ma coincides with a pronounced drying trend inferred from our stable isotope data (Fig. 31.4; Yang et al., 2021). Following this gap, the stable isotope evidence indicates that wetter conditions with higher biogenic productivity prevailed during ca. 0.9-0.78 Ma. Corresponding to this wetter period, artefacts are reported from the Nihewan Basin again (Yang et al., 2021).

Our findings are broadly consistent with Dennell's (2013) suggestion that hominins likely occupied the basin during the warmer, favorable periods and avoided it under significantly colder ones (Fig. 30.4, Fig. 31.4).

4.7 Conclusions

- This study presents the first long-term stable isotope record of the Early Pleistocene Nihewan Basin.
- The strong covariance of $\delta^{18}O_{eq.cal}$ and $\delta^{13}C_{eq.cal}$ values implies that the Early Pleistocene Nihewan Basin was mostly hydrologically closed.
- The $\delta^{18}O_{eq.cal}$ and $\delta^{13}C_{eq.cal}$ data show that water bodies in the basin were strongly affected by evaporation.
- Thus, the $\delta^{18}O_{eq.cal}$ variability reflects the local hydrological state at the section location between closed (more standing waters, in-stream wetland, lake) and open (more flowing waters, open wetland, alluvial plain) settings instead of regional P/E ratios alone.
- The concurrence of high $\delta^{18}O_{eq.cal}$ and $\delta^{13}C_{eq.cal}$ values and the increase in ΔT is indicative of an increase in the proportion of EASM-driven precipitation which led to wetter climate and increased biogenic productivity, whereas low values reflect decreased EASM-driven precipitation and drier climate and reduced biogenic productivity.
- In comparison with the synthetic Early Pleistocene artefact record from the basin, inferred hominin occupation mostly coincided with periods of higher $\delta^{18}O_{eq.cal}$ and $\delta^{13}C_{eq.cal}$ values. Thus, hominins were more present during wetter climate periods when more standing waters bodies had formed in the Nihewan Basin.

5 Key conclusions and future work

This PhD study is the first to employ a holistic approach to investigate in detail the complex deposition history of the Early Pleistocene Nihewan sediments. The results of the study present new insights and evidence for the aeolian origin of these sediments and their ultimate accumulation in a dominantly wetland depositional setting. These findings challenge the long-existing claims in the literature that the depositional setting in the basin was mostly a lake. Furthermore, based on the newly established long-term stable isotope record, this study provides the first evidence for the hydrological closure of the Nihewan Basin during the Early Pleistocene. These collective findings refine our understanding of the favorable and challenging climatic conditions that strongly influenced the Early Pleistocene hominin activities in the region. Thus, this study paves the way for more research on the palaeoenvironments of Early Pleistocene hominins in E Asia.

Various approaches are suggested here for future work.

- The chronological constraints for Dachangliang sediment sections and nearby sections with long magnetostratigraphic polarity intervals (normal or reversed) can be improved in two ways: first, by applying $^{26}Al/^{10}Be$ burial dating method and second by enhancing the sampling resolution in intervals of strong grain-size EM fluctuations to enable fine-scale astronomical tuning of grain-size data.
- Although the eastern margin of the Nihewan Basin offers numerous exposed sediment sections, sediments from a more central location are scientifically preferable due to their likelihood of providing a more continuous climatic record which was formed at a relatively stable sediment accumulation rate. The primary challenge to study these central sediments is that their access requires drilling of sediment cores.
- Soil branched glycerol dialkyl glycerol tetraethers (brGDGTs) and plant leaf wax isotopes ($\delta^{13}C_{wax}$, $\delta^{2}H_{wax}$) preserved in the Early Pleistocene Nihewan sediments have the potential to provide independent records of air temperature and monsoonal precipitation. Such records are of great importance for improving our understanding of how these climate variables influenced hominin activities in the basin, and for refining climate-human coevolution models in semi-arid regions.
- The application of the novel ostracod-clumped isotope (Δ_{47}) thermometer to the long-sediment archives of the Nihewan Basin will also enable independent reconstruction of absolute paleotemperatures during periods of Early Pleistocene human presence. Integrated with conventional $\delta^{18}O_{ostracod}$ data, the combined dataset will further reconstruct the associated hydrological shift

References

Antoine, P., Rousseau, D., Moine, O., Kunesch, S., Hatté, C., Lang, A., Tissoux, H., Zöller, L. (2009). Rapid and cyclic aeolian deposition during the Last Glacial in European loess: a high-resolution record from Nussloch, Germany. Quat. Sci. Rev. 28, 2955-2973.

Ao, H., Dekkers, M., Deng, C., Zhu, R. (2009). Paleoclimatic significance of the Xiantai Fluvio-lacustrine sequence in the Nihewan Basin (North China), based on rock magnetic properties and clay mineralogy. Geophys. J. Int. 177, 913-924.

Ao, H., Deng, C., Dekkers, M., Liu, Q., Qin, L., Xiao, G., Chang, H. (2010). Astronomical dating of the Xiantai, Donggutuo and Maliang Paleolithic sites in the Nihewan Basin (North China) and implications for early human evolution in East Asia. Palaeogeogr. Palaeoclimatol. Palaeoecol. 297, 129-37.

Ao, H., An, Z., Dekkers, M., Wei, Q., Pei, S., Zhao, Hui, Zhao, Hongli, Xiao, G., Qiang, X., Wu, D., Chang, H. (2012). High-resolution record of geomagnetic excursions in the Matuyama chron constrains the ages of the Feiliang and Lanpo Paleolithic sites in the Nihewan Basin, North China. Geochem. Geophys. Geosyst. 13, Q08017.

Ao, H., Dekkers, M., An, Z., Xiao, G., Li, Y., Zhao, H., Qiang, X., Chang, H., Chang, Q., Wu, D. (2013a). Magnetostratigraphic evidence of a mid-Pliocene onset of the Nihewan Formation-implications for early fauna and hominid occupation in the Nihewan Basin, North China. Quat. Sci. Rev. 59, 30-42.

Ao, H., Dekkers, M., Qi, W., Qian, X., Xiao, G. (2013b). New evidence for early presence of hominids in North China. Sci. Rep. 3, 2403.

Ao, H., Rohling, E., Li, X., Song, Y., Roberts, A., Han, Y., Poulsen, C., Jonell, T., Liebrand, D., Sun, Q., Li, X., Qiang, X., Zhang, P., Dekkers, M. (2023). Northern hemisphere ice sheet expansion intensified Asian aridification and the winter monsoon across the Mid-Pleistocene transition. Commun. Earth Environ. 4, 1-11.

Arts, M. (2023). WaverideR: extracting signals from wavelet spectra.

Bae, C. (2024). The Paleoanthropology of Eastern Asia. University of Hawaii Press.

Bae, C., Manthey, C. (2025). Out of Africa I revisited: life history, energetics, and the evolutionary capacity for early hominin dispersals. Quat. Sci, Rev. 370, 109690.

Barbour, G. (1924). Preliminary observations in the Kalgan area. Bull. Geol. Soc. China 3, 153-68.

Barbour, G., Licent, E., Teilhard de Chardin, P. (1926). Geological study of the deposits of the Sangkanho basin. Bull. Geol. Soc. China 5, 263-278.

Bi, Y., Pang, E., Sun, Y., Liu, Y., Bian, Q., Liu, S., Shen, Z., Xiong, J., Zhang, H., Hao, Q., Deng, C. (2022). Magnetostratigraphy of the fluvio-lacustrine sequence of core DY-1 in the Datong Basin and its implications for the evolution of the Shanxi Rift System in northern China. Palaeogeogr. Palaeoclimatol. Palaeoecol. 599, 111063.

Blazina, T., Sun, Y., Voegelin, A., Lenz, M., Berg, M., Winkel, L. (2014). Terrestrial selenium distribution in China is potentially linked to monsoonal climate. Nat. Commun. 5, 4717.

Blott, S., Pye, K. (2001). GRADISTAT: a grain size distribution and statistics package for the analysis of unconsolidated sediments. Earth Surf. Process. Landforms 26, 1237-1248.

Börner, N., De Baere, B., Akita, L., Francois, R., Jochum, K., Frenzel, P., Zhu, L., Schwalb, A. (2017). Stable isotopes and trace elements in modern ostracod shells: implications for reconstructing past environments on the Tibetan Plateau, China. J. Paleolimnol. 58, 191-211.

Chen, M. (1988). Study on the Nihewan Beds. China Ocean Press, 143. (in Chinese)

Chen, X., Chi, Z., Dong, S., Yan, Z., Yang, J., Shi, W., Min, L., Wang, Y., Yao, P. (2015). Late Cenozoic sedimentation of Nihewan Basin, central North China and its tectonic significance. J. Asian Earth Sci. 114, 242-257.

Cheng, H., Edwards, R., Broecker, W.S., Denton, G., Kong, X., Wang, Y., Zhang, R., Wang, X. (2009). Ice age terminations. Science 326, 248-252.

Chi, Z., Wei, Q. (2013). Study of "Nihewan Layer". Stor. Relics 5, 3-10. (in Chinese)

Chinese Academy of Sciences (Compilatory Commission of Physical Geography of China), (1984). Physical Geography of China: Climate. Sci. Press 1-30. (in Chinese)

Clemens, S., Prell, W. (2003). Data report: oxygen and carbon isotopes from site 1146, northern South China Sea. In: Prell, W.L., Wang, P., Blum, P., Rea, D. and Clemens, S. (Eds.), Proc. Ocean Drill. Program Sci. Results 184, 1-8.

Da, J., Zhang, Y., Wang, H., Balsam, W., Ji, J. (2015). An Early Pleistocene atmospheric CO_2 record based on pedogenic carbonate from the Chinese loess deposits. Earth Planet. Sci. Lett. 426, 69-75.

Dai, C., Gao, S., Zhang, Y., Xia, F., Wang, D. (2023). A Paleo-Changjiang delta complex on the East China Sea shelf formed Some 30 ka Ago (at the MIS 3 Stage). J. Mar. Sci. Eng. 11, 2035.

Dearing, J. (1999). Magnetic susceptibility. In: Walden, J., Oldfield, F., Smith, J. (Eds.), Environmental Magnetism, a Practical Guide. Technical Guide No. 6. Quat. Res. Assoc. 35-62.

Decrouy, L., Vennemann, T., Ariztegui, D. (2011). Controls on ostracod valve geochemistry, Part 1: variations of environmental parameters in ostracod (micro-) habitats. Geochim. Cosmochim. Acta 75, 7364-7379.

Deng, C., Hao, Q., Guo, Z., Zhu, R. (2019). Quaternary integrative stratigraphy and timescale of China. Sci. China Earth Sci. 62, 324-348.

Deng, C., Shaw, J., Liu, Q., Pan, Y., Zhu, R. (2006a). Mineral magnetic variation of the Jingbian loess/paleosol sequence in the northern Loess Plateau of China: implications for Quaternary development of Asian aridification and cooling. Earth Planet. Sci. Lett. 241, 248-259.

Deng, C., Wei, Q., Zhu, R., Wang, H., Zhang, R., Ao, H., Chang, L., Pan, Y. (2006b). Magnetostratigraphic age of the Xiantai Paleolithic site in the Nihewan Basin and implications for early human colonization of northeast Asia. Earth Planet. Sci. Lett. 244, 336-348.

Deng, C., Xie, F., Liu, C., Ao, H., Pan, Y., Zhu, R. (2007). Magnetochronology of the Feiliang Paleolithic site in the Nihewan Basin and implications for early human adaptability to high northern latitudes in East Asia. Geophys. Res. Lett. 34, 1-6.

Deng, C., Zhu, R., Zhang, R., Ao, H., Pan, Y. (2008). Timing of the Nihewan formation and faunas. Quat. Res. 69, 77-90.

Deng, T., Zheng, M. (2005). Limb bones of *Elasmotherium* (Rhinocerotidae, Perissodactyla) from Nihewan (Hebei, China). Vert. PalAsiat. 43, 110-121. (in Chinese with English abstract)

Dennell, R. (2008). The Palaeolithic Settlement of Asia. Cambridge University Press.

Dennell, R. (2013). The Nihewan Basin of North China in the early Pleistocene: continuous and flourishing, or discontinuous, infrequent and ephemeral occupation? Quat. Int. 295, 223-236.

Dietze, E., Hartmann, K., Diekmann, B., IJmker, J., Lehmkuhl, F., Opitz, S., Stauch, G., Wünnemann, B., Borchers, A. (2012). An end-member algorithm for deciphering modern detrital processes from lake sediments of Lake Donggi Cona, NE Tibetan Plateau, China. Sediment. Geol. 243-244, 169-180.

Dietze, E., Dietze, M. (2019). Grain-size distribution unmixing using the R package EMMAgeo. Quat. Sci. J. 68, 29-46.

Ding, Z., Derbyshire, E., Yang, S., Yu, Z. W., Xiong, S., Liu, T. (2002). Stacked 2.6-Ma grain size record from the Chinese loess based on five sections and correlation with the deep-sea δ^{18}O record. Paleoceanography 17, 5-1-5-21.

Ding, Z., Derbyshire, E., Yang, S., Sun, J., Liu, T. (2005). Stepwise expansion of desert environment across northern China in the past 3.5 Ma and implications for monsoon evolution. Earth Planet. Sci. Lett. 237, 45-55.

Domro¨s, M., Peng, G. (1988). The Climate of China. Berlin/Heidelberg: Springer.

Eltijani, A., Molnár, D., Makó, L., Geiger, J., Sümegi, P. (2022). Application of parameterized grain-size endmember modeling in the study of Quaternary oxbow lake sedimentation: a case study of Tövises bed sediments in the Eastern Great Hungarian Plain. Quaternary 5, 44.

Fan, Q., Ma, H., Wei, H., Shan, F., An, F., Xu, L., Madsen, D. (2014). Late Pleistocene paleoclimatic history documented by an oxygen isotope record from carbonate sediments in Qarhan Salt Lake, NE Qinghai-Tibetan Plateau. J. Asian Earth Sci. 85, 202-209.

Folk, R. (1954). The distinction between grain size and mineral composition in sedimentary-rock nomenclature. J. Geol. 62, 344-359.

Folk, R., Ward W. (1957). Brazos River bar: a study in the significance of grain size parameters. J. Sediment. Petrology 27, 3-26.

Gammon, P., Neville, L., Patterson, R., Savard, M., Swindles, G. (2017). A log-normal spectral analysis of inorganic grain-size distributions from a Canadian boreal lake core: towards refining depositional process proxy data from high latitude lakes. Sedimentology 64, 609-630.

Gasse, F., Fontes, J., Van Campo, E., Wei, K. (1996). Holocene environmental changes in Bangong Co basin (Western Tibet). Palaeogeogr. Palaeoclimatol. Palaeoecol. 120, 79-92.

Grimm, E. (1987). CONISS: a FORTRAN 77 program for stratigraphically constrained cluster analysis by the method of incremental sum of squares. Comput. Geosci. 13, 13-35.

Guo, J., Ziegler, M., Wanders, N., Vreeken, M., Yin, Q., Lu, H., Fuchs, L., Dong, J., Sun, Y., Peterse, F. (2024). Robust land surface temperature record for North China over the past 21,000 years. Sci. Adv. 10, eadj4800.

Han, Z., Li, X., Wang, Y., Wang, X., Yi, S., Lu, H. (2016). Tectonically-controlled infilling of the eastern Nihewan Basin, North China, since the middle Pleistocene. Sci. China Earth Sci. 59, 1378-1389.

Han, Z., Shi, X., Jia, K., Sun, B., Zhao, S., Fu, C. (2019). Determining the discharge and recharge relationships between lake and groundwater in Lake Hulun using hydrogen and oxygen isotopes and chloride ions. Water 11, 264.

Han, Y., An, Z., Marlon, J., Bradley, R., Zhan, C., Arimoto, R., Sun, Y., Zhou, W., Wu, F., Wang, Q., Burr, G., Cao, J. (2020). Asian inland wildfires driven by glacial–interglacial climate change. Proc. Natl. Acad. Sci. 117, 5184-5189.

Henderson, A., Holmes, J. (2009). Palaeolimnological evidence for environmental change over the past millennium from Lake Qinghai sediments: a review and future research prospective. Quat. Int. 194, 134-147.

Hilgen, F., Lourens, L., Van Dam, J., Beu, A., Boyes, A., Cooper, R., Krijgsman, W., Ogg, J., Piller, W., Wilson, D. (2012). Chapter 29 - The Neogene Period, in: the Geologic Time Scale. Elsevier, 923-978.

Holmes, J., Chivas, A. (2002). The Ostracoda: applications in Quaternary research. Geophys. Monogr. Ser. 131.

Hu, X., Li, Y., Yang, J. (2005). Quaternary paleolake development in the Fen River Basin, North China. Geomorphology 65, 1-13.

Jia, J., Zhu, L., Wang, Z., Wang, B., Chen, Q. (2019). The regional difference of climate evolution across mid-latitude Asia since mid-Pleistocene. Quat. Sci. 39, 549-556. (in Chinese with English abstract)

Juggins, S. (2022). Rioja: analysis of quaternary science data. R package version 1.0-5.

Kim, S., O’Neil, J. (1997). Equilibrium and nonequilibrium oxygen isotope effects in synthetic carbonates. Geochim. Cosmochim. Acta 61, 3461-3475.

Kong, F., Xu, S., Han, M., Chen, H., Miao, X., Kong, X., Jia, G. (2021). Application of grain size endmember analysis in the study of dust accumulation processes: a case study of loess in Shandong Province, East China. Sediment. Geol. 416, 105868.

Kranck, K., Smith, P., Milligan, T. (1996). Grain-size characteristics of fine-grained unflocculated sediments II: ‘Multi-round’ distributions. Sedimentology 43, 597-606.

Laskar, L., Robutel, P., Joutel, F., Gastineau, M., Correia, A., Levard, B. (2004). A long-term numerical solution for insolation quantities of the Earth. Astron. Astrophys. 428, 261-285.

Lebbink, M. (2010). Aeolian late Eocene deposition in Xining, central China. Dissertation/master's thesis. Utrecht University.

Lehmkuhl, F., Zens, J., Krauß, L., Schulte, P., Kels, H. (2016). Loess-paleosol sequences at the northern European loess belt in Germany: distribution, geomorphology and stratigraphy. Quat. Sci. Rev. 153, 11-30.

Leng, M., Marshall, J. (2004). Palaeoclimate interpretation of stable isotope data from lake sediment archives. Quat. Sci. Rev. 23, 811-831.

Li, H., Ku, T. (1997). δ^{13}C-δ^{18}C covariance as a paleohydrological indicator for closed-basin lakes. Palaeogeogr. Palaeoclimatol. Palaeoecol. 133, 69-80.

Li, H., Yang, X., Heller, F. (2008). High resolution magnetostratigraphy and deposition cycles in the Nihewan Basin (North China) and their significance for stone artifact dating. Quat. Res. 69, 250-262.

Li, R., Qiao, J., Qiu, W., Zhai, Q., Li, Y. (2000). Soluble salt deposit in the Nihewan beds and its environmental significance. Sci. China Ser. D Earth Sci. 43, 464-479.

Li, R., Yu, S., Sun, P., He, S., Yuan, Y., Xiong, Z. (2015). Characteristics of $\delta^{13}C$ in typical aquatic plants and carbon sequestration by plant photosynthesis in the Banzhai catchment, Maolan of Guizhou Province. Carsol. Sin. 34, 9-16. (in Chinese with English abstract)

Li, X., Huang, W., Wang, Y., Ji, J. (2010). A study of the palaeoclimates and palaeoenvironments in the Nihewan Basin in the light of the lithofacies and the palaeontological remains of the Pleistocene mammals. Chinese Sci. Bull. 55, 297-306. (in Chinese)

Li, Y., Xu, Q., Yang, X. (1996). Pollen records of the Feiliang Paleolithic site in Yangyuan, Hebei Province. Geogr. Territ. Res. 12, 55-59. (in Chinese)

Li, Y., Yang, J., Xia, Z., Mo, D. (1998). Tectonic geomorphology in the Shanxi Graben System, northern China. Geomorphology 23, 77-89.

Li, Y., Shi, W., Aydin, A., Beroya-Eitner, M., Gao, G. (2020). Loess genesis and worldwide distribution. Earth-Sci. Rev. 201, 102947.

Liang, X., Niu, Q., Qu, J., Liu, B., Liu, B., Zhai, X., Niu, B. (2019). Applying end-member modeling to extricate the sedimentary environment of yardang strata in the Dunhuang Yardang National Geopark, northwestern China. Catena 180, 238-251.

Lisiecki, L., Raymo, M. (2005). A Pliocene-Pleistocene stack of 57 globally distributed benthic $\delta^{18}O$ records. Paleoceanography 20, PA1003.

Liu, D., Pan, D., Bai, Y., He, X., Wang, D., Zhang, L. (2015). Variation of dissolved organic carbon transported by two Chinese rivers: the Changjiang River and Yellow River. Mar. Pollut. Bull. 100, 60-69.

Liu, T., An, Z., Yuan, B., Han, J. (1985). The loess-paleosol sequence in China and climatic history. Episodes 8, 21-28.

Liu, L. (1996). The Vegetation of Hebei. Science Press, Beijing. (In Chinese with English abstract)

Liu, P., Deng, C., Li, S., Zhu, R. (2010). Magnetostratigraphic dating of the Huojiadi paleolithic site in the Nihewan Basin, north China. Palaeogeogr. Palaeoclimatol. Palaeoecol. 298, 399408.

Liu, P., Yue, F., Liu, J., Qin, H., Li, S., Zhao, X., Xu, J., Yuan, B., Deng, C., Zhu, R. (2018). Magnetostratigraphic dating of the Shixia red sediments and implications for formation of Nihewan paleo-lake, North China. Quat. Sci. Rev. 193, 118-128.

Liu, P., Qin, H., Li, S., Yuan, B. (2021). Magnetostratigraphic dating of the danangou and dongyaozitou mammalian faunas in the Nihewan Basin, North China. Quat. Sci. Rev. 257, 106855.

Liu, Z., Wen, X., Brady, E., Otto-Bliesner, B., Yu, G., Lu, H., Cheng, H., Wang, Y., Zheng, W., Ding, Y., Edwards, R., Cheng, J., Liu, W., Yang, H. (2014). Chinese cave records and the East Asia summer monsoon. Quat. Sci. Rev. 83, 115-128.

Lordkipanidze, D., Ponce de Léón, M., Margvelashvili, A., Rak, Y., Rightmire, G., Zollikofer, C. (2013). A complete skull from Dmanisi, Georgia, and the evolutionary biology of early *Homo*. Science 342, 326-332.

Lu, S., Xue, Q., Zhu, L., Yu, J. (2008). Mineral magnetic properties of a weathering sequence of soils derived from basalt in Eastern China. Catena 73, 23-33.

Lu, H., Liu, W., Yang, H., Leng, Q., Liu, Z., Cao, Y., Hu, J., Sheng, W., Wang, H., Wang, Z., Zhang, Z. (2022). Decoupled land and ocean temperature trends in the early-middle Pleistocene. Geophys. Res. Lett. 49, e2022GL099520.

Magill, C., Ashley, G., Freeman, K. (2013a). Ecosystem variability and early human habitats in eastern Africa. Proc. Natl. Acad. Sci. U.S.A. 110, 1167-1174.

Magill, C., Ashley, G., Freeman, K. (2013b). Water, plants, and early human habitats in eastern Africa. Proc. Natl. Acad. Sci. U.S.A. 110, 1175-1180.

McLaren, P., Bowles, D. (1985). The effects of sediment transport on grain-size distributions. J. Sediment. Res. 55, 457-470.

Meng, X., Liu, L., Wang, X., Balsam, W., Chen, J., Ji, J. (2018). Mineralogical evidence of reduced East Asian summer monsoon rainfall on the Chinese loess plateau during the early Pleistocene interglacials. Earth and Planetary Sci. Lett, 486, 61-69.

Meisch, C. (2000). Freshwater Ostracoda of Western and Central Europe, Süßwasserfauna von Mitteleuropa 8/3. Heidelberg: Spektrum Akad. Verlag 522.

Meyer, I., Davies, G., Vogt, C., Kuhlmann, H., Stuut, J. (2013). Changing rainfall patterns in NW Africa since the Younger Dryas. Aeolian Res. 10, 111-123.

Meyer, I., Van Daele, M., Tanghe, N., De Batist, M., Verschuren, D. (2020). Reconstructing East African monsoon variability from grain-size distributions: end-member modeling and source attribution of diatom-rich sediments from Lake Chala. Quat. Sci. Rev. 247, 10657.

Meyers, S. (2014). Astrochron: an R package for astrochronology.

Min, L., Chi, Z., Zhu, G., Yao, P., Niu, P. (2002). Analysis of the palaeoenvironment of Quaternary stromatolites at Dongmulian, Yangyuan County of Hebei Province. Acta Geol. Sin. (Chin. Ed.) 76, 452-460. (in Chinese with English abstract)

Min, L., Chi, Z. Q. (2003). Quaternary geology of the Western Yangyuan Basin. Beijing: Geol. Publ. House.

Mischke, S., Herzschuh, U., Sun, Z., Qiao, Z., Sun, N., Zander, A. (2006). Middle Pleistocene Ostracoda from a large freshwater lake in the presently dry Qaidam Basin (NW China). J. Micropalaeontology 25, 57-64.

Mischke, S., Kramer, M., Zhang, C., Shang, H., Herzschuh, U., Erzinger, J. (2008). Reduced early Holocene moisture availability in the Bayan Har Mountains, northeastern Tibetan Plateau, inferred from a multi-proxy lake record. Palaeogeogr. Palaeoclimatol. Palaeoecol. 267, 59-76.

Mischke, S., Lai, Z., Faershtein, G., Porat, N., Röhl, M., Braun, P., Kalbe, J., Ginat, H. (2021). A Late Pleistocene wetland setting in the arid Jurf ed Darawish region in central Jordan. Front. Earth Sci. 9, 722435.

Moghazi, H., Zhao, H., Zhang, C., Eythorsdottir, E., Mischke, S. (2024a). Early Pleistocene depositional and environmental conditions at Dachangliang, Nihewan Basin, NE China. Front. Earth Sci. 12.

Moghazi, H., Zhao, H., Zhang, C., Omar, H., Eltijani, A., Mischke, S. (2024b). The East Asian monsoon variability in the Nihewan Basin, northern China, during the Early Pleistocene: a grain size end-member modelling analysis. Quat. Sci. Rev. 346, 109022.

Mu, H., Xu, Q., Zhang, S., Hun, L., Li, M., Li, Y., Hu, Y., Xie, F. (2015). Pollen-based quantitative reconstruction of the paleoclimate during the formation process of Houjiayao Relic Site in Nihewan Basin of China. Quat. Int. 374, 76-84.

Munsell Soil Colour Chart (2009). Munsell soil colour chart 2009 revised edition. Baltimore, Maryland, USA: Macbeth Division of Kollmorgen Corporation.

Nakagawa, T., Okuda, M., Yonenobu, H., Miyoshi, N., Fujiki, T., Gotanda, K., Tarasov, P.E., Morita, Y., Takemura, K., Horie, S. (2008). Regulation of the monsoon climate by two different orbital rhythms and forcing mechanisms. Geology 36, 491-494.

Nian, X., Gao, X., Xie, F., Mei, H., Zhou, L. (2014). Chronology of the Youfang site and its implications for the emergence of microblade technology in North China. Quat. Int. 347, 113-121.

Pang, Q., Zhai, D., Zhao, Z., Zhang, Z. (2015). Late Cenozoic micropalaeontology in the Nihewan Basin and its implications for environmental evolution. Acta Geol. Sin. 89, 817-842. (in Chinese with English abstract)

Paprocka, A. (2007). Stable carbon and oxygen isotopes in recent sediments of Lake Wigry, NE Poland: implications for lake morphometry and environmental changes. Terr. Ecol. 1, 267-281.

Påsse, T. (1997). Grain size distribution expressed as tanh-functions. Sedimentology 44, 1011-1014.

Paterson, G., Heslop, D. (2015). New methods for unmixing sediment grain size data. Geochem. Geophys. Geosyst. 16, 4494-4506.

Pei, S. (2002). The Paleolithic Site at Dachangliang in Nihewan Basin, North China. Acta Anthropol. Sin. 21, 116-125. (in Chinese with English abstract)

Pei, S., Li, X., Liu, D., Ma, N., Peng, F. (2009). Preliminary study on the living environment of hominids at the Donggutuo site, Nihewan Basin. Chin. Sci. Bull. 54, 3896-3904.

Pei, S., Xie, F., Deng, C., Jia, Z., Wang, X., Guan, Y., Li, X., Ma, D., de la Torre, I. (2017). Early Pleistocene archaeological occurrences at the Feiliang site, and the archaeology of human origins in the Nihewan Basin, North China. PLoS One 12, 0187251.

Pei, S., Deng, C., de la Torre, I., Jia, Z., Ma, D., Li, X., Wang, X. (2019). Magnetostratigraphic and archaeological records at the Early Pleistocene site complex of Madigou (Nihewan Basin): implications for human adaptations in North China. Palaeogeogr. Palaeoclimatol. Palaeoecol. 530, 176-189.

Prins, M., Weltje, G. (1999). End-member modeling of siliciclastic grain-size distributions: the late Quaternary record of eolian and fluvial sediment supply to the Arabian Sea and its paleoclimatic significance. In J. Harbaugh, W. Watney, E. Rankey, R. Slingerland, R. Goldstein, E. Franseen (Eds.), Numerical experiments in stratigraphy: Recent advances in stratigraphic and sedimentologic computer simulations. SEPM Society for Sediment. Geol. 62, 91-112

Prins, M., Vriend, M. (2007). Glacial and interglacial eolian dust dispersal patterns across the Chinese Loess Plateau inferred from decomposed loess grain-size records. Geochem. Geophys. Geosyst. 8, Q07Q05.

Prins, M., Zheng, H., Beets, K., Troelstra, S., Bacon, P., Kamerling, I., Wester, W., Konert, M., Huang, X., Ke, W., Vandenberghe, J. (2009). Dust supply from river floodplains: the case of the lower Huang He (Yellow River) recorded in a loess-palaeosol sequence from the Mangshan Plateau. J. Quat. Sci. 24, 75-84.

Potts, R., Faith, J. (2015). Alternating high and low climate variability: the context of natural selection and speciation in Plio-Pleistocene hominin evolution. J. Hum. Evol. 87, 5-20.

Potts, R., Dommain, R., Moerman, J., Behrensmeyer, A., Deino, A., Riedl, S., Beverly, E., Brown, E., Deocampo, D., Kinyanjui, R., Lupien, R. (2020). Increased ecological resource variability during a critical transition in hominin evolution. Sci. Adv. 43, 75-84.

Pye, K. (1995). The nature, origin and accumulation of loess. Quat. Sci. Rev. 14, 653-667.

Qian, S., Xu, Q., Griffiths, M., Yang, H., Xie, S. (2024). Decoupled terrestrial temperature and hydroclimate during the Plio-Pleistocene in the East Asian monsoonal region. Quat. Sci. Rev. 344, 108955.

Qiu, Z. (2000). Nihewan fauna and Q/N boundary in China. Quat. Sci. 20, 142-154. (in Chinese with English abstract)

Qin, X., Cai, B., Liu, T. (2005). Loess record of the aerodynamic environment in the East Asia monsoon area since 60,000 years before present. J. Geophys. Res. Solid Earth 110.

Rea, D., Hovan, S. (1995). Grain size distribution and depositional processes of the mineral component of abyssal sediments: lessons from the North Pacific. Paleoceanography 10, 251-258.

Rohling, E., Foster, G., Grant, K., Marino, G., Roberts, A., Tamisiea, M., Williams, F. (2014). Sea-level and deep-sea-temperature variability over the past 5.3 million years. Nature 508, 477-482.

Ruddiman, W., Raymo, M., Martinson, D., Clement, B., Backman, J. (1989). Pleistocene evolution: Northern hemisphere ice sheets and North Atlantic Ocean. Paleoceanography 4, 353-412.

Schick, K., Toth, N., Wei, Q., Clark, J., Etler, D. (1991). Archaeological perspectives in the Nihewan Basin, China. J. Hum. Evol. 21, 13-26.

Schwalb, A. (2003). Lacustrine ostracodes as stable isotope recorders of late-glacial and Holocene environmental dynamics and climate. J. Paleolimnol. 29, 267-351.

Schwalb, A., Dean, W., Güde, H., Hanisch, S., Sobek, S., Wessels, M. (2013). Benthic ostracode $\delta^{13}C$ as sensor for early Holocene establishment of modern circulation patterns in Central Europe. Quat. Sci. Rev. 66, 112-122.

Shao, Q., Wang, F., Ge, J., Bahain, J., Voinchet, P., Hu, G., Jin, X., Grün, R., Bae, C., Song, X. (2026). New U-series and coupled ESR/U-series dating of Xujiayao (northern China), the type site for *Homo juluensis*. Quat. Sci. Rev. 373, 109742.

Shen, G., Wang, Y., Tu, H., Tong, H., Wu, Z., Kuman, K., Fink, D., Granger, D. (2020). Isochron $^{26}Al/^{10}Be$ burial dating of Xihoudu: evidence for the earliest human settlement in northern China. L'Anthropol. 124, 102790.

Shen, H., Zhao, K., Ge, J., Zhou, X., Song, Y., Liu, S., Wang, Y., Jin, C., Gao, C., Huang, W., Li, X. (2021). Early and Middle Pleistocene vegetation and its impact on faunal succession on the Liaodong Peninsula, Northeast China. Quat. Int. 591, 15-23.

Stuut, J., Smalley, I., O'Hara-Dhand, K. (2009). Aeolian dust in Europe: African sources and European deposits. Quat. Int. 198, 234-345.

Sun, D., Bloemendal, J., Rea, D., Vandenberghe, J., Jiang, F., An, Z., Su, R. (2002). Grain-size distribution function of polymodal sediments in hydraulic and aeolian environments, and numerical partitioning of the sedimentary components. Sediment. Geol. 152, 263-277.

Sun, D., Bloemendal, J., Rea, D., An, Z., Vandenberghe, J., Lu, H., Su, R., Liu, T. (2004). Bimodal grain-size distribution of Chinese loess, and its palaeoclimatic implications. Catena 55, 325-340.

Sun, J. (2005). Long-term fluvial archives in the Fen Wei Graben, central China, and their bearing on the tectonic history of the India-Asia collision system during the Quaternary. Quat. Sci. Rev. 24, 1279-1286.

Sun, J., Ding, Z., Xia, X., Sun, M., Windley, B. (2018). Detrital zircon evidence for the ternary sources of the Chinese Loess Plateau. J. Asian Earth Sci. 155, 21-34.

Sun, M., Zhang, X., Tian, M., Liu, R., He, Z., Qi, L., Qiao, Y. (2018). Loess deposits since Early Pleistocene in northeast China and implications for desert evolution in east China. J. Asian Earth Sci. 155, 164-173.

Sun, X., Lu, H., Wang, S., Xu, X., Zeng, Q., Lu, X., Lu, C., Zhang, W., Zhang, X., Dennell, R. (2018). Hominin distribution in glacial-interglacial environmental changes in the Qinling Mountains range, central China. Quat. Sci. Rev. 198, 37-55.

Sun, Y., Lu, H., An, Z. (2006). Grain size of loess, palaeosol and Red Clay deposits on the Chinese Loess Plateau: significance for understanding pedogenic alteration and palaeomonsoon evolution. Palaeogeogr. Palaeoclimatol. Palaeoecol. 241, 129-138.

Talbot, M. (1990). A review of the palaeohydrological interpretation of carbon and oxygen isotopic ratios in primary lacustrine carbonates. Chem. Geol. Isot. Geosci. Sect. 80, 261-279.

Taner, M. (2000). Attributes revisited. Technical publication. Rock Solid Images Inc, Houston, Texas.

Teilhard de Chardin, P., Piveteau, J. (1930). Les mammifères fossiles de Nihowan (Chine). Ann. Paléontol. 19, 1-134.

Thomson, D. (1982). Spectrum estimation and harmonic analysis. Proc. IEEE 70, 1055-1096.

Tian, J., Wang, P., Cheng, X., Li, Q. (2002). Astronomically tuned Plio-Pleistocene benthic δ^{18}O record from South China Sea and Atlantic-Pacific comparison. Earth Planet. Sci. Lett. 203, 1015-1029.

Tian, J., Wang, P., Cheng, X. (2004). Development of the East Asian monsoon and Northern Hemisphere glaciation: oxygen isotope records from the South China Sea. Quat. Sci. Rev. 23, 2007-2016.

Tsoar, H., Pye, K. (1987). Dust transport and the question of desert loess formation. Sedimentology 34, 139-153.

Tong, H., Zhang, B., Chen, X. (2024). An overview and new insights into the Quaternary mammalian fauna from Nihewan Basin in North China. Acta Anthropol. Sin. 43, 157-183. (in chinese with English abstract)

Tong, H., Zhang, B., Chen, X., Wang, X., Sun, J. (2021). Chronological significance of the mammalian fauna from the Early Pleistocene Shanshenmiaozui site in Nihewan Basin, northern China. Acta Anthropol. Sin. 40, 469-489. (in Chinese with English abstract)

Tu, H., Luo, L., Deng, C., Ou, Z., Lai, Z., Shen, G., Bae, C., Granger D. (2022). Isochron ^{26}Al/^{10}Be burial dating of the Xiashagou Fauna in the Nihewan Basin, northern China: implications for biogeography and early hominin dispersals. Quat. Sci. Rev. 283, 107447.

Vandenberghe, J., Mücher, H., Roebroeks, W., Gemke, D. (1985). Lithostratigraphy and palaeoenvironment of the Pleistocene deposits at Maastricht-Belvedere, Southern Limburg, The Netherlands. Meded. Rijks Geol. Dienst 39-1, 7-18.

Vandenberghe, J., An, Z., Nugteren, G., Lu, H., van Huissteden, J. (1997). New absolute time scale for the Quaternary climate in the Chinese loess region by grain-size analysis. Geology 25, 35-38.

Vandenberghe, J., Lu, H., Sun, D., van Huissteden, J., Konert, M. (2004). The late Miocene and Pliocene climate in East Asia as recorded by grain size and magnetic susceptibility of the red clay deposits (Chinese Loess Plateau). Palaeogeogr. Palaeoclimatol. Palaeoecol. 204, 239-255.

Vandenberghe, J. (2013). Grain size of fine-grained windblown sediment : a powerful proxy for process identification. Earth-Sci. Rev. 121, 18-30.

Vandenberghe, J., Yang, X., Wang, X., Wang, S., Lu, H. (2021). Diverse floodplain deposits of reworked loess in a monsoon climate (Hanzhong Basin, central China). Quat. Res. 103, 4-20.

von Grafenstein, U., Erlenkeuser, H., Mu¨ller, H., Jouzel, J., Johnsen, S. (1999). A mid-European decadal isotope-climate record from 15,500 to 5000 years BP. Science 284, 1654-1657.

von Grafenstein, U., Eicher, U., Erlenkeuser, H., Ruch, P., Schwander, J., Ammann, B. (2000). Isotope signature of the Younger Dryas and two minor oscillations at Gerzensee (Switzerland): palaeoclimatic and palaeolimnologic interpretation based on bulk and biogenic carbonates. Palaeogeogr. Palaeoclimatol. Palaeoecol. 159, 215-229.

Walther, J. (1894). Einleitung in die Geologie als historische Wissenschaft. In Lithogenesis der Gegenwart. Jena: G. Fischer, Bd. 3, 535-1055.

Wang, H., Deng, C., Zhu, R., Wei, Q., Hou, Y., Bo¨eda, E. (2005). Magnetostratigraphic dating of the Donggutuo and Maliang paleolithic sites in the Nihewan Basin, north China. Quat. Res. 64, 1-11.

Wang, H., Deng, C., Zhu, R., Xie, F. (2006). Paleomagnetic dating of the Cenjiawan Paleolithic site in the Nihewan Basin, northern China. Sci. China Ser. D 49, 295-303.

Wang, X., Yang, Z., Løvlie, R., Min, L. (2004). High-resolution magnetic stratigraphy of fluvio-lacustrine succession in the Nihewan Basin, China. Quat. Sci. Rev. 23, 1187-1198.

Wang, X., Løvlie, R., Su, P., Fan, X. (2008). Magnetic signature of environmental change reflected by Pleistocene lacustrine sediments from the Nihewan Basin, North China. Palaeogeogr. Palaeoclimatol. Palaeoecol. 260, 452-462.

Wang, P., Tian, J., Lourens, L. (2010). Obscuring of long eccentricity cyclicity in Pleistocene oceanic carbon isotope records. Earth Planet. Sci. Lett. 290, 319-330.

Wang, Z., Huang, C., Zhou, Y., Pang, J., Zha, X. (2018). Characteristics of Holocene loess-palaeosol particle size composition and paleoclimatic significance in East Guanzhong, Shaanxi Province. Adv. Earth Sci. 33, 293-304.

Wei, Q. (1983). A new *Megaloceros* from Nihowan Beds. Vert. PalAsiat. 21, 87-95. (in Chinese with English abstract)

Wei, Q. (1991). Geologic sequence of the archaeological sites in the Nihewan Basin, North China. Contrib. XIII INQUA 61-73. (in Chinese with English abstract)

Wei, Q. (2016). Textual research of Nihewan Basin. Stor. Relics 2, 3-11.

Wentworth, C. (1922). A scale of grade and class terms for clastic sediments. J. Geol. 30, 377.

Weltje, G. (1997). End-member modeling of compositional data: numerical-statistical algorithms for solving the explicit mixing problem. Math. Geol. 29, 503-549.

Wu, F., Fang, X., Ma, Y., Herrmann, M., Mosbrugger, V., An, Z., Miao, Y. (2007). Plio-Quaternary stepwise drying of Asia: evidence from a 3-Ma pollen record from the Chinese Loess Plateau. Earth Planet. Sci. Lett. 257, 160-169.

Wu, L., Krijgsman, W., Liu, J., Li, C., Wang, R., Xiao, W. (2020). CFLab: a MATLAB GUI program for decomposing sediment grain size distribution using Weibull functions. Sediment. Geology 398, 105590.

Wu, P., Xie, Y., Li, Y., Kang, C., Chi, Y., Sun, L., Wei, Z. (2023). Provenance variations of the loess deposits in the East Asian monsoon boundary zone, Northeast China: response to the variations of climate and wind regimes. Catena 222, 106804.

Xia, Z. (1992). The study of the change of ancient lake shore in the Datong-Yangyan (Nihewan) Basin. Geogr. Res. 11, 52-59.

Xiao, J., Chang, Z., Si, B., Qin, X., Itoh, S., Lomtatidze, Z. (2009). Partitioning of the grain-size components of Dali Lake core sediments: evidence for lake-level changes during the Holocene. J. Paleolimnol. 42, 249260.

Xiao, J., Chang, Z., Fan, H., Zhou, L., Zhai, D., Wen, R., Qin, X. (2012). The link between grain-size components and depositional processes in a modern clastic lake. Sedimentology 59, 1050-1062.

Xiao, J., Fan, J., Zhou, L., Zhai, D., Wen, R., Qin, X. (2013). A model for linking grain-size component to lake level status of a modern clastic lake. J. Asian Earth Sci. 69, 149-158.

Xiao, J., Fan, J., Zhai, D., Wen, R., Qin, X. (2015). Testing the model for linking grain-size component to lake level status of modern clastic lakes. Quat. Int. 355, 34-43.

Xie, F., Cheng S. (1990). Palaeoliths excavation in Cenjiawan Village, Yangyuan County, Hebei Province. Acta Anthropol. Sin. 9, 265. (in Chinese with English abstract)

Xu, Z., Jiang, F., Zhao, H., Zhang, Z., Sun, L. (1989). Annals of Hulun Lake. Jilin Lit. Hist. Publ. House 691. (in Chinese)

Xu, Z., Pei, S., Hu, Y., de la Torre, I., Ma, D. (2021). Stable isotope analysis of mammalian enamel from the Early Pleistocene site of Madigou, Nihewan Basin: implications for reconstructing hominin paleoenvironmental adaptations in North China. Front. Earth Sci. 9, 789781.

Xu, Z., Pei, S., Hu, Y., de la Torre, I., Ma, D., Ye, Z., Deng, C. (2023). Ecological shifts and hominin adaptations during the Mid-Pleistocene Climate Transition in Northeast Asia as evidenced by isotopic analysis ($\delta^{13}C$, $\delta^{18}O$) of mammalian enamel from early Paleolithic sites in the Nihewan Basin, China. Quat. Sci. Rev. 308, 108072.

Xu, Y., Sun, Q., Yin, X., Long, H., Li, D., Lin, F. (2024). Late Pleistocene Sea level change and tectonism control the formation of the Old Red Sand along the southeastern coast of China. Palaeogeogr. Palaeoclimatol. Palaeoecol. 637, 112018.

Yamamoto, M., Clemens, S., Seki, O., Tsuchiya, Y., Huang, Y., O'ishi, R., Abe-Ouchi, A. (2022). Increased interglacial atmospheric CO_2 levels followed the mid-Pleistocene Transition. Nat. Geosci. 15, 307-313.

Yang, S., Deng, C., Zhu, R., Petraglia, M. (2019). The Paleolithic in the Nihewan Basin, China: evolutionary history of an early to late Pleistocene record in Eastern Asia. Evol. Anthropol. 29, 125-142.

Yang, S., Yue, J., Zhou, X., Storozum, M., Huan, F., Deng, C., Petraglia, M. (2020). Hominin site distributions and behaviours across the Mid-Pleistocene Climate Transition in China. Quat. Sci. Rev. 248, 106614.

Yang, S., Wang, F., Xie, F., Yue, J., Deng, C., Zhu, R., Petraglia, M. (2021). Technological innovations at the onset of the Mid-Pleistocene Climate Transition in high-latitude East Asia. Nat. Sci. Rev. 8, nwaa053.

Yang, J., Zhang, Z., Li, Y., Wang, F., Fan, B., She, Z., Xie, H., Wang, S., Da, S. (2022). Environment of the early Pleistocene Banshan Paleolithic site in the Nihewan Basin, north China. Front. Earth Sci. 10, 830798.

Yang, X., Wang, X., Van Balen, R., Prins, M., Wang, S., van Buuren, U., Lu, H. (2019). Fluvial terrace formation and its impacts on early human settlement in the Hanzhong basin, Qinling Mountains, central China. Glob. Planet. Change 178,1-14.

Young, C. (1950). "The Plio-Pleistocene boundary in China," Rep. ^{18}th Int. Geol. Congr. (London: Wiley), 115-125.

Yuan, B., Xia, Z., Niu, P. (2011). Nihewan Rift and Early Man. Beijing: Geology Press, 12-20. (in Chinese)

Zanchetta, G., Drysdale, R., Hellstrom, J., Fallick, A., Isola, I., Gagan, M., Pareschi, M. (2007). Enhanced rainfall in the Western Mediterranean during deposition of sapropel S1: stalagmite evidence from Corchia cave (Central Italy). Quat. Sci. Rev. 26, 279-286.

Zan, J., Fang, X., Zhang, W., Yan, M., Zhang, D. (2018). A new record of late Pliocene-Early Pleistocene aeolian loess-red clay deposits from the western Chinese Loess Plateau and its palaeoenvironmental implications. Quat. Sci. Rev. 186, 17-26.

Zeng, L., Lu, H., Yi, S., Xu, Z., Qiu, Z., Yang, Z., Li, Y. (2011). Magnetostratigraphy of loess in northeastern China and paleoclimatic changes. Chin. Sci. Bull. 56, 2267-2275. (in Chinese)

Zeng, L., Lu, H., Yi, S., Li, Y., Lv, A., Zhang, W., Xu, Z., Wu, H., Feng, H., Cui, M. (2016). New magnetostratigraphic and pedostratigraphic investigations of loess deposits in North-East China and their implications for regional environmental change during the Mid-Pleistocene Climatic Transition. J. Quat. Sci. 31, 20-32.

Zhang, J., Chen, F., Holmes, J., Li, H., Guo, X., Wang, J., Li, S., Lü, Y., Zhao, Y., Qiang, M. (2011). Holocene monsoon climate documented by oxygen and carbon isotopes from lake sediments and peat bogs in China: a review and synthesis. Quat. Sci. Rev. 30, 1973-1987.

Zhang, W., Mischke, S., Zhang, C., Gao, D., Fan, R. (2013). Ostracod distribution and habitat relationships in the Kunlun Mountains, northern Tibetan Plateau. Quat. Int. 313-314, 38-46.

Zhang, Z., Li, Y., Li, C., Xu, Q., Zhang, R., Ge, Y., Li, B., Deng, C., Li, Z., Zhang, L. (2020). Pollen evidence for the environmental context of the early Pleistocene Xiashagou fauna of the Nihewan Basin, north China. Quat. Sci. Rev. 236, 106298.

Zhang, Z., Wang, Y., Li, Y. (2024). Research progress on the relationship between Paleolithic hominid activities and environmental changes in the Nihewan Basin. Acta Anthropol. Sin. 43, 184.

Zhai, D., Xiao, J., Zhou, L., Wen, R., Chang, Z., Wang, X., Jin, X., Pang, Q., Itoh, S. (2011). Holocene East Asian monsoon variation inferred from species assemblage and shell chemistry of the ostracodes from Hulun Lake, Inner Mongolia. Quat. Res. 75, 512-522.

Zhou, T., Li, H., Liu, Q., Li, R., Sun X. (1991). Cenozoic Paleography Research of Nihewan Basin.

Zhou, X., Yang, J., Wang, S., Xiao, G., Zhao, K., Zheng, Y., Shen, H., Li, X. (2018). Vegetation change and evolutionary response of large mammal fauna during the Mid-Pleistocene Transition in temperate northern East Asia. Palaeogeogr. Palaeoclimatol. Palaeoecol. 505, 287-294.

Zhou, X., Yang, J., Xiao, G., Wang, J., Hu, Y., Zheng, Y., Liu, J., Li, X. (2023). Megacycles of climate and vegetation in East Asia since 3 Ma. Catena 229, 107195.

Zhu, R., Deng, C., Pan, Y. (2007). Magnetochronology of the fluvio-lacustrine sequences in the Nihewan basin and its implications for early human colonization of Northeast Asia. Quat. Sci. 27, 922-944. (in Chinese with English abstract)

Zhu, R., Hoffman, K., Potts, R., Deng, C., Pan, Y., Guo, B., Shi, C., Guo, Z., Yuan, B., Hou, Y., Huang, W. (2001). Earliest presence of humans in northeast Asia. Nature 413, 413-417.

Zhu, R., Potts, R., Xie, F., Hoffman, K., Deng, C., Shi, C., Pan, Y., Wang, H., Shi, R., Wang, Y., Shi, G., Wu, N. (2004). New evidence on the earliest human presence at high northern latitudes in Northeast Asia. Nature 431, 559-562.

Zhu, Z., Dennell, R., Huang, W., Wu, Y., Rao, Z., Qiu, S., Xie, J., Liu, W., Fu, S., Han, J., Zhou, H. (2015). New dating of the *Homo erectus* cranium from Lantian (Gongwangling), China. J. Hum. Evol. 78, 144-157.

Zhu, Z., Dennell, R., Huang, W., Wu, Y., Qiu, S., Yang, S., Rao, Z., Hou, Y., Xie, J., Han, J., Ouyang, T. (2018). Hominin occupation of the Chinese Loess Plateau since about 2.1 million years ago. Nature 559, 608-612.

Ziegler, M., Lourens, L., Tuenter, E., Hilgen, F., Reichart, G., Weber, N. (2010). Precession phasing offset between Indian summer monsoon and Arabian Sea productivity linked to changes in Atlantic overturning circulation. Paleoceanography 25.